Performance Evaluation of a Magnetically Enhanced Micro-Cathode Vacuum Arc Thruster

by Thomas Andrew Denz

B.S. in Mechanical Engineering, November 1980, The Pennsylvania State University
B.S. in Computer Information Systems, March 1999, Strayer University

A Thesis submitted to

The Faculty of
The School of Engineering and Applied Science
of The George Washington University
in partial fulfillment of the requirements
for the degree of Master of Science

August 31, 2012

Thesis directed by

Michael Keidar
Associate Professor of Engineering and Applied Science

ProQuest LLC.
789 East Eisenhower Parkway
P.O. Box 1346
Ann Arbor, MI 48106 - 1346

Dedication

This work is dedicated to my fellow classmates.

Acknowledgments

Acknowledgment is given to Taisen Zhuang for his work on the development and testing of the Micro-Cathode Vacuum Arc Thruster. The University of Southern California (USC) also provided assistance with many of the actual tests of the thruster unit. Finally, Professor Michael Keidar provided much help and advice throughout the project.

Abstract of Thesis

Performance Evaluation of a Magnetically Enhanced Micro-Cathode Vacuum Arc Thruster

A magnetically enhanced Micro-Cathode Vacuum Arc Thruster (μCAT) was designed and fabricated at the George Washington University (GWU). This thesis reports on the results of experimental performance testing of the μCAT. The thruster impulse and exhaust velocity were considered as well as various energy and efficiency values. Magnetic field simulations were conducted of different permanent magnet configurations that could be used in the magnetically enhanced μCAT. Plasma parameters within the μCAT were examined. Finally, a possible μCAT application to perform an orbit change maneuver for a small satellite was considered.

Table of Contents

List of Figures

List of Tables

List of Symbols / Nomenclature

a	semi-major axis of an ellipse
A	area of magnetic field coil
B	magnetic field strength
$\vec{B}$	magnetic field strength as a vector
c	exhaust velocity
C	capacitance
deltaT	time step
e	electronic charge
E	electrical energy
$\vec{E}$	electric field
E_{arc}	arc energy
$E_{arcpeaks}$	arc energy from experimental data
E_{coil}	magnetic field coil energy
E_{coil_mag}	magnetic coil energy
$E_{coilmag}$	magnetic coil energy
E_{coil_res}	magnetic field coil resistive energy losses
$E_{coiltotalmagres}$	magnetic field coil energy with magnetic and resistive components
E_{PFN}	energy stored in pulse forming network
E_{plume}	energy in plume
Efficiency1	efficiency based on arc energy
Efficiency2	efficiency based on arc and coil magnetic energies
Efficiency3	efficiency based on arc and coil magnetic and resistive energies
F_{12}	electrostatic force between charged particles

$\vec{F}_{12}$	electrostatic force between charged particles as a vector
$\vec{F}_{el}$	electrostatic force on a charged particle
$\vec{F}_{mag}$	magnetic force on a charged particle
F_{mag_ion}	magnetic force on an ion
h_a	apogee altitude
h_p	perigee altitude
I	current
I	impulse
I_{arc}	arc current
$\overline{I_{arc}}$	average arc current
I_{coil}	magnetic field coil current
I_{coil_final}	final current value
K	Boltzmann's constant
l	length of magnetic field coil
L	characteristic dimension
L	inductance of magnetic field coil
m	mass of a particle
m	mass of cathode erosion per spot
m	propellant mass
$\dot{m}$	cathode material erosion rate
$\dot{m}_{arc}$	plasma ion mass flow rate
$\dot{m}_{arc}$	plasma flow rate
$\dot{m}_{cathode}$	total cathode mass flow rate
m_{pp}	mass of material in exhaust per pulse

M	impulse
M_0	initial satellite mass
M_f	final satellite mass
M_p	propellant mass
n	number of coil turns per unit length
n	particle number density
N	number of capacitors in network
N	number of turns on anode-cathode magnetic field coil
P	power
P_{coil}	power in magnetic field coil
PRF	pulse repetition frequency
q	electric charge of a particle
q_1	electric charge on particle 1
q_2	electric charge on particle 2
q_{Tion}	electric charge of titanium ion
r	distance from center of Earth to satellite
$\hat{r}_{12}$	unit vector between particles
r_{12}	separation distance between particles
r_a	apogee distance
r_{ave}	average radius of magnetic field coil
r_e	radius of the Earth
r_{Le}	Larmor radius for electrons
r_{Li}	Larmor radius for ions
r_p	perigee distance

$R_{an\_cath\_sh}$	resistance of anode-cathode shunt resistor
R_{coil}	resistance of magnetic field coil
$R_{mag\_coil\_sh}$	resistance of magnetic field coil shunt resistor
R_{pl}	resistance of arc
R_{shunt}	resistance of shunt resistor
$SumE_{arc}USC14/14$	average arc energy value
t	time
t_{off}	time between current pulses
t_{on}	time duration of current
T	thrust
T_e	electron temperature
$TotalE_{arc}$	arc energy per pulse
U	voltage potential
U_0	charging voltage
U_{ac}	potential across anode and cathode
U_{ad}	arc discharge voltage
v	ion velocity
v	velocity component of exhaust in direction of thrust
V	exhaust velocity
V	spacecraft velocity
$\vec{V}$	particle velocity
V_a	velocity at apogee
V_{arc}	arc voltage
$V_{circular}$	velocity in circular orbit

V_{coil}	voltage on magnetic field coil
V_{mag}	voltage on magnetic field coil
V_{per}	velocity perpendicular to magnetic field
$V_{perpendicular}$	particle velocity component perpendicular to magnetic field
V_{sh}	voltage across shunt resistor
V_{shunt}	voltage across shunt resistor
ϵ_0	permittivity of free space
η	efficiency
η_{arc_energy}	energy efficiency
η_{PPU}	efficiency of power processing unit
$\eta_{propellant}$	propellant efficiency
λ_D	Debye Length
μ	gravitational parameter
μ	proportionality constant
μ_0	permeability of free space

Chapter 1 – Introduction

The purpose of this thesis was to perform an evaluation of the operation of a small Micro-Cathode Vacuum Arc Thruster (μCAT) with an externally applied magnetic field. A historical survey was conducted on electric propulsion efforts in the past. A μCAT was developed at the George Washington University (GWU). The hardware and its operation are described. A number of tests were performed with the μCAT and extensive data was collected. Some of the tests involved measurement of the thruster impulse and the exhaust velocity of the plasma propellant. A large amount of testing was done to determine the energy usage in different parts of the μCAT. The kinetic energy in the exhaust plume was studied. The electrical energy in the arc was measured in experimental trials. Electrical energy in the μCAT magnetic field coil was also measured. Various efficiency measures were then determined from the actual data collected. The specific effects of various magnetic field coil strengths on the μCAT efficiencies were studied.

The use of permanent magnets to produce similar magnetic fields to that obtained with the magnetic field coil was considered. Modeling software was used to simulate various configurations of the permanent magnets and determine the directions of the magnetic field lines. Knowledge of the magnetic field around the magnets was used to ascertain appropriate arrangements of the hardware components.

Plasma properties resulting from the arc in the thruster were studied. The Debye Length and the Larmor radii for the ions and electrons were calculated. Magnetic forces on the charged particles, electrostatic forces from the anode and cathode, and electrostatic

forces between charged particles were also evaluated. Finally, a specific application of the μCAT to perform an orbit change for a small satellite was considered to determine the necessary mass of plasma propellant.

Lessons learned were summarized in the Conclusions section. References 1 and 2 also contain information on analysis and testing performed on the GWU μCAT.

Chapter 2 – Document Review and Historical Background

Extensive research has been done in the past regarding plasmas from vacuum arcs and the use of plasmas in vacuum arc thrusters.

Plyutto, et al, in reference 3 pointed out that high speed plasma streams emanating from a cathode in vacuum arcs have been observed since 1930. Representative particle energies of 80 eV with copper cathodes had been measured. It was also mentioned in reference 3 that plasma jets were determined to produce forces on the cathode of 2.5 to 15 dynes/A. Plyutto, et al, conducted their own experiments with vacuum arcs and investigated arc stability. The cathode material was found to be consumed and produced both plasma and macroparticles. The plasma density tended to have a cosine distribution with a maximum along the line normal to the cathode surface. The macroparticles tended to remain close to the plane of the cathode surface itself. The amount of macroparticles produced depended on the cathode material and on the duration and current level of the arc. A pendulum setup in a vacuum chamber was used to estimate the plasma velocities. These velocities depended on the cathode material and ranged from 1.8×10^5 to approximately 9×10^5 cm/sec (1.8×10^3 to 9×10^3 m/sec). Ion energies measured with an electrostatic probe were found to vary from approximately 5 to 40 eV again depending on the type of material. Mass spectroscopic analysis revealed the presence of multiply charged ions and indicated a range of ionization rates from 12 to 100 percent. Plyutto, et al, noted that multiply charged ions occur much less with higher arc currents. Representative plasma properties were used in analysis discussed in the paper. The value used for the peak electron density in the vicinity of the cathode spot was $10^{18}/cm^3$

($10^{24}/m^3$). The ion velocity used in analysis was $5x10^5$ cm/sec ($5x10^3$ m/sec) and the electron velocity used was 10^8 cm/sec (10^6 m/sec).

In reference 4, Gilmour evaluated the use of a vacuum arc specifically for electric propulsion. The vacuum arc occurs between a cathode and anode when some of the cathode is vaporized and ionized providing an electrically conductive path. The necessary voltage to sustain an arc was found to range from 8 to 33 volts depending on the cathode material. The necessary electron current for a stable arc ranged from 2 to 60 amps also depending on the material. Experiments conducted revealed that additional power was needed to sustain an arc when an increased magnetic field was applied normal to the cathode. Gilmour stated that the cathode mass consumption rate again depends on the cathode material. A value of $0.2x10^{-3}$ gm/coulomb of electron charge was given as an average and a value of $0.02x10^{-3}$ gm/coulomb was listed as a minimum value. The plasma plume produced at the cathode was described to be conical with a semiangle of about 30 degrees. A possible value of 10^6 amps/cm^2 (10^{10} amps/m^2) was given for the emission current density. Gilmour reported on previous measurements of plasma plume velocities. They depend on the cathode material with $2x10^4$ m/sec listed as a normal value for copper. It was mentioned that such a velocity would result in a particle energy of 130 eV and a specific impulse of 2000 sec.

Gilmour further described experiments run on a vacuum arc system. The pressure in the system chamber was typically kept less than 10^{-4} mm Hg. A cathode rod was positioned inside an annular anode. The cathode was partly consumed during the process but was not advanced forward into and through the anode. The experiment durations

varied from two to five minutes with the result that the amount of recession of the cathode surface was limited to about 0.05 inches. Measurements of the resistance of the metallic film deposition on a flat plate positioned six inches in front of the cathode revealed that most of the material in the plasma plume was concentrated in a 60 degree cone centered on the cathode/anode axis. It was also noted that for experiments run with tin as the material, a tin film was left on the concentrically located insulator between the cathode and anode after the arc. Subsequent arcs could then be initiated by passing an electric current through the film. Some of the experiments were conducted with a magnetic field applied in the vicinity of the cathode by a solenoid coil placed concentrically about the cathode/anode axis. Tests were run with magnetic field strengths varying from zero to 500 gauss. It was found that the power needed for the arc and the efficiency of the device increased with the magnetic field strength. Efficiencies from 5 to 8 percent and 12 to 18 percent ranges were mentioned for different materials with no magnetic field applied. The efficiency for copper increased to around 30 percent when a 500 gauss magnetic field was used. The higher magnetic field strengths were found to direct the plasma plume perpendicular to the cathode surface. Such a direction is more desirable for thruster applications where the cathode face is perpendicular to the thrust direction. Calculations for thrust and specific impulse resulted in values of over 10^{-3} lbs and 1200 sec, respectively. An experiment was also run with a wider disk shaped cathode and no magnetic field. The efficiency was found to be 15 percent and the specific impulse was 1000 sec. The erosion of the cathode material was even on its surface. Other experiments with stainless steel and titanium resulted in efficiencies greater than 20 percent. Gilmour proposed that a vacuum arc thruster could be used for

satellite station-keeping applications with a three year life possible. He also indicated that higher magnetic field strengths could result in a better thruster.

Gilmour, et al, continued reporting on a vacuum arc thruster in reference 5. In it, reference 4 was reviewed and values of 2×10^4 m/sec and 1.5×10^{-6} N/amp were given as typical for the plasma plume velocity and reaction force on the cathode when copper was used for the cathode material. An efficiency term, η, was defined to relate the electrical energy, E, stored in a capacitor and the kinetic energy of the exhaust in the direction of the thrust.

$$\eta E = \frac{1}{2} m_{pp} v^2 \tag{2-1}$$

In this equation, m_{pp} is the mass of material in the exhaust per pulse and v is the velocity component of the exhaust in the direction of the thrust.

Experimental results indicated that the use of magnetic field coils concentric with the axis of the thruster produced a large increase in the resistance of the arc. A representative value for the duration of an arc pulse was 1.2×10^{-3} sec. An experimental design for a pulsed vacuum arc thruster was developed that used a thin cylindrical cathode with a flat face for arcing. It was configured to provide a 2000 N sec total impulse, 10^{-4} N sec of impulse per pulse, and 1000 sec for a specific impulse. Some problems occurred in achieving a uniformly distributed consumption of the cathode material during thruster operation. Possible fixes were considered including the use of varying cathode materials within the thruster and a cathode feed mechanism to advance the material toward the arc region. An observation reported in reference 5 was that the

thruster efficiency and specific impulse did not depend on the cathode material if the operating potential was much higher than the minimum potential needed for the arc. In addition, cathode materials that release solid pieces, or beads, during arcing provide a lower specific impulse. Conically shaped anodes at different angles were used in experiments to develop a suitable configuration. It was found that several sparks from an igniter electrode were sometimes necessary to initiate the full vacuum arc. Then, a four arc pulse per second or higher rate was achieved.

Experimental results were described further in reference 5. A torsional pendulum was used to measure thrust and was suitable for the thruster with its 10^{-4} N sec of impulse per pulse. A calorimeter was used to measure the energy in the plasma plume. An efficiency was then determined by comparing the plume energy and the arc input energy. Some experiments were conducted with bismuth as the material, which was able to operate at a low 28 volts. As a result of high levels of neutrals in the exhaust, the efficiency with bismuth was only 1% and the specific impulse was less than 100 sec. Additional experiments at higher voltages were conducted with other cathode materials. Gold and stainless steel were used at 200 volts, which resulted in an efficiency of 10% and a specific impulse of 1000 sec. It was reported that successful operation for long periods of time was conducted.

In the summarization of reference 5, values of 10^{-5} to 10^{-4} N sec of impulse per pulse, 1000 sec for specific impulse, and 10% for an efficiency were provided. Advantages of a pulsed vacuum arc thruster were listed. The cathode material is the fuel and has a high density and can be non-corrosive. The cathode utilization rate is

proportional to the electric current in the arc. Fuel valves are not needed. Operation with low voltages below 200 volts is possible. A specific impulse of 1000 sec can be achieved. Maintaining a vacuum during testing is easier while using metallic cathodes.

Dethlefsen reported on pulsed vacuum arc thrusters in reference 6. He pointed out that the velocity of emitted electrode material from a vacuum arc can be as high as 10^5 m/sec and the current density can be 10^7 amps/cm^2 (10^{11} amps/m^2). Cathode metals with low melting points and low thermal conductivity tend to release droplets of material during arcing. The result is a lower efficiency in a vacuum arc thruster. Magnesium and copper are better materials to use since they produce fewer droplets. A shorter current pulse, possibly around 10^{-5} sec, also reduces droplet formation.

Specific measurements of a thruster mounted on a pendulum were made and reported on in reference 6. The arc discharge was started with a high voltage pulse applied to a trigger electrode. The vacuum pressure was around 10^{-6}torr. Lead, antimony, tin, and magnesium were tested. Lead, antimony, and tin had small droplets in the exhaust and a resulting lower performance. Better performance was obtained with magnesium in a thruster that had a conical anode configuration. Two cases were listed for magnesium. Specific values included cathode mass consumption rates of 4.6×10^{-6} and 1.68×10^{-6} gm/shot, impulse figures of 18.0 and 9.05 dyne sec/shot, specific impulse figures of 4000 and 5500 sec, and efficiency levels of 12.5 and 12.6%. The efficiency was determined from the ratio of kinetic energy in the exhaust to electrical energy stored in the thruster capacitor. The following formula was used.

$$\eta = \frac{M^2/2m}{CU^2/2} \tag{2-2}$$

M is the impulse. m is the mass of cathode erosion per shot. C is the capacitor value. U is the voltage potential. A large anode does not experience significant material erosion during arcing. A thruster configuration with a small anode area, however, can produce vapor jets from both the anode and cathode.

Time-of-flight measurements were made on a thruster with anode and cathode material erosion. A velocity value of 4.2×10^4 m/sec and a specific impulse of 4300 sec were found for magnesium. Additional tests provided values for mass consumption rates of 4.12×10^{-6} to 1.24×10^{-5} gm/shot, impulse figures of 7.7 to 18 dyne sec/shot, specific impulse values of 1480 to 1900 sec, and efficiency levels of 7.7 to 9.7%. With a small anode, it was noted that the anode erosion was more than that from the cathode. A thruster with a cathode jet alone performs a little better than one with both cathode and anode jets. Dethlefsen concluded that an anode jet does not accelerate the electrode material quite as well as a cathode jet. Nevertheless, a vacuum arc thruster configured to erode both the cathode and anode could utilize both electrodes as fuel. Both electrodes could be eroded at the same rate by reversing the discharge capacitor electrical polarity periodically. It was also mentioned that the efficiencies obtained were less than for ion engines.

Dethlefsen listed simplicity, a passive quality when not in use, digital control, a high specific impulse, and low weight as advantages for a pulsed vacuum arc thruster. A

specific application includes satellite attitude control. Inefficiency can arise from Joule heating in the electric circuits. The vacuum arc resistance was noted to be $10x10^{-3}$ ohms, which is similar to that of the discharge circuit itself. Conclusions were provided in reference 6 that 5660 sec and higher values for specific impulse were measured, efficiencies were dependent on electrode material and the electric current pulse, and a vacuum arc thruster might be good for electric micro-propulsion.

Gilmour, et al, reported in reference 7 on experiments conducted to generate a metallic plasma in vacuum. A 400 microsecond laser burst was used to illuminate a cathode. An electric current continued for about 800 microseconds after the laser pulse, probably coming from a vacuum arc. It was noted that the vacuum arc plasma plume was highly directional, probably high speed, and the electron current density was 10^6 amps/cm^2 (10^{10} amps/m^2) or more. Besides using a laser to initiate an arc, other methods included a mechanically moved igniter electrode and a fixed igniter injecting a plasma burst. Pulsed operation allowed for a high peak power during pulses. The duty factor, or combination of pulse duration and frequency, could be modified to change the average power.

Gilmour, et al, provided some characteristics of vacuum arcs. In an arc, some of the negative electrode material is vaporized and ionized into a plasma, which provides an electrically conducting path between the electrodes. The consumption rate of the cathode could be about 10^{-7} kg/coulomb of charge emitted and is constant for a given material and operating conditions. The cathode spot in a vacuum arc is made up of discrete cells, each conducting a small range of current. Different materials have a minimum, or threshold,

current possible. High boiling point materials may not exhibit the discrete cell behavior. Cells and arcs have random and finite lifetimes. A value of 10^4 m/sec is typical for the velocity of an arc plasma. Therefore, the pressure on the cathode at the arc spot is high. The range could be 0.2 to 95 atmospheres, depending on the material. Again, the current density in the cathode spots could be greater than 10^6 amps/cm^2 (10^{10} amps/m^2). High currents, pressures, and temperature gradients could result in the ejection of droplets, or beads, of material. This larger scale erosion, rather than the emission of a plasma or ionized vapor, is usually unwanted.

Gilmour, et al, reported further on the configuration of a metallic plasma generator. A small diameter cathode is used with a spring to advance it forward as the material is consumed. The energy storage unit can be a capacitor or pulse forming network. The current may be a few hundred amps and the voltage may be a few hundred volts. A magnetic field coil is placed around the ring shaped anode and provides a self-limiting effect on the arc discharge current and control of the angular dispersion of the plasma jet. A current pulse is sent which vaporizes a metallic film on the surface of an insulator near the cathode. This process creates a plasma which provides a path for the main arc current. The vacuum arc redeposits a metallic film on the insulator, which allows for additional pulsed operation. Besides a current pulse to vaporize a conductive film on an insulator, several other methods of arc ignition were described. A pulsed laser, an igniter electrode, a high voltage breakdown of several thousand volts on an insulator, and a titanium hydride igniter releasing hydrogen that ionizes were mentioned. For the method using the conductive film on an insulator, a discharge capacitor can be sized to vaporize as much film as deposited by the main arc. In this way, the film does

not build up excessively. A few hundred volts on a 0.1 to 1.0 micro-farad capacitor is typical.

Several cathode configurations were reviewed. Different geometries for the electrodes are better suited for different electric input characteristics. Favorable operation in one configuration was obtained with a voltage value of 200 volts, a charge per pulse of $6x10^{-3}$ coulombs, a peak current of 200 amps, and a pulse duration of 55 microseconds. With a cathode feed mechanism and appropriate values for the arc current, several thousand hours of operation are possible. Pulse durations were varied from 2 microseconds to continuous operation and pulse frequencies over 300 pulses/sec were demonstrated.

It was found that the anode configuration could be varied to concentrate magnetic field lines from a magnetic field coil. The magnetic field could help direct the plasma plume for propulsion applications. In an arrangement with a concentric anode, cathode, and magnetic field coil around one axis, the magnetic field lines have a tendency to cause some of the charged particles to move around that axis. In some regions then, JxB forces act further on azimuthally moving charged particles to compress them toward the axis and to give them a component of velocity in the axial direction. A higher magnetic field strength obviously results in a higher axial component of velocity. The magnetic field coil producing the magnetic field could also be tilted from the thruster axis to produce a thrust vectoring effect. Gilmour, et al, pointed out that an axial magnetic field in the concentric anode and cathode configuration increases the arc discharge impedance significantly. Without a magnetic field, the impedance could be a few milli-Ohms.

Gilmour, et al, reported on experiments with pulsed vacuum arcs for electric propulsion. Measurements were used to obtain specific performance values of 1000 sec for the specific impulse and almost 1500 lb sec for the total impulse. The efficiency could be greater than 10% and a life duration of 10^8 pulses was possible. A thrust vector effect up to 15 degrees was demonstrated with field coils.

Dorodnov discussed some of the properties of plasma streams and vacuum arcs in reference 8. Representative ion energies in a plasma stream could be 10^0 to 10^4eV. Ion energies in a vacuum arc cathode spot vary from 10 to 100 eV. Thermal energy values are typically on the order of 1 eV. Ion current densities in a plasma stream could be 10^{-4} to 10^2 amps/cm^2 (10^0 to 10^6 amps/m^2). The cathode material erosion rate, $\dot{m}$, in a vacuum arc was specified as being proportional to the current, I.

$$\dot{m} = \mu I \tag{2-3}$$

The proportionality constant, μ, was listed as having values of approximately 0.4 to $1x10^{-4}$ g/coulomb for different cathode materials. Titanium specifically had a value of $0.53x10^{-4}$ g/coulomb. Dorodnov pointed out that the cathode erosion products contain vapor, ions with different charge states, and microscopic droplets. The droplets could be 1% of the eroded output for high melting point materials. In low melting point materials, the amount of erosion products in droplet form could be an order of magnitude higher.

Anders, et al, discussed power supplies for arcs in reference 9. Arc initiation methods were mentioned. They include the use of a high voltage applied across a trigger electrode and a cathode, a movable trigger electrode, a laser plasma trigger, and a

triggerless method involving application of a supply voltage to a conductive path between an anode and cathode. In this last method, the initial current causes gas and plasma to be released at the cathode. A cathode spot and arc initiation follow. A supply voltage over 500 volts was advantageous.

The electric arc resistance is usually small. A representative value was determined in reference 9 from

$$R_{pl} = \frac{U_{ac}}{I_{arc}} \tag{2-4}$$

where R_{pl} is the resistance of the arc, U_{ac} is the potential across the anode and cathode, and I_{arc} is the arc current. For a potential of 20 volts and an arc current of 200 amps, the resistance of the arc is 0.1 ohms. Characteristics of a pulse forming network of capacitors and coils was also discussed in reference 9. The stored energy, E_{PFN}, in such a network can be found from

$$E_{PFN} = \frac{N}{2} C U_0^2 \tag{2-5}$$

where N is the number of capacitors in the network, C is the capacitance value, and U_0 is the charging voltage. The efficiency of the reference 9 power supply was improved with the use of a diode to limit the charging of the capacitors in the network to one polarity. A physical power supply unit was built and was able to provide a 10 pulse per second output. The average arc current, $\overline{I_{arc}}$, could be found from

$$\overline{I_{arc}} = \frac{t_{on}}{t_{on} + t_{off}} I_{arc} = PRF t_{on} I_{arc} \tag{2-6}$$

where t_{on} is the time duration of the current, t_{off} is the time between the current pulses, I_{arc} is the arc current, and PRF is the pulse repetition frequency. A 1 kV supply voltage and a 2 k amp arc current were used in the reference 9 laboratory. The pulse duration was approximately 600 micro-seconds. The average current was 12 amps. A history of approximately 10^7 arcs was demonstrated. The low plasma resistance and high supply voltage were listed as characteristics providing reliable pulsed operation.

A review of other power supply techniques was made in reference 9. It was mentioned that the amount of plasma created by the arc is proportional to the arc current. A dc supply could provide currents of around 100 amps. The reference 9 power supply current was, again, an average of around 12 amps.

Anders, et al, discussed pulsed vacuum arcs in reference 10. A voltage pulse of around 10 kV with a duration of a few microseconds might be used to create a "flash over" between a cathode and trigger electrode. Cathode spots are created that produce a plasma. The plasma allows for a main arc between the cathode and anode. This "High-voltage flashover" technique can be reliable, but problems can still occur. Deposition of macroparticle material between the cathode and trigger electrode can short the path preventing subsequent plasma formation for the main arc. In addition, high voltage equipment is needed, which could adversely impact the design of a propulsion unit for spacecraft applications. Contaminating material from the insulator or trigger electrode is a third problem that can occur with an arc trigger method.

A method of initiating a vacuum arc without the trigger mechanism was developed. It utilizes a conducting film on the surface of the insulator between the

cathode and anode. When the arc voltage is applied, joule heating occurs and a plasma is created at the interface between the cathode and the conducting film. This triggerless technique can work with a 500 volt pulse instead of the higher 10 kV value. The vacuum arc then tends to redeposit some material on the insulator between the cathode and anode. In this way, the conducting film is regenerated for the next arc pulse. An isolation transformer and trigger electrode are not needed, but a switch for the power supply is necessary to control the arc initiation.

Anders, et al, reported on experimental results. The triggerless method of arc initiation has a high reliability as demonstrated by a history of over a million pulses. Specific parameters tested included an arc voltage up to 1200 volts, a pulse duration of 250 micro-seconds, and a pulse frequency of 1 to 5 Hz. A titanium conducting film with a thickness of $1x10^{-6}$ m on the surface of the insulator was demonstrated experimentally. Additional tests were conducted with a 20 Hz pulse frequency, a 300 amp arc, a 1.5 micro-second pulse rise time, and a 4 micro-second pulse fall time. A history of 100,000 pulses showed the reliability of the arc triggering method. The use of low melting point materials can produce macroparticles, which could then electrically short the system if deposited in excess between the cathode and anode. Acceptable values of the resistance of the conductive film between the cathode and anode could be from 1 ohm to 100,000 ohms. Voltages of from 600 to 1000 volts are best for good arc initiation reliability.

Qi, et al, discussed micro-thrusters specifically for small satellite applications in reference 11. Ion engines and Hall thrusters may not scale down well to small sizes. Pulsed Plasma Thrusters utilizing a high voltage capacitor might also suffer from a low

thrust to mass ratio. A vacuum arc micro-thruster using inductive energy storage requires lower mass and could be an improvement. Qi, et al, further discussed characteristics of vacuum arcs. A plasma plume is produced from a metallic cathode and emanates from cathode spots. Plasma stream speeds of 10,000 to 30,000 m/sec are possible with resulting specific impulse values of 1,000 to 3,000 sec. The ions are usually singly, doubly, or triply charged. The arc current, duration, and frequency have wide variability. Vacuum arc micro-thrusters can be as small as 0.1 kg.

Qi, et al, reported further on actual experiments conducted using a vacuum arc micro-thruster. The physical arrangement included a thin cathode rod concentrically located inside a cylindrical anode with an insulator separating them. The arc was initiated by applying a voltage pulse across a thin, conducting graphite layer applied to the surface of the insulator. When the pulse started, plasma was produced at the interface between the conducting graphite and the cathode. Arc initiation between the cathode and anode followed. Once break down occurred, the arc voltage dropped to values between 20 and 40 volts. The arc pulse duration was around 250 micro-seconds.

Measurements were made of plasma stream velocities for different cathode materials. The values were found to range from 11,100 to 29,900 m/sec. Qi, et al, discussed three acceleration mechanisms for these high speeds. The first comes from an electric field force. The second comes from collisions between ions or between ions and neutrals, or the pressure gradient. The third, and largest, comes from collisions between electrons and ions. The ion speeds were much higher than the acoustic speed in the plasma. The ion kinetic energy values ranged from 20 to 200 eV. Vacuum arcs tend to

have an ion current that is about 10% of the total arc current. Qi, et al, measured 7.8% for tungsten. A time-of-flight technique was used to determine the ion charge states for various materials. The average ion charge state values ranged from +2 to +3. Cathode erosion rates were also measured. The values ranged from 20 to 60 micro-grams per Coulomb of charge through the arc. The cathode erosion includes ionized material, or plasma, neutral atoms, and macro-particles.

Qi, et al, used the experimental data to estimate efficiency for a vacuum arc thruster. The overall efficiency was determined from

$$\eta = \eta_{PPU}\eta_{arc\_energy}\eta_{propellant} \tag{2-7}$$

The efficiency of the power processing unit, η_{PPU}, was estimated as 92%. The energy efficiency, η_{arc_energy}, reflects the output plasma kinetic energy as a fraction of the input electrical arc energy. This efficiency was expressed as

$$\eta_{arc\_energy} = \frac{\frac{1}{2}\dot{m}_{arc}v^2}{I_{arc}V_{arc}} \tag{2-8}$$

where $\dot{m}_{arc}$ is the plasma ion mass flow rate, v is the ion velocity, I_{arc} is the arc current, and V_{arc} is the arc voltage. Qi, et al, determined an energy efficiency value for a tungsten arc as approximately 17%. The propellant efficiency, $\eta_{propellant}$, reflects the ratio of the plasma flow rate to the total cathode mass flow rate as

$$\eta_{propellant} = \frac{\dot{m}_{arc}}{\dot{m}_{cathode}} \tag{2-9}$$

Qi, et al, reported this value as approximately 83%. The overall efficiency was then listed as approximately 13%. A thrust, T, to power, P, ratio was also determined by

$$\frac{T}{P} = \frac{\dot{m}_{arc} v}{I_{arc} V_{arc}} \eta_{PPU} \quad (2\text{-}10)$$

The value obtained for a tungsten arc was approximately 22 micro-N/Watt. Qi, et al, concluded that a vacuum arc thruster could be practical for some satellite applications.

The use of micro and nano propulsion for small satellite applications was also discussed by Schein, et al, in references 12 and 13. It was mentioned that a low propellant efficiency and operating voltages of a few thousand volts limit the thrust efficiency of pulsed plasma thrusters (PPTs) to less than 10%. Another disadvantage is the need for a large, high voltage capacitor in the power processing unit (PPU). A vacuum arc thruster (VAT) that uses inductive energy storage, however, avoids these disadvantages.

The physical thruster configuration described in references 12 and 13 utilized an inductive energy technique to create a voltage spike across a thin, conducting graphite layer on the insulator separating the anode and cathode. The opening of a switch in series with an inductor, L, created a voltage spike, L*dI/dt, where L is the inductance and I is the current. The current through the graphite then produced the initial plasma near the graphite to cathode interface. This plasma then allowed for a full arc between the cathode and anode. The cathode would erode and some of the plasma produced from the arc would redeposit on the insulator between the anode and cathode. The cycle could then be repeated for additional pulses. Without the need for large capacitors, the overall mass of the VAT was low.

Schein, et al, reported on testing results of the VAT configuration with several different cathode materials. As mentioned in reference 11 also, the plasma velocity ranged from 11,100 to 29,900 m/sec. Again, the ion charge states varied from +2 to +3 and the cathode erosion rates varied from 20 to 60 micro-grams per Coulomb of charge. In the same fashion as in reference 11, the overall efficiency for the tungsten cathode material case was listed as approximately 13%. In references 12 and 13, the thrust to power ratio for the tungsten cathode was given as approximately 18.2 micro-N/Watt. A high precision thrust stand in a vacuum chamber was used to experimentally measure the VAT thrust down to the micro-N level. Thrust measurements for a titanium cathode resulted in a value of 2.2 micro-N/Watt. A calculated estimate for the titanium thrust to power ratio was 6.7 micro-N/Watt. It was reported in reference 12 that the thrust to power ratio is affected by the ion to arc current ratio. This current ratio is also affected by the anode/cathode geometry. In addition, the plasma exhaust tends to diverge from the thruster. Taking these factors into account could then produce an estimated thrust to power ratio more closely in agreement with the measured value. The efficiency of the titanium cathode VAT was estimated as 1.6%. This value is much less that the 13% for the tungsten cathode VAT. Schein, et al, felt that the geometric configuration of the cathode recess could be used to increase the ion to arc current ratio. A higher current ratio could then result in an overall efficiency of 7% for the titanium VAT. Schein, et al, concluded that proper geometric design of the VAT and the use of heavier cathode materials than titanium would actually result in a thrust to power ratio of approximately 20 micro-N/Watt and an efficiency of approximately 15%. It was concluded in reference 13 that the VAT is an efficient means of electrical propulsion. It has the advantages of

being able to use various materials for the cathode and a low arc initiation voltage, having a low total mass, and eliminating the need for a capacitor.

Polk, et al, provided analyses of vacuum arc thruster and vacuum arc ion thruster operation in reference 14. A number of advantages of vacuum arcs were mentioned. The plasma is created very efficiently in a cathode spot. This plasma production is scalable to very small sizes for micro-propulsion applications. Operation can be pulsed so the duty cycle is easily varied. Additionally, since the solid cathode serves as the propellant source, mechanical simplicity is possible. Valves are not needed and the thruster can be small and lightweight.

A basic measure of a vacuum arc thruster is the mass erosion rate of the cathode. It was stated in reference 14 that at low energy levels, the total mass erosion rate is proportional to the arc discharge current. Higher current levels or longer pulses could result in large scale melting of the cathode material. Polk, et al, stated that as demonstrated by experimental data, the ion current is a nearly constant 0.07 to 0.1 fraction of the arc discharge current. Experimental data also indicated that the charge state distribution tends to be constant after the initial production of the plasma and once it moves away from the cathode spot. It was suggested in reference 14 that acceleration of the plasma is caused by gas dynamic forces and possibly electrostatic forces also. Further experimental findings indicated that the ion current density has a cosine or exponential type distribution about an axis perpendicular to the cathode surface. Experimental evidence also indicated that the ion velocity tends to be constant for any specific material.

Polk, et al, defined the power consumption for a vacuum arc thruster as the product of the arc discharge current and the arc discharge voltage. The total efficiency was then defined as the exhaust kinetic power divided by the input power. The thrust and thrust to power ratio were found to vary with the ion mass, the ion current fraction, the exhaust velocity, and the inverse of the charge state distribution of the ions. The total efficiency varied with these thrust factors squared. It was pointed out in reference 14 that these factors are dependent on the specific cathode material.

It was reported in reference 14 that some of the best performing cathode materials were chromium, yttrium, tantalum, and tungsten. The efficiencies for these materials in a vacuum arc thruster were listed optimistically as varying from 0.07 to 0.12 and the specific impulses as varying from 860 to 1660 seconds. More realistic estimates might be 0.02 to 0.04 lower for the efficiencies and 100 to 200 seconds lower for the specific impulses. Polk, et al, mentioned several aspects regarding the successful use of vacuum arcs for propulsion. Arc initiation must be reliable for a high number of repeated pulses in order to achieve a long thruster lifetime. The cathode must be uniformly consumed and then advanced as it is consumed. In addition, the possibility of contamination of the spacecraft from the plasma plume must be considered.

Chapter 3 – Equipment Description and Operation

The Micro-Cathode Vacuum Arc Thruster (μCAT) intended for this study was one developed in the George Washington University (GWU) Micropropulsion and Nanotechnology Laboratory (MpNL). The device is operated in a vacuum chamber. A general schematic of the major μCAT components is shown in Figure 3-1.

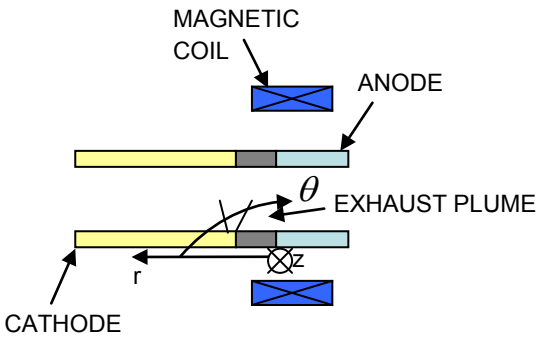

Figure 3-1: Micro-Cathode Vacuum Arc Thruster Major Components

The main μCAT body is composed of cylindrical titanium electrodes for the cathode and anode separated by a cylindrical insulator. The cathode, insulator, and anode are positioned next to each other on a common axis. Electrical energy is supplied from an inductive power processing unit to initiate an arc between the cathode and anode. The μCAT operates in a repeating pulsed mode. A cathode spot at one end of the arc forms near the interface between the cathode and insulator. A plasma plume that consists of the ablated cathode titanium ions and electrons initiates from the cathode spot. The plume then expands into the cylindrical body of the μCAT. An external magnetic field is applied with a solenoid coil positioned around the tube structure of the μCAT. The

magnetic field curves through the interior chamber in the theta direction and helps to turn the charged particles of the plasma plume arc jet in the direction of the field and then along the cylinder axis. A steel core is positioned on the side of the magnetic coil closest to the cathode in an effort to tighten the curvature of the magnetic field. In this way, the plume turns from the cathode spot and through the anode to exhaust out of the μCAT structure and provide useful thrust. With repeated pulses, the cathode experiences an ablation of its material along its circumference near the insulating ring. As the cathode is consumed during operation, it is pushed toward the insulator and anode by a spring. In this way, a longer cathode can be used resulting in longer life for the μCAT.

An electrical schematic of the μCAT is shown in Figure 2-2.

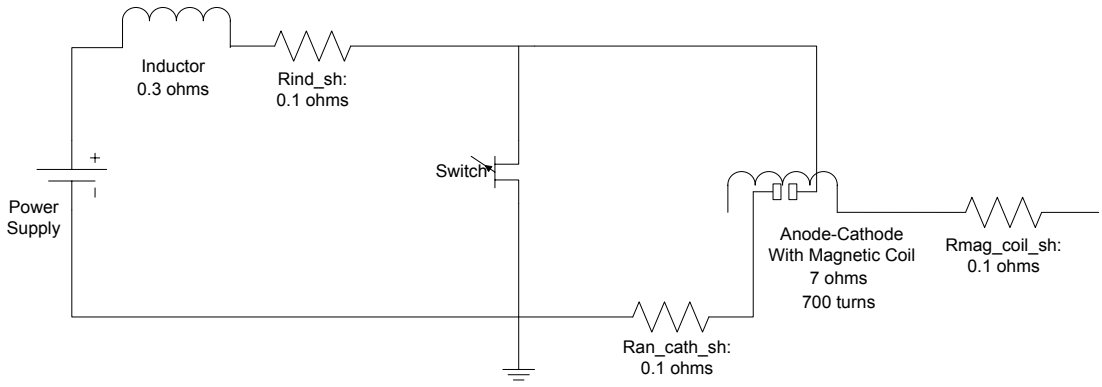

Figure 3-2: Micro-Cathode Vacuum Arc Thruster Electrical Schematic

The power supply provides a current through the inductor and switch. When the switch is opened, a large voltage spike is created across the anode and cathode resulting in the electric arc.

Chapter 4 – Experiments Conducted

4.1 Experiments for Thruster Impulse and Exhaust Velocity

A variety of physical experiments were performed with the actual μCAT. First, thruster impulse measurements were made for various voltages applied to the magnetic field coil around the anode and cathode. The higher voltages in the coil produced higher magnetic field strengths. The thruster impulse values vs. the magnetic coil voltages are shown in Figure 4-1.

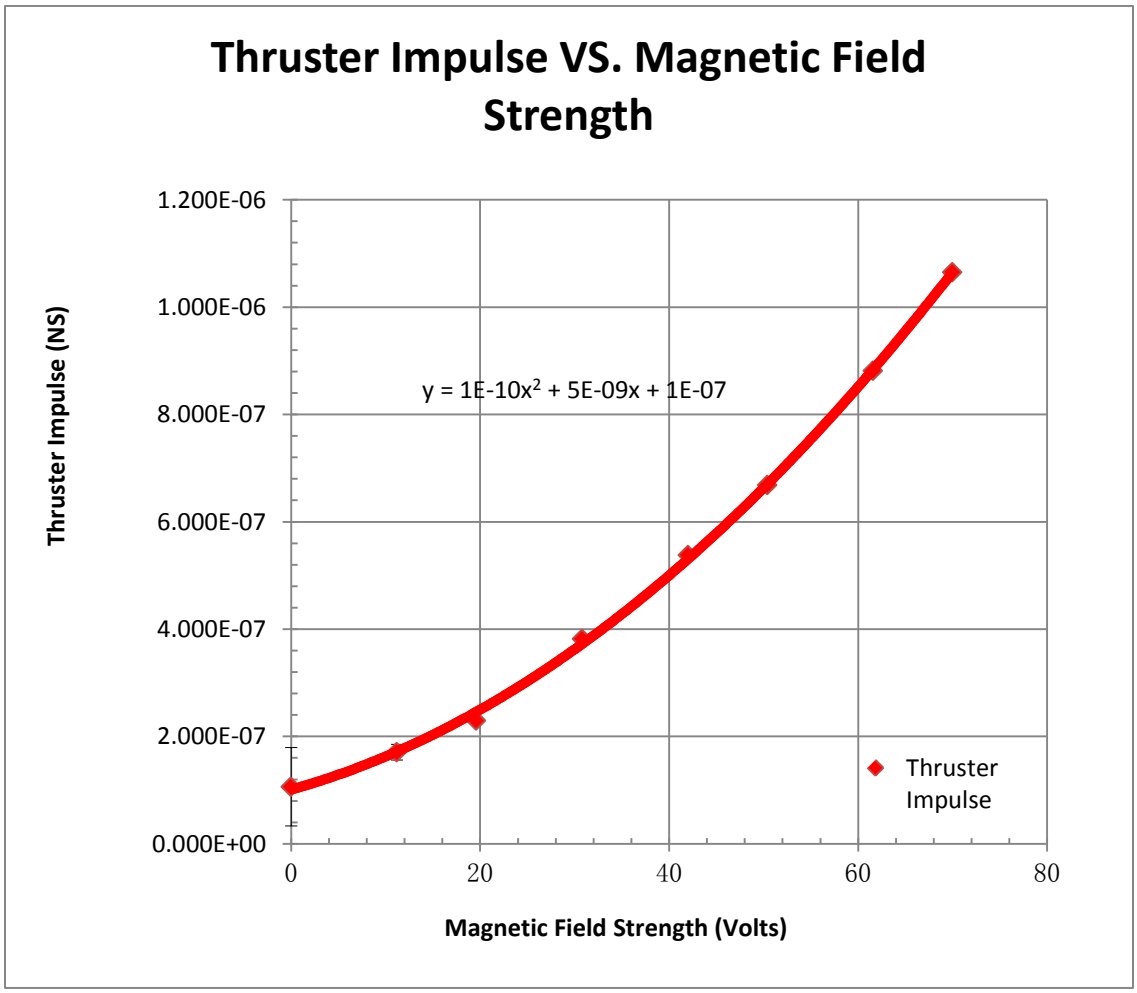

Figure 4-1: Thruster Impulse vs. Magnetic Field Strength

The Figure 4-1 plot was made with Microsoft Office Excel and the second order polynomial descriptive curve function was provided by the program's graphing facility. The improved thruster impulse with increasing magnetic field is clearly seen. Second, thruster exhaust velocity measurements were made for a number of magnetic field coil voltages. These results are shown in Figure 4-2.

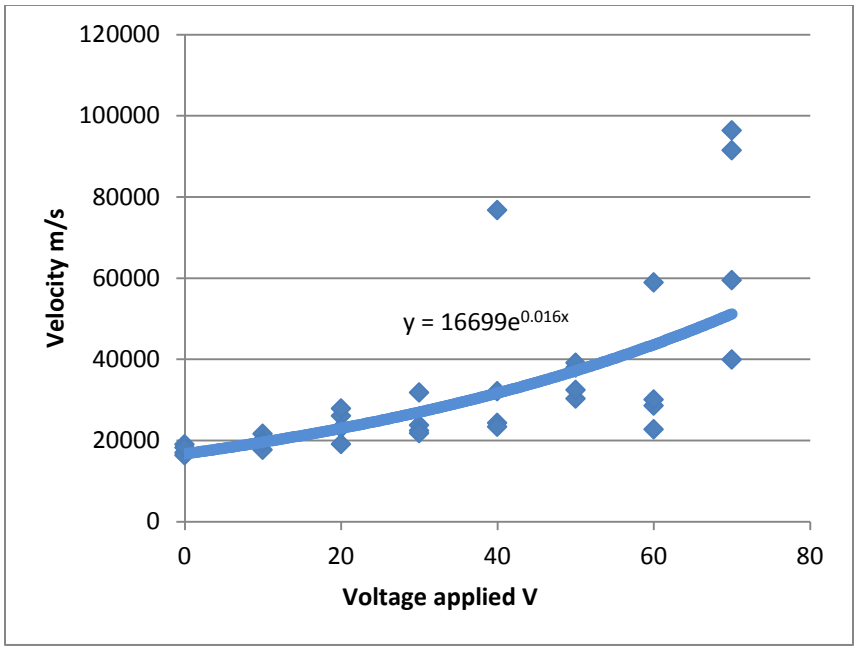

Figure 4-2: Thruster Exhaust Velocity vs. Magnetic Field Strength

There is a wider scatter of velocity data than there was for the thruster impulse data. Nevertheless, a trend of increasing exhaust velocity with increasing magnetic field strength is apparent. The curve fitting function was again provided by the Excel program. A specific physical relationship between exhaust velocity and the magnetic field strength, or voltage on the magnetic field coil, is not necessarily evident from the data. The polynomial and exponential functions listed simply provided for computational convenience.

4.2 Experiments for Thruster Energy

The impulse and velocity can be used to calculate the mechanical energy in the thruster plume. Thrust can be represented as the time rate of change of linear momentum.

$$Thrust = \frac{d(mV)}{dt} \tag{4-1}$$

where m is propellant mass and V is the exhaust velocity. The equation can also be written as

$$Thrust = \frac{\Delta(\mathrm{mV})}{\Delta t} \tag{4-2}$$

Then

$$Impulse = Thrust * \Delta t = \Delta(mV) \tag{4-3}$$

The energy in the plume, E_{plume}, is expressed as kinetic energy.

$$E_{plume} = \frac{1}{2} mV^2 \tag{4-4}$$

Substituting

$$Impulse = mV \tag{4-5}$$

and using I for impulse gives

$$E_{plume} = \frac{1}{2} IV \tag{4-6}$$

The experimental values for impulse and exhaust velocity are both available from Figures 4-1 and 4-2 for various magnetic field strengths.

In addition to the impulse and velocity, electrical measurements were made to determine other energy quantities used in various parts of the μCAT. A major area was to determine the arc energy between the anode and cathode vs. the magnetic field coil

voltage. Several sets of data were recorded. One method involved taking voltage measurements across the 0.1 ohm $R_{an\_cath\_sh}$ resistor in series with the anode-cathode arc and additional voltage measurements across the arc itself. These measurements were repeated every 2.0e-7 sec for a total of 2500 data points. The voltage readings across the shunt resistor provided the current in the arc according to Ohm's Law:

$$I_{arc} = V_{sh}/R_{an\_cath\_sh} \tag{4-7}$$

The current values at each time step were then used as input with the arc voltage measurements to find the energy in the arc according to Watt's Law:

$$E_{arc} = V_{arc} * I_{arc} * deltaT \tag{4-8}$$

These arc energy values were totaled for the time steps to determine the energy in one arc pulse. Two methods were tried. One involved totaling all 2500 time step arc energy values. The second involved totaling only the time step arc energy values for the portion of the arc voltage vs. time curves between two major voltage spikes. The arcs typically started and ended with rather sharply defined spikes. Graphs of these curves are shown in Appendix A. The voltage is on the vertical scale and the time is on the horizontal scale. The CH1 trace (orange) is for the voltage on the 0.1 ohm shunt resistor and provides an indication of the arc current. It rises sharply upward at the start and then has a gradual decay. The CH2 trace (blue) is for the voltage across the anode-cathode. The starting and ending spikes can be seen and were determined by manually reviewing the data in the Excel spreadsheets. The total arc energy from the portion of the curve between the voltage spikes was usually only slightly less than the total arc energy from the entire curve. The total arc energy values from between the voltage spikes were used

in efficiency calculations. These arc energy experiments were conducted for magnetic field coil values of 0, 10, 20, 30, 40, 50, 60, and 70 volts.

Another method for determining the arc energy involved taking voltage measurements across the 0.1 ohm shunt resistor again to determine the current in the arc. For these experimental trials, however, the voltage across the arc itself had to be assumed. Each experimental run had 600,000 measurements taken for a 60 second period. The time step duration was therefore 0.0001 sec. The current in the arc was found by the same method of using the voltage readings across the shunt resistor and Ohm's Law.

$$I_{arc}\ (for\ each\ time\ step) = \frac{V_{shunt}\ (for\ each\ time\ step)}{R_{shunt}} \tag{4-9}$$

The 600,000 voltage readings were summed in an Excel spreadsheet to work with the experimental trial in a simpler calculation.

$$\sum_{1}^{600,000} I_{arc} = \frac{\sum_{1}^{600,000} V_{shunt}}{R_{shunt}} \tag{4-10}$$

Then for the arc energy where U_{ad} is the assumed value for the arc discharge voltage,

$$\sum_{1}^{600,000} E_{arc} = U_{ad} * \sum_{1}^{600,000} I_{arc} * deltaT \tag{4-11}$$

Each trial run of 60 seconds included 14 arc pulses. So the arc energy per pulse was found from

$$TotalE_{arc} = \frac{\sum_{1}^{600,000} E_{arc}}{14} \tag{4-12}$$

These arc energy values per pulse were used in additional efficiency calculations. These particular arc energy trials were conducted for magnetic field coil values of 0, 11.2, 19.6, 30.8, 42, 56, 61, and 70 volts. For each of these magnetic field coil voltage settings

except the 56 volt case, five 60 second shots (with 14 arc pulses each) were conducted. The 56 volt magnetic field case had ten 60 second shots. Data was recorded in Excel files and the calculation results were then averaged for the five or ten shots at each of the eight magnetic field coil voltage values.

Another major area of energy use in the μCAT was the electrical energy in the magnetic field coil. Several sets of data were taken in this area as well. Voltage measurements were taken across the 0.1 ohm $R_{mag\_coil\_sh}$ resistor in series with the magnetic field coil. These measurements were repeated every 4.0e-6 sec for a total of 2500 data points. The voltage readings across the shunt resistor provided the current in the coil according to Ohm's Law again:

$$I_{coil} = V_{sh}/R_{mag\_coil\_sh} \tag{4-13}$$

The energy in the inductor coil can then actually be divided into two components. The main component of interest is the magnetic field energy. The other component is the resistive energy losses in the coil wiring.

The magnetic energy can be found by considering the power supplied to the coil.

$$P_{coil} = V_{coil} * I_{coil} \tag{4-14}$$

This voltage on the coil is found from

$$V_{coil} = L * \frac{dI_{coil}}{dt} \tag{4-15}$$

where L is the inductance of the coil. Then

$$P_{coil} = L * \frac{dI_{coil}}{dt} * I_{coil} \tag{4-16}$$

This power to the coil is the rate of inductor energy, so

$$\frac{dE_{coil}}{dt} = L * \frac{dI_{coil}}{dt} * I_{coil} \tag{4-17}$$

Or

$$dE_{coil} = L * I_{coil} * dI_{coil} \tag{4-18}$$

This expression can be discretized as

$$\Delta E_{coil} = L * I_{coil} * \Delta I_{coil} \tag{4-19}$$

Then by summing up the individual current measurements and delta current values between successive measurements, the experimental estimate for the magnetic coil energy can be obtained.

$$E_{coil\_mag} = L * \sum_{initial}^{final} (I_{coil} * \Delta I_{coil}) \tag{4-20}$$

The initial value for the sum is at the start of the data recording. The value is near zero. The final value is taken at the peak of the current vs. time curve. The arc is fired close to this maximum point when the magnetic field is the strongest. These field coil measurements were conducted for magnetic field coil values of 10, 20, 30, 40, 50, 60, 70, 80, and 90 volts. The signal vs. time curve shows a somewhat asymptotic rise to a peak value. Graphs of these curves are shown in Appendix B. The voltage/current signal is on the vertical scale and the time is on the horizontal scale. Another estimate of the magnetic energy from the coil can be found from integrating the dE_{coil} expression.

$$\int_0^{total} dE_{coil} = \int_0^{I_{coil\_final}} L * I_{coil} * dI_{coil} \tag{4-21}$$

where I_{coil_final} is the final current value at the peak of the current vs. time curve. Then

$$E_{coil} = \frac{1}{2} L * I_{coil\_final}^2 \tag{4-22}$$

The inductance of the magnetic field coil can be estimated from the inductance formula for a solenoid.

$$L = \mu_0 \mu_r N^2 \frac{A}{l} \tag{4-23}$$

The value for the permeability of free space, μ_0, was taken as

$$\mu_0 = 4\pi * 10^{-7} \tag{4-24}$$

in henries/m. The value of μ_r was 1.0. N is the number of turns on the anode-cathode coil. The GWU μCAT has 700 turns. The area of the coil is A and the length of the coil is l. The area was found using an average of the 0.184 inch inner radius and the 1.0 inch outer radius.

$$A = \pi r_{ave}^2 \tag{4-25}$$

The coil length was 0.681 inches.

The resistive energy losses in the coil wiring can be found from the same current values at each time step along with the magnetic field coil resistance.

$$E_{coil\_res} = I_{coil}^2 * R_{coil} * deltaT \tag{4-26}$$

The resistance of the coil, R_{coil}, was provided as an experimental value of 7 ohms. These coil energy values were totaled for the same portion of the available time steps to determine the coil resistive energy expended for one pulse.

$$E_{coil\_res} = \sum_{initial}^{final} I_{coil}^2 * R_{coil} * deltaT \tag{4-27}$$

With values for mechanical plume energy, the electrical arc energy, and the magnetic and resistive energies in the magnetic field coil, various efficiency values were calculated.

Chapter 5 – Experimental Data

5.1 Summary of Experiments Conducted

In addition to tests of the thruster impulse and exhaust velocity, measurements were also made of some of the electrical parameters. Table 5-1 shows the specific magnetic field coil voltages that were used for the different experiments. The first two columns show the field coil voltages tried for arc energy determination and the third column shows the field coil voltages tried for the coil energy determination.

Magnetic Field Coil Voltage (volts) (Arc Energy Experiments)	Magnetic Field Coil Voltage (volts) (Arc Energy – 14 Pulses Experiments)	Magnetic Field Coil Voltage (volts) (Magnetic Field Coil Energy Experiments)
0	0 (5 cases)	
10	11.2 (5 cases)	10
20	19.6 (5 cases)	20
30	30.8 (5 cases)	30
40	42 (5 cases)	40
50	56 (10 cases)	50
60	61 (5 cases)	60
70	70 (5 cases)	70
		80
		90

Table 5-1: Magnetic Field Coil Voltages for the Various Experiments

5.2 Mechanical Plume Energy from the Thruster Impulse and Exhaust Velocity

The mechanical plume energy is needed for each of the magnetic field coil voltages that were tested. The plume energy was found from

$$E_{plume} = \frac{1}{2} IV \tag{5-1}$$

The impulse, I, was found from the curve fit equation

$$I = (1E-10)V_{mag}^2 + (5E-09)V_{mag} + (1E-07) \tag{5-2}$$

where V_{mag} is the voltage on the magnetic field coil. The exhaust velocity, V, was found from

$$V = 16699e^{0.016V_{mag}} \quad (5\text{-}3)$$

The calculated plume energy values for the different magnetic field coil voltages are shown in Table 5-2.

Magnetic Field Coil Voltage (volts)	I (impulse in Ns)	V (exhaust velocity in m/s)	E_{plume} (joules)
0	0.0000001	16699	0.00083495
10	0.00000016	19596.45803	0.001567717
11.2	1.68544E-07	19976.34528	0.001683447
19.6	2.36416E-07	22849.9479	0.002701047
20	0.00000024	22996.65654	0.002759599
30	0.00000034	26986.82644	0.00458776
30.8	3.48864E-07	27334.47804	0.004768008
40	0.00000046	31669.3342	0.007283947
42	4.864E-07	32699.14195	0.007952431
50	0.0000006	37164.30796	0.011149292
56	6.936E-07	40908.94885	0.014187223
60	0.00000076	43612.71941	0.016572833
61	7.771E-07	44316.13524	0.017219034
70	0.00000094	51180.00034	0.0240546
80	0.00000114	60060.28678	0.034234363
90	0.00000136	70481.39945	0.047927352

Table 5-2: Mechanical Plume Energy vs. Magnetic Field Coil Voltage

The plume energy data in Table 5-2 is plotted in Figure 5-1.

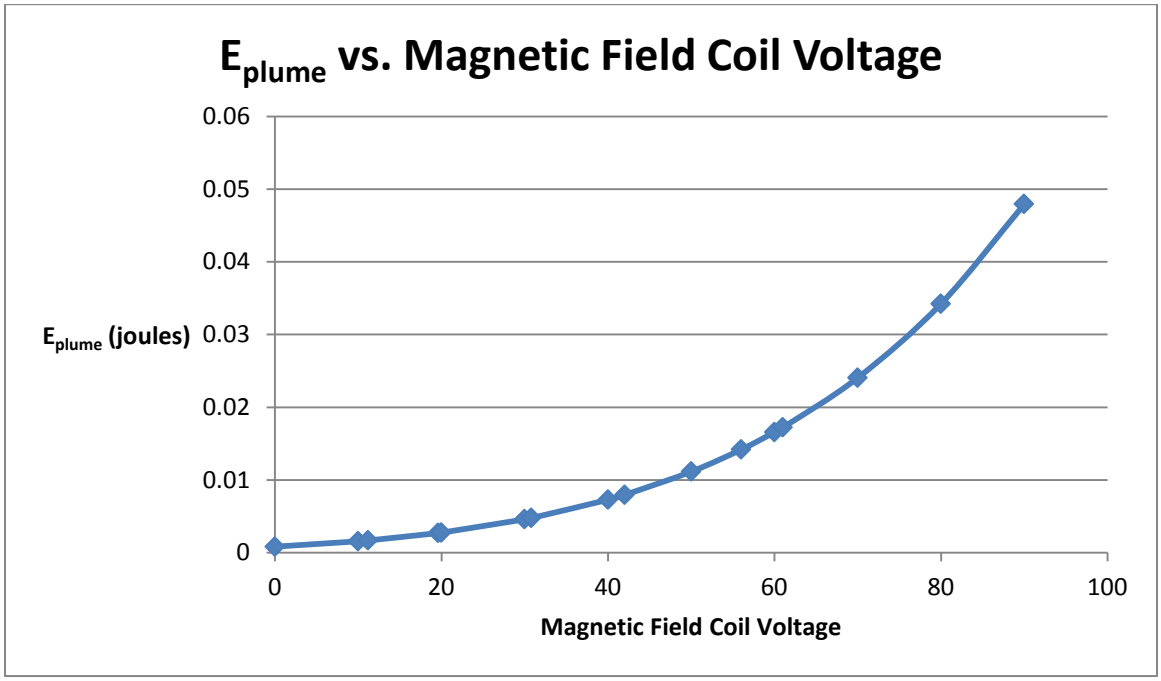

Figure 5-1: E_{plume} vs. Magnetic Field Coil Voltage

The impulse and velocity components that make up the mechanical plume energy are both measured quantities. Figure 5-1 shows the increase of E_{plume} with respect to the magnetic field coil strength. This mechanical plume energy increase shows that the magnetic field functions as desired in turning the plasma plume from the cathode spot in the direction of the thruster axis.

5.3 Electrical Arc Energy

The experimental trials involving specific arc current and arc voltage measurements at discrete time sampling points to determine the arc energy resulted in two totals. One was for the entire set of data points and the other was for the segment of

data between the anode-cathode arc voltage spikes. These summed arc energy values for the different magnetic field coil voltages are shown in Table 5-3 along with the total duration of the pulse.

Magnetic Field Coil Voltage (volts)	Summed Arc Energies (joules)		Total Pulse Duration (sec)
	Total	Between Volt Peaks	
0	0.25292864	0.24179248	0.0003318
10	0.24157392	0.23158256	0.0003328
20	0.21274416	0.20417352	0.000214
30	0.21151368	0.20067896	0.0001825
40	0.21479296	0.20454416	0.0001768
50	0.20967952	0.19831512	0.000151
60	0.20375912	0.19158232	0.0001392
70	0.18894912	0.17726408	0.0001088

Table 5-3: Summed Electrical Arc Energies vs. Magnetic Field Coil Voltage

The arc energy values calculated from the measured data between the starting and ending arc voltage spikes have been plotted in Figure 5-2. In addition, the total time for the electric arc pulse between the same starting and ending arc voltage spikes have been plotted in Figure 5-3. The blue CH2 curves in the figures in Appendix A show the location of the voltage spikes (peaks).

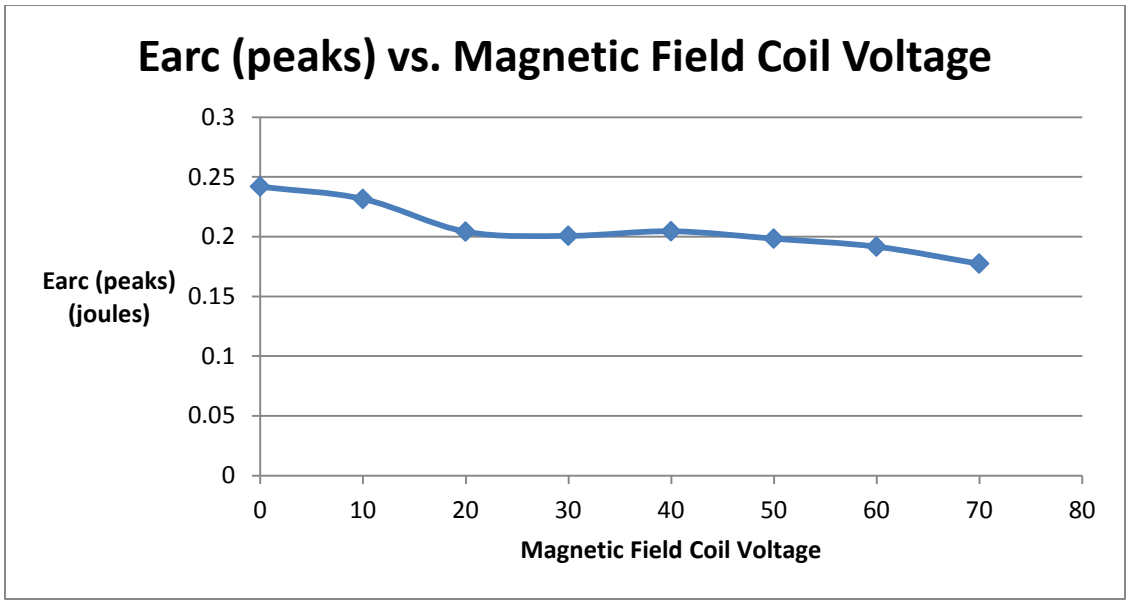

Figure 5-2: E_{arc} (peaks) vs. Magnetic Field Coil Voltage

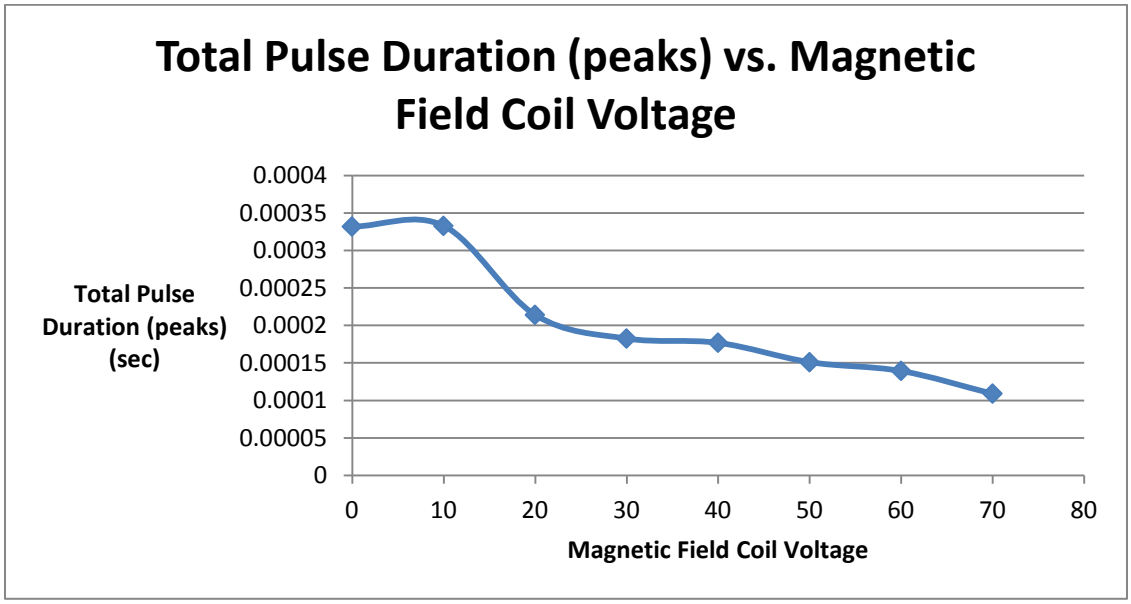

Figure 5-3: Total Pulse Duration (peaks) vs. Magnetic Field Coil Voltage

For use in calculating arc energy values on some of the other experimental data sets, the measured arc voltages can be used to determine average arc voltages for each of the specific magnetic field coil voltages (0, 10, 20, 30, 40, 50, 60, and 70 volts). These

averages can then be used to determine interpolated arc voltages for the specific magnetic field coil voltages of the other experimental trials (0, 11.2, 19.6, 30.8, 42, 56, 61, and 70 volts). These other trials did not have measured arc voltages vs. time. Constant arc voltage values had to be assumed for these cases. The average and interpolated arc voltages for the various magnetic field coil voltages are shown in Table 5-4.

Magnetic Field Coil Voltage (volts)	Average V_{arc} (volts)	Interpolated V_{arc} (volts)
0	61.86738999	
10	58.76923077	
11.2		61.19804457
19.6		78.19974119
20	79.00934579	
30	89.61534247	
30.8		89.76530059
40	91.489819	
42		92.91715322
50	98.62649007	
56		102.6936995
60	105.4051724	
61		107.8277066
70	129.6305147	

Table 5-4: Arc Voltage (Average and Interpolated) vs. Magnetic Field Coil Voltage

A graph of V_{arc} vs. the magnetic field coil voltage is shown in Figure 5-4.

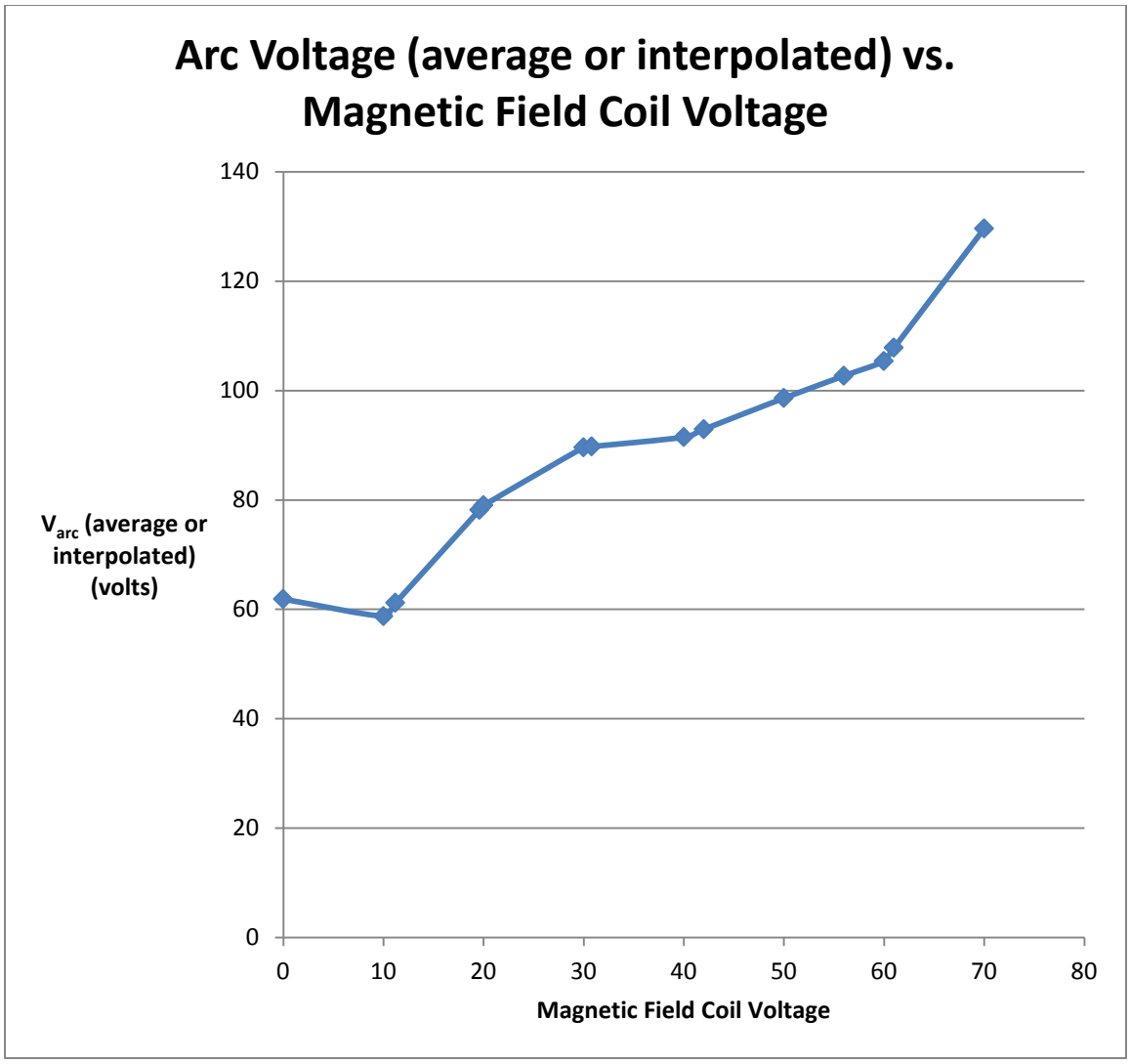

Figure 5-4: Arc Voltage (average or interpolated) vs. Magnetic Field Coil Voltage

While the arc voltage increases with an increased magnetic field strength, the arc energy, E_{arc}, still decreases somewhat. This decrease may be due to the shorter arc pulse duration as seen in Figure 5-3.

The experimental trials involving specific arc current measurements at discrete time sampling points and the assumed constant arc voltage values from averaging and interpolation provided additional indications of arc energy at different magnetic field coil strengths. These sets of data involved repeated trials at each magnetic field coil voltage.

The average arc energy values for the different magnetic field coil voltages are shown in Table 5-5.

Magnetic Field Coil Voltage (volts)	Number of Repeated Trials	Average Arc Energies (joules)
0	5 shots of 14 pulses	0.206949987
11.2	5 shots of 14 pulses	0.122142394
19.6	5 shots of 14 pulses	0.148950845
30.8	5 shots of 14 pulses	0.125159275
42	5 shots of 14 pulses	0.132475769
56	10 shots of 14 pulses	0.095527321
61	5 shots of 14 pulses	0.111910371
70	5 shots of 14 pulses	0.163570289

Table 5-5: Averaged Electrical Arc Energies vs. Magnetic Field Coil Voltage

These average arc energy values have been plotted in Figure 5-5.

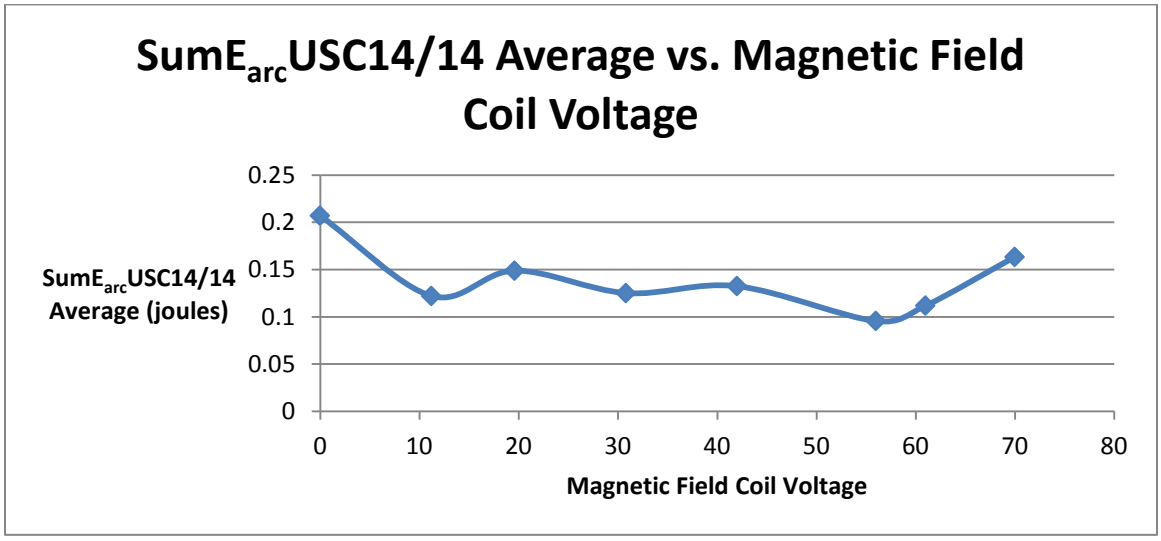

Figure 5-5: Average Arc Energy vs. Magnetic Field Coil Voltage

A slight downward trend of these arc energy values with increasing magnetic field strength can be seen. This trend is similar to that shown in Figure 5-2. In this case, the whole curve is slightly lower. The Figure 5-2 data is probably a better estimation since it involved 2,500 time sampling points for each arc pulse. The experimental trials for the Figure 5-5 data involved 600,000 time sampling points for 14 arc pulses, but these pulses were concentrated in the center portion of the file. The pulse frequency was 50 Hz. The experiment was set up and ran for approximately 30 seconds, then 14 pulses were fired, then the experiment completed for a little over 29 additional seconds. Each experiment was for a total of 60 seconds. The time sampling rate was for every 0.0001 sec. Each pulse registered in the data file with only 5 or 6 data points. A representative graph of these pulses is shown in Figure 5-6.

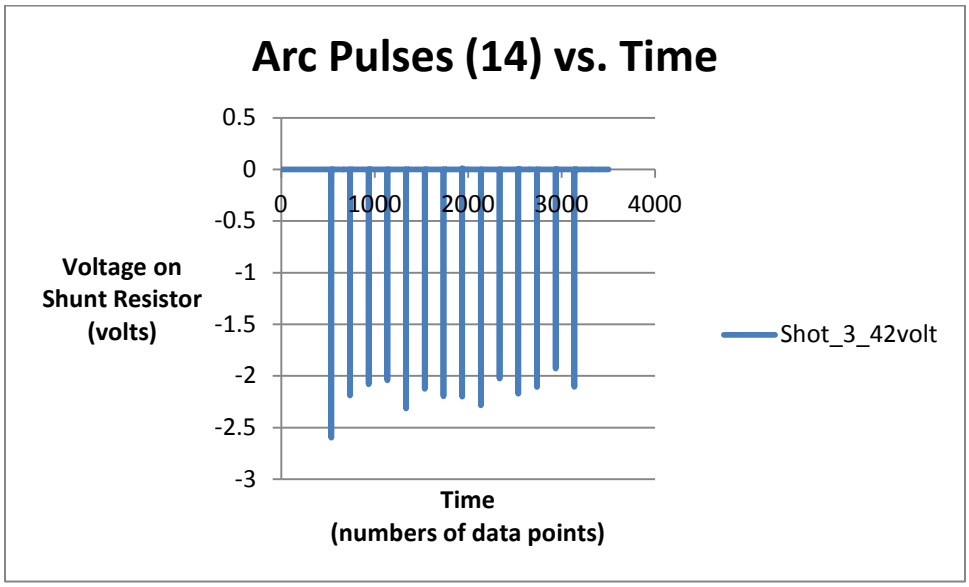

Figure 5-6: Arc Pulses (14) vs. Time

The values are negative only because of the placement of the measuring leads. There is a significant variation in the magnitude of the different pulses. Some of the other trials showed an even greater variation as seen in the plots in Appendix C. The frequency,

however, remained very consistent. The recorded voltage values before and after and also between the pulses was typically around 1.7-9.7e-5. These values are small compared to the values of around 2 recorded during the actual pulses themselves. The values are different by several orders of magnitude. Nevertheless, when adding up the values for 600,000 data points, a sizeable bias is introduced in the results. Therefore, a more accurate treatment was made by using only 3,500 data points around the 14 pulses. In this way, the small amounts resulting from the measurements between the pulses remained small compared to the measurements during the actual pulses.

5.4 Electrical Magnetic Field Coil Energy

Another component of electrical energy used in the μCAT is that in the magnetic field coil itself. The electrical arc energy results in mechanical plume energy, but electrical energy must also be expended in the field coil to create the magnetic field that turns the plume toward the exhaust direction. The magnetic field coil energy has two parts. The first is in the magnetic field and is found from

$$E_{coil\_mag} = L * \sum_{initial}^{final} (I_{coil} * \Delta I_{coil}) \tag{5-4}$$

An alternate method of finding the magnetic field energy involves integrating the equation between the initial (zero) and ending (I_{coil_final}) current values.

$$E_{coil} = \frac{1}{2} L * I_{coil\_final}^2 \tag{5-5}$$

The second part of the magnetic field coil energy is the resistive energy loss, or joule heating, in the wiring. The field coil in the GWU μCAT had a resistance of seven ohms. The resistive energy equation is

$$E_{coil\_res} = \sum_{initial}^{final} I_{coil}^2 * R_{coil} * deltaT \quad (5\text{-}6)$$

These electrical coil energy values for the different magnetic field coil voltages are shown in Table 5-6 along with the final current in the coil.

Magnetic Field Coil Voltage (volts)	Summed Coil Magnetic Energy (joules)	Summed Coil Resistive Energy (joules)	Total Summed Coil Energies (joules)	Alternate Coil Magnetic Energy (joules)	Final (max) Current in Coil (amps)
0	0	0	0	0	0
10	0.074271014	0.068762747	0.143033761	0.048569986	1.96
20	0.142675599	0.251989338	0.394664937	0.136020237	3.28
30	0.386253778	0.564897805	0.951151583	0.33663188	5.16
40	0.586440611	1.059966656	1.646407267	0.557432131	6.64
50	0.993975365	1.67621225	2.670187615	0.943807283	8.64
60	1.344666446	2.483189811	3.827856257	1.305098394	10.16
70	1.838093813	3.373360973	5.211454786	1.724811046	11.68
80	2.293814202	4.457673293	6.751487495	2.202945239	13.2
90	3.15978004	5.1874648	8.34724484	2.695017259	14.6

Table 5-6: Electrical Magnetic Field Coil Energies vs. Magnetic Field Coil Voltage

The average time to reach the final, or maximum, current in the field coil was 0.00624 seconds. The electrical coil energies have also been plotted in Figure 5-7.

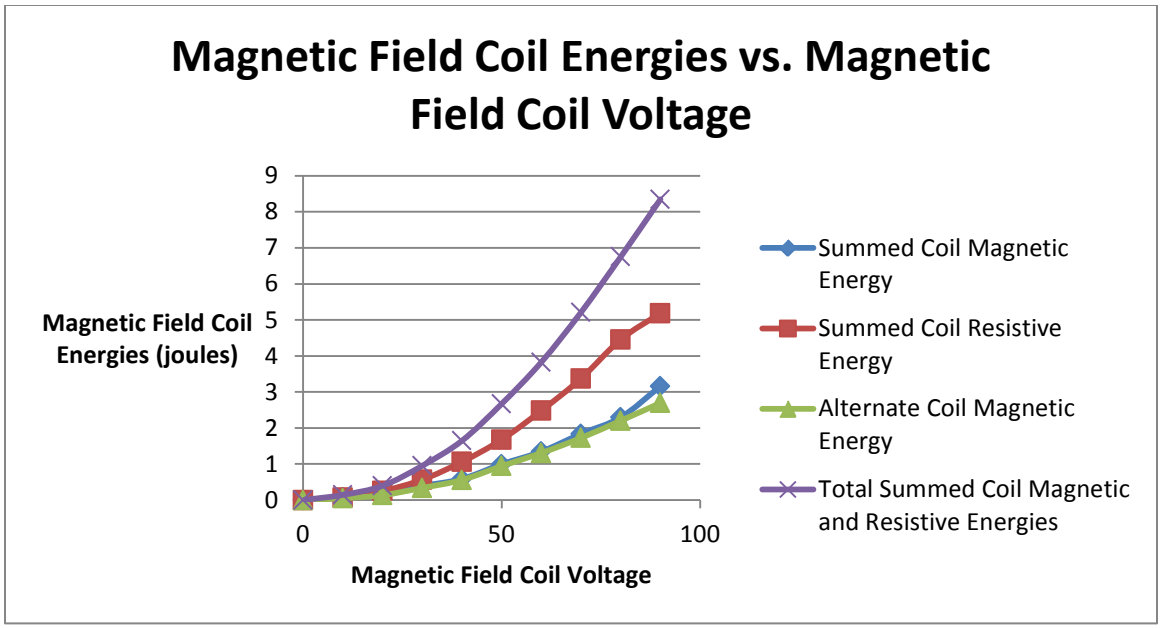

Figure 5-7: Magnetic Field Coil Energies vs. Magnetic Field Coil Voltage

It is apparent that the summed coil magnetic energy data matches closely with the alternate method of calculating this energy based on the $(1/2)*L*(I_{coil\_final})^2$ formula. It is also seen that the energy expended as resistive energy losses is significant. This loss is greater than the magnetic field energy. It is easily seen that the energy used to generate the magnetic field increases with the higher magnetic field coil voltages.

Chapter 6 – Efficiencies

μCAT efficiencies are calculated as the ratio of the mechanical plume energy to various electrical energies used in its operation. The most basic efficiency is Efficiency1 found from this formula

$$Efficiency1 = \frac{E_{plume}}{E_{arcpeaks}} \tag{6-1}$$

A revised estimate of efficiency is Efficiency2 found from this formula

$$Efficiency2 = \frac{E_{plume}}{E_{arcpeaks} + E_{coilmag}} \tag{6-2}$$

It includes the effect of the magnetic energy of the magnetic field coil. Another revised estimate of efficiency is Efficiency3 found from this formula

$$Efficiency3 = \frac{E_{plume}}{E_{arcpeaks} + E_{coiltotalmagres}} \tag{6-3}$$

It includes the effects of both the magnetic energy and the resistive energy of the magnetic field coil. These efficiencies are plotted as functions of the magnetic field coil voltage in Figures 6-1, 6-2, and 6-3.

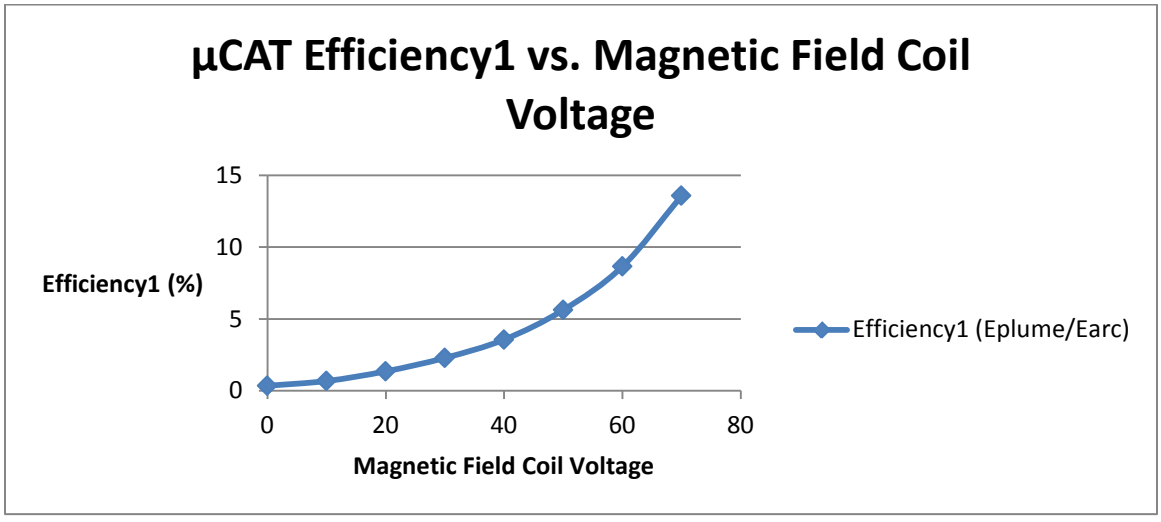

Figure 6-1: μCAT Efficiency1 vs. Magnetic Field Coil Voltage

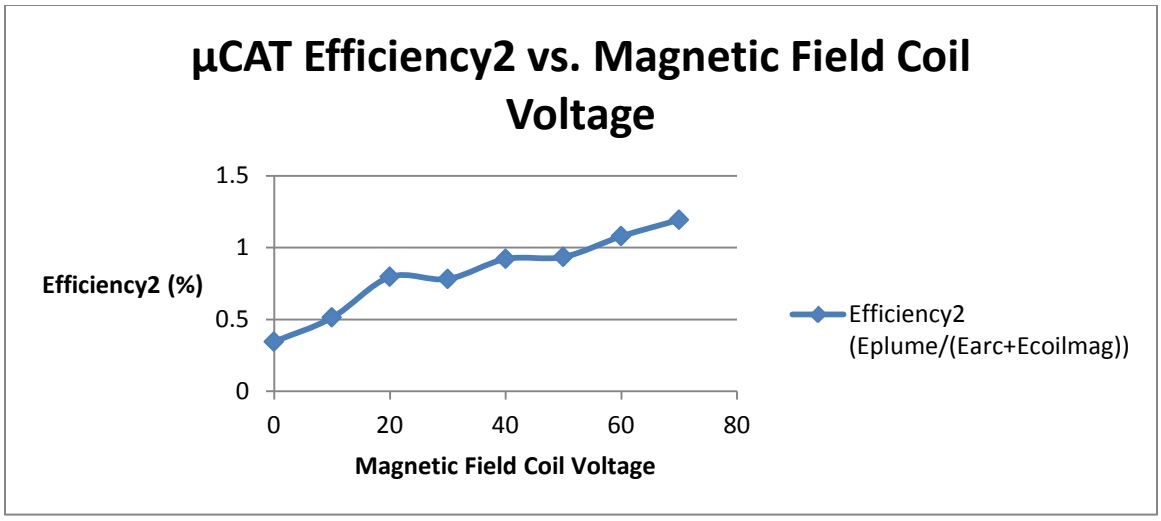

Figure 6-2: μCAT Efficiency2 vs. Magnetic Field Coil Voltage

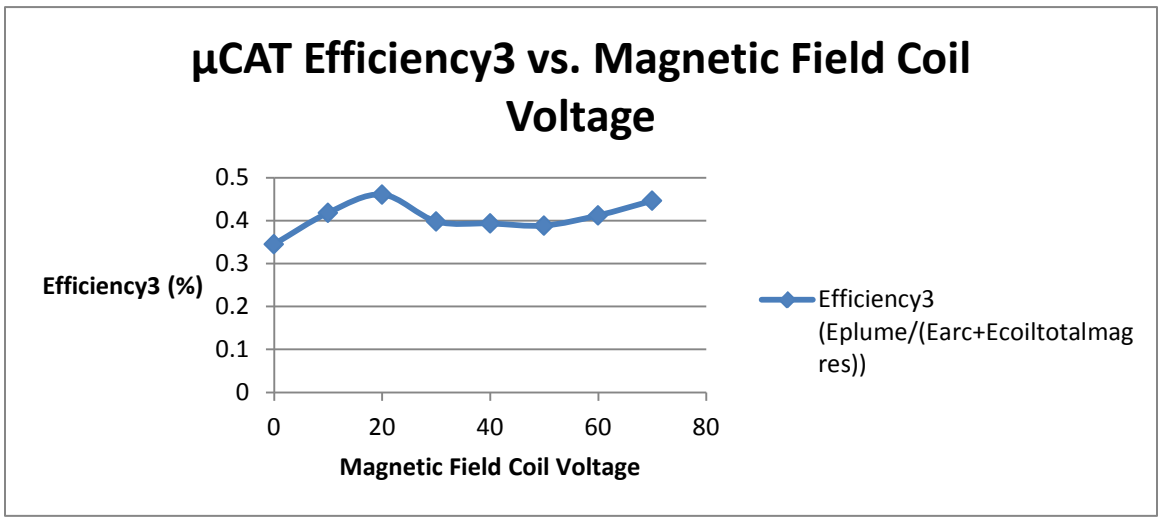

Figure 6-3: μCAT Efficiency3 vs. Magnetic Field Coil Voltage

While Efficiency1 and Efficiency2 both show increasing upward trends with the magnetic field coil voltage, Efficiency3 is more nearly level. In addition, the efficiency is less by an order of magnitude when the energy used in the magnetic field coil is accounted for. An overlay of all three efficiencies is shown in Figure 6-4.

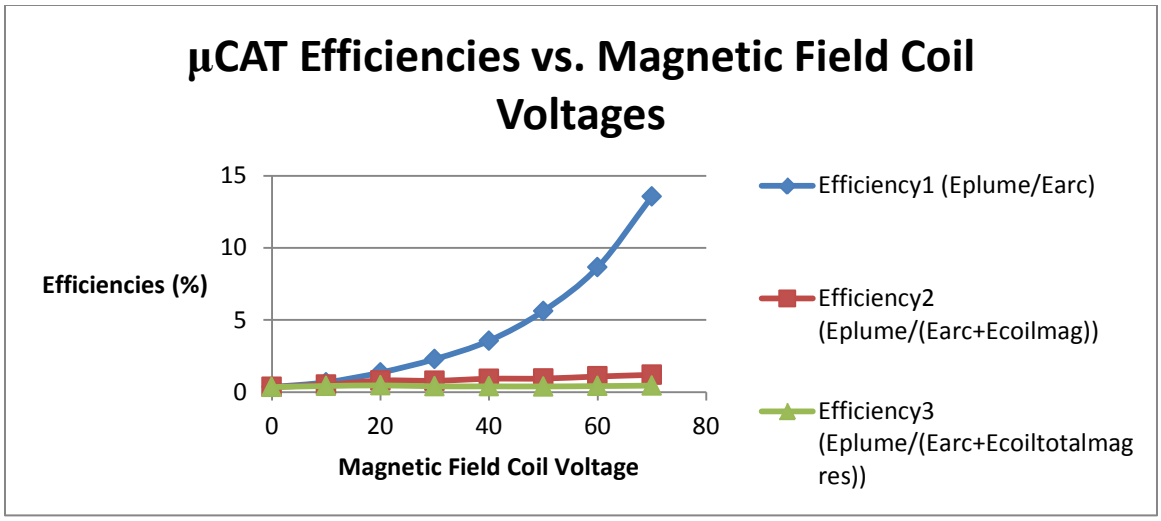

Figure 6-4: μ CAT Efficiencies vs. Magnetic Field Coil Voltage

The effect on efficiency of using a magnetic field coil is easily seen. Basic efficiency improves with an increased magnetic field coil voltage, but accounting for energy used in the coil drops it back down so it appears nearly level.

Improvements in efficiency might be made by minimizing energy spent in the magnetic field coil. The resistance of the wiring should be as low as possible and consideration might be given to lower currents. These factors would help to minimize the I^2R losses. A formula for the magnetic field strength at the center of a solenoid coil was provided in reference 15 as

$$B = \mu_0 nI \tag{6-4}$$

where μ_0 is the permeability of free space, n is the number of coil turns per unit length, and I is the electrical current. While I could be reduced to minimize the I^2R losses, the lower current would then reduce the field strength. A higher number of coil turns per unit length, however, could be a good strategy to increase B. An adequate field strength might then be achieved with less current. In addition, further improvements might be

obtained by minimizing the time it takes to reach the final coil current level. The important aspect of the magnetic field coil is to produce the necessary magnetic field strength. Achieving the field strength with minimum energy input is the goal.

Besides using a magnetic field coil, a permanent magnet might provide an appropriate magnetic field without requiring any electrical energy input. Such a situation would correspond to the Efficiency1 case. The input energy would be in the electrical arc and not both the arc and the coil. Permanent magnets have been considered further.

Chapter 7 – Magnetic Field Simulations

The design of the μCAT included a solenoid coil to produce the magnetic field. In order to improve the curvature of the field and achieve a better exhaust flow direction, metal plates were added around the circumference of the μCAT. The placement of the plates was such that the magnetic field was turned to intersect the cathode surface in a more perpendicular direction. In this way, the exhaust plume was expected to eject from the spot, follow the magnetic field lines to turn in the direction of the μCAT axis, and then exit from the thruster in a direction nearly perpendicular to the exhaust plane. The metal plates added significant mass and bulk. In addition, the solenoid coil and circuitry added mass and complexity and required energy to operate. In order to achieve a suitable magnetic field shape in a simpler fashion, various configurations of permanent magnets have been considered. The idea is to place permanent magnets around the μCAT structure to produce an appropriately curved magnetic field for a 90 degree turn of the exhaust plume.

A software application called Finite Element Method Magnetics (FEMM) Version 4.2 was used to simulate the magnetic field resulting from the existing magnetic field coil and metal plates and from several configurations of permanent magnets. The purpose was to provide a qualitative view of the magnetic field lines that exist or could be produced in the μCAT. AlNiCo was chosen as a typical permanent magnet material. For convenience, air was chosen as the surrounding medium. The FEMM software had the capability to produce two dimensional planar and axisymmetric views of the magnetic field lines. The output from the FEMM program for various permanent magnet configurations are shown in Appendix D. Axisymmetric and planar views are shown.

The axisymmetric views show just one half of the geometry. The axisymmetric model actually covers a full 360 degrees about the centerline. The planar views show a two dimensional arrangement of two separate magnets. They were modeled to be symmetric about the centerline axis. In this way, the model geometries of one cylindrical axisymmetric magnet and two magnets placed opposite each other were very similar. A review of the output views in Appendix D shows that the magnetic field results of each axisymmetric case and the corresponding planar case are also very similar.

As a baseline, the magnetic field simulation output for the current μCAT with the magnetic field coil and metal plates is shown in Figure 7-1.

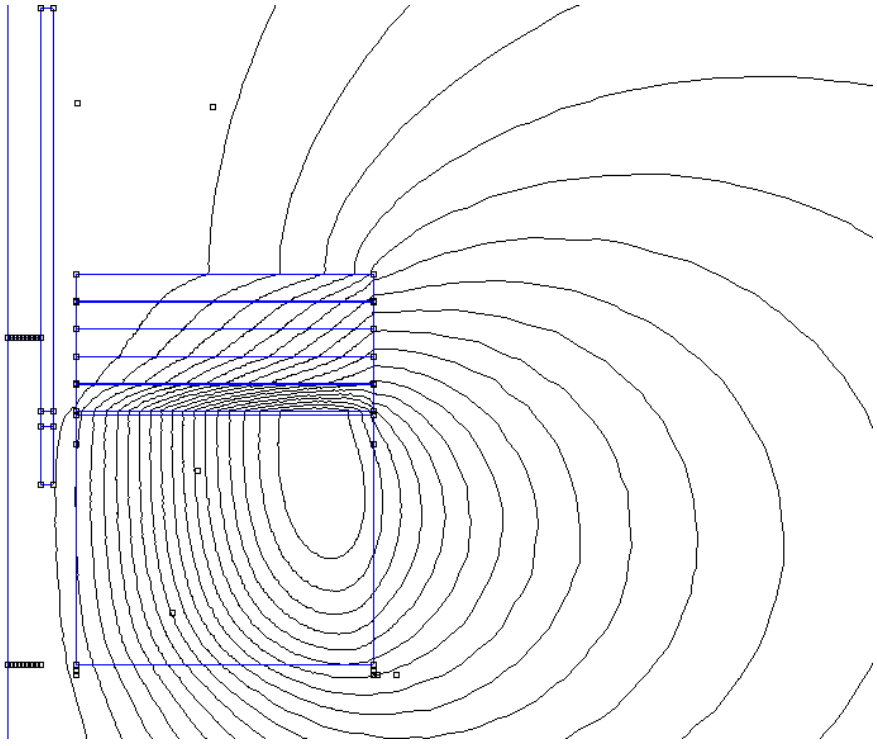

Figure 7-1: Magnetic Field Simulation, μCAT With Magnetic Field Coil and Metal Plates

The thruster centerline is on the left. The long titanium cathode (above) and the shorter titanium anode (below) appear just to the right of the thruster centerline. An insulator is between them. The 18 AWG magnetic field coil and the metal (1020 Steel) plates are positioned further to the right. A vacuum and the insulator were both approximated in the model as air. The cathode spot would occur near the lower inside corner of the cathode near the interface with the insulator. Although the software output shows a limited number of field lines, it is apparent that the lines that would intersect the cathode spot would do so at a nearly 45 degree angle and then proceed out of the thruster almost parallel to the centerline. The experimental results discussed previously showed the effectiveness of this arrangement.

The use of permanent magnets instead of the solenoid field coil and metal plates has been simulated for a number of cases. One simple configuration would be to place two magnets symmetrically on either side of the μCAT. The FEMM output for this two dimensional planar arrangement is shown in Figure 7-2.

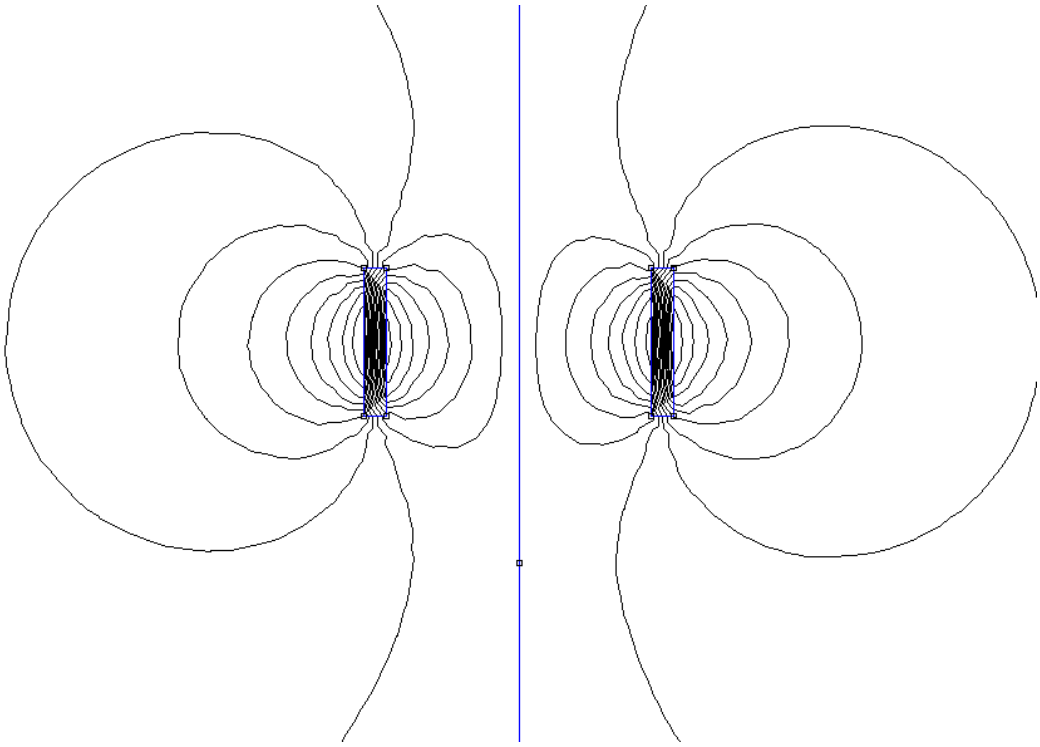

Figure 7-2: Magnetic Field Simulation, PlanarMagnet1.ans (Larger Area)

The centerline of the μCAT would be on the centerline of the figure. The magnets are seen on each side. They would be placed around the outside of the cylindrical cathode and anode. The magnetic field lines are also visible. The best curved shape of the field lines appears to be from the inside corners. At some angle, the field lines would proceed out of the magnets and approach the centerline. The magnets could be positioned with the inside corners near the end of the cathode. Part of the cathode, the insulator, and the anode would be beyond the end of the magnets. The cathode spot still occurs near the interface between the cathode and the insulator. With this placement, the magnetic field lines would intersect the cathode spot at an approximately 45 degree angle. The charged particles in the cathode spot plume would tend to follow the magnetic field lines and exit the thruster along the centerline. The effect would be comparable to the baseline

arrangement with the magnetic field coil and metal plates. If the magnets were placed with the cathode and insulator interface inside, the field lines could intersect the cathode spot in a perpendicular direction, but the plume might then easily be trapped inside between the magnet corners. If the magnets were placed with the cathode and insulator interface too far outside, the plume might diverge excessively outside the thruster, or even be directed back on the outside to the opposite ends of the magnets. The corresponding axisymmetric view is shown in Figure 7-3. This model geometry has one ring shaped magnet concentrically located about the μCAT centerline. Obviously, specific placement of the magnet with respect to the cathode spot location is very critical.

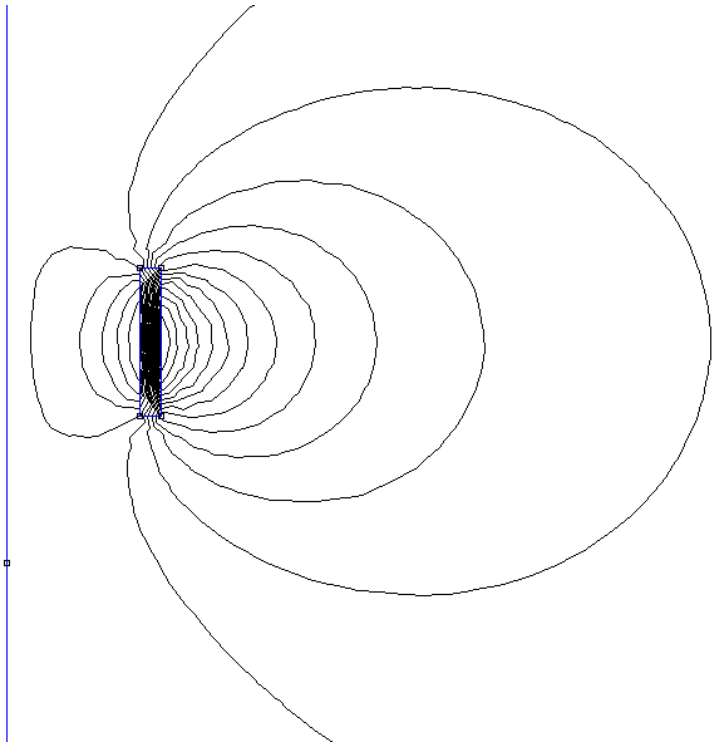

Figure 7-3: Magnetic Field Simulation, AxialMagnet1.ans (Larger Area)

Another simple configuration would be to orient the magnet to be perpendicular to the μCAT axis instead of parallel to it. The planar view of this configuration is shown in Figure 7-4.

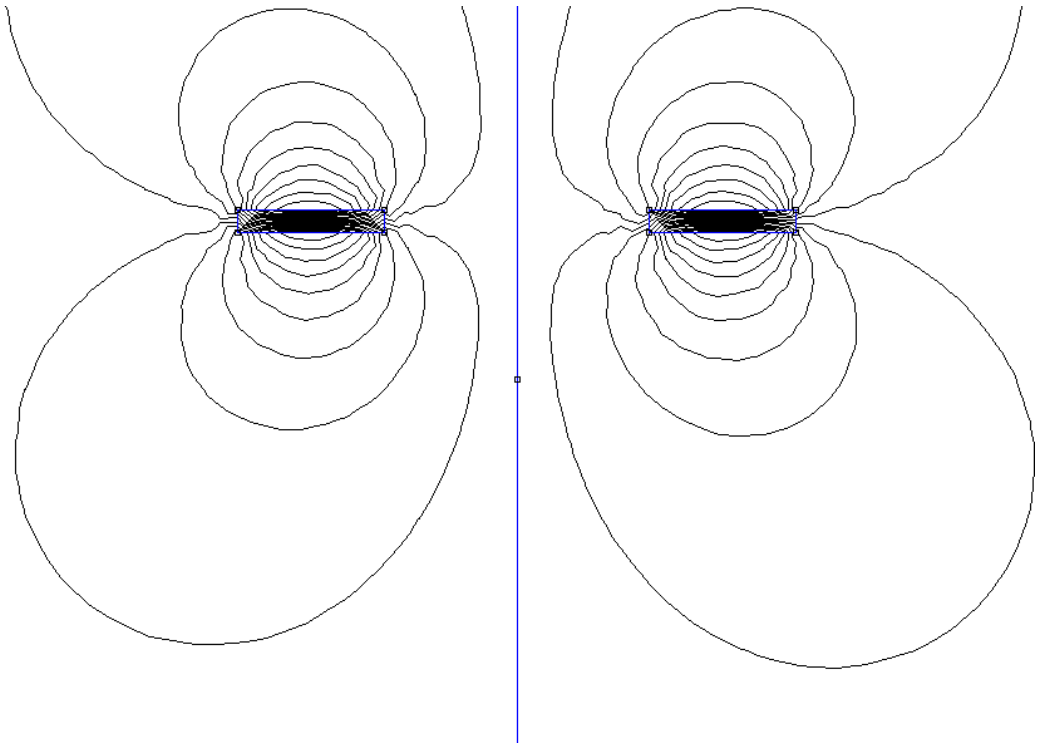

Figure 7-4: Magnetic Field Simulation, PlanarMagnet1Rotated.ans

It can be seen that the magnetic field lines proceeding from the inside end of the magnet that approach the centerline could intersect the cathode spot in a more nearly perpendicular fashion. This situation might offer some improvement over the configuration with the magnetic field lines intersecting the cathode spot at a 45 degree angle.

Some configurations were modeled that utilized several magnets. One obvious configuration would be to place multiple magnets concentric to the μCAT centerline and at the same distance from that centerline. Such a configuration is shown in Figure 7-5.

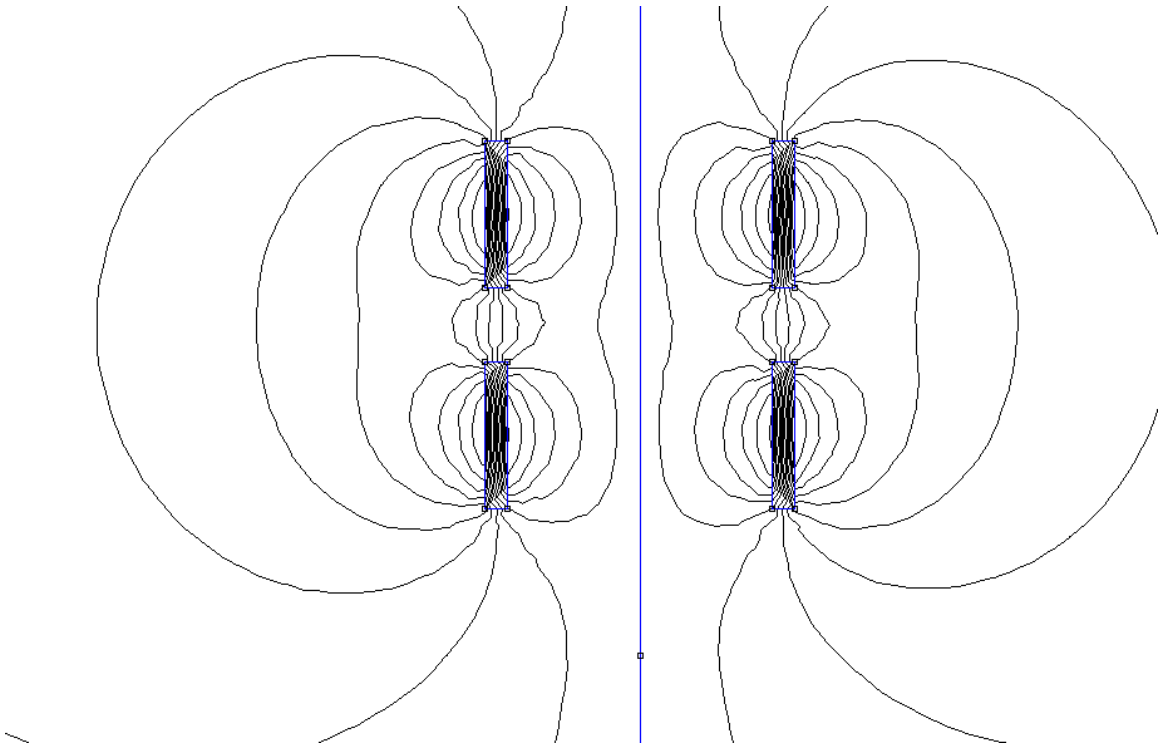

Figure 7-5: Magnetic Field Simulation, PlanarMagnet2NonExpanded.ans

While some of the magnetic field lines are nearly parallel to the centerline of the μCAT, they turn back to the inner corners of the magnets. A plasma plume along these lines would probably impact some of the μCAT structure or the magnets themselves. Most of the field lines in the interior region proceed back to some corner of the magnets. The best placement of the magnets with respect to the μCAT again seems to be with the cathode spot near the inside corner at the outer end.

Another configuration with multiple magnets is shown in Figure 7-6. In this case, the 45 degree angle position is an attempt to create a nozzle like effect with the field lines.

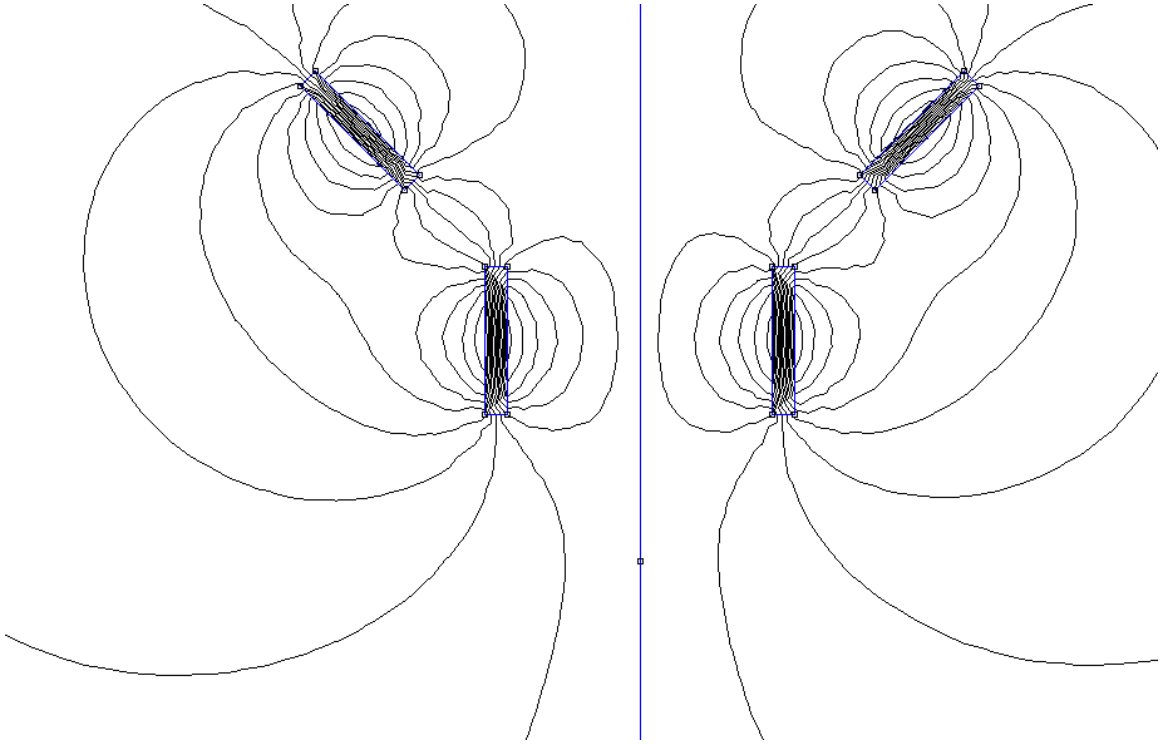

Figure 7-6: Magnetic Field Simulation, PlanarMagnet2_45Angle.ans

With multiple magnets, however, multiple corner effects still occur. A plasma plume in the interior region would again be misdirected away from the μCAT centerline. Corner effects tend to produce field lines that are perpendicular to the desired direction of travel for the plasma plume. While the configuration of Figure 7-6 might work, the cathode spot would still have to be located near the inside corner at the lower end. There is no particular advantage to this multiple magnet placement.

A specially shaped magnet in the form of a quarter circle was also considered. The configuration is shown in Figure 7-7. This shape is another attempt to create a nozzle like effect.

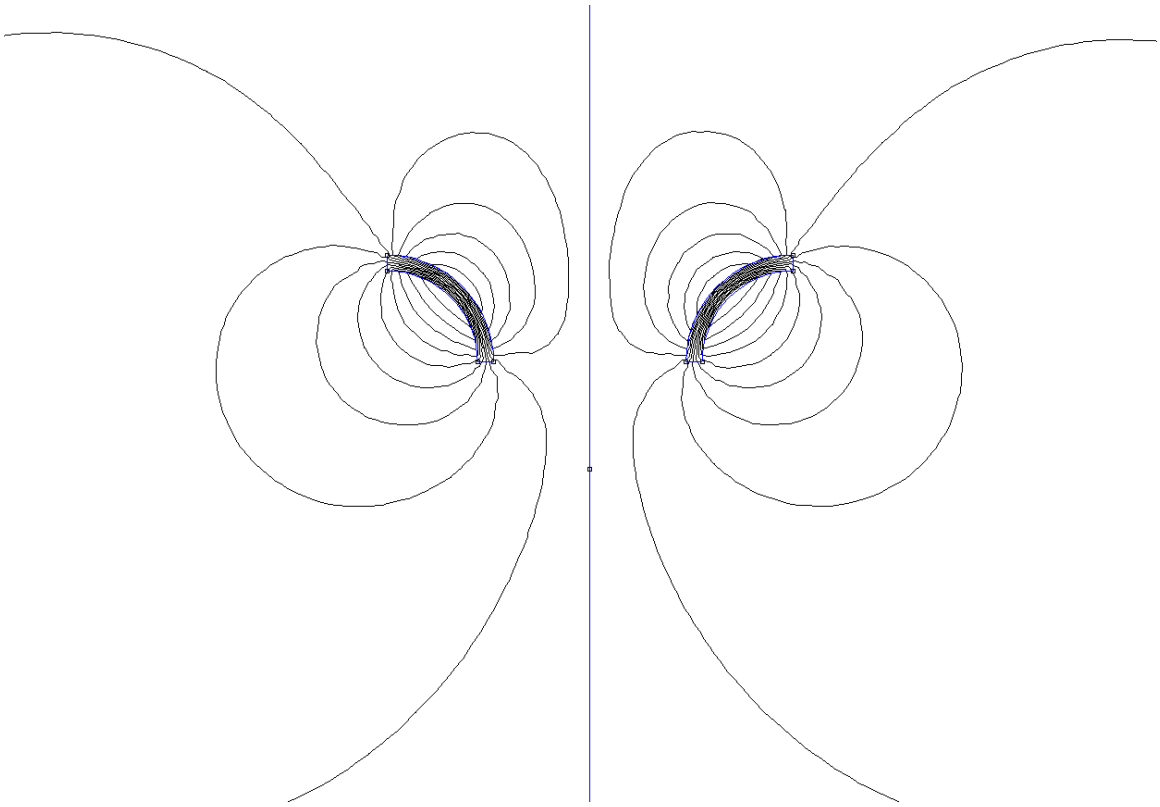

Figure 7-7: Magnetic Field Simulation, PlanarMagnet1QuarterCircle.ans

The magnetic field lines at the inside bottom corner that approach the centerline could again intersect the cathode spot in a nearly perpendicular fashion. The inside area, however, still does not create an effective nozzle. The cathode spot should be positioned close to the inside bottom edge.

Another attempt to avoid corner effects involved the use of round magnets. A configuration with multiple round magnets is shown in Figure 7-8.

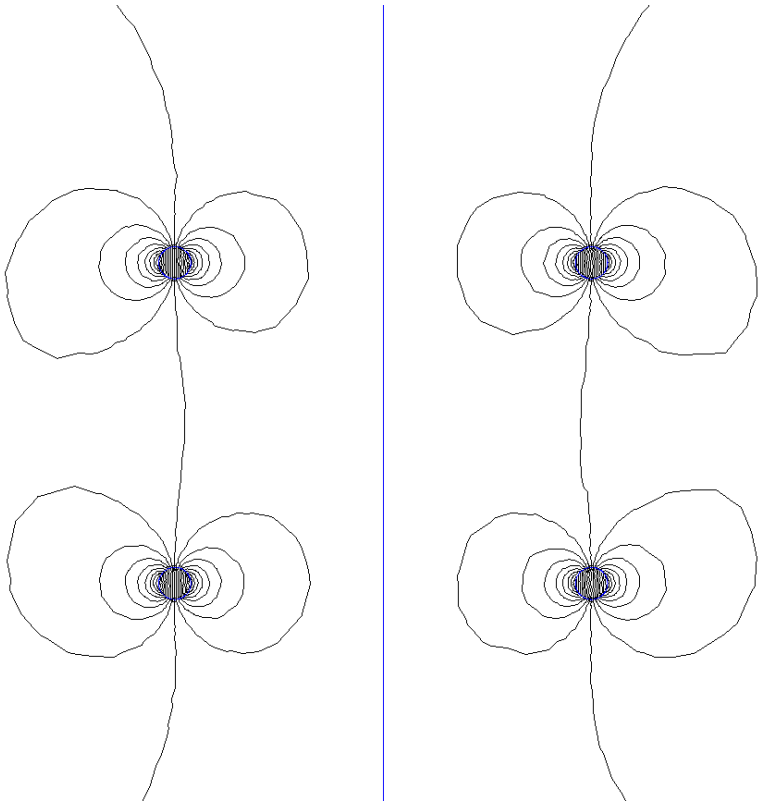

Figure 7-8: Magnetic Field Simulation, PlanarMagnet2Circular.ans

The magnetic field lines between the magnets either circle back to the opposite side or proceed into the other magnet. Although specific corners are eliminated, the problem of corner effects is still present. In order for this configuration to be effective, the cathode spot would have to be positioned in the outside region. It can also be seen that the magnetic field lines that approach the centerline would not be perpendicular to the cathode spot.

Another configuration for a μCAT was considered that used a central anode surrounded by a concentric insulator and then a concentric cathode. The electrodes were placed inside a cylindrical casing. The electrodes were modeled as titanium. The

insulator and vacuum regions were modeled as air for convenience. The casing was modeled with both non-magnetic and magnetic materials. Aluminum was the non-magnetic material and axisymmetric magnetic field simulation results for this case are shown in Figure 7-9.

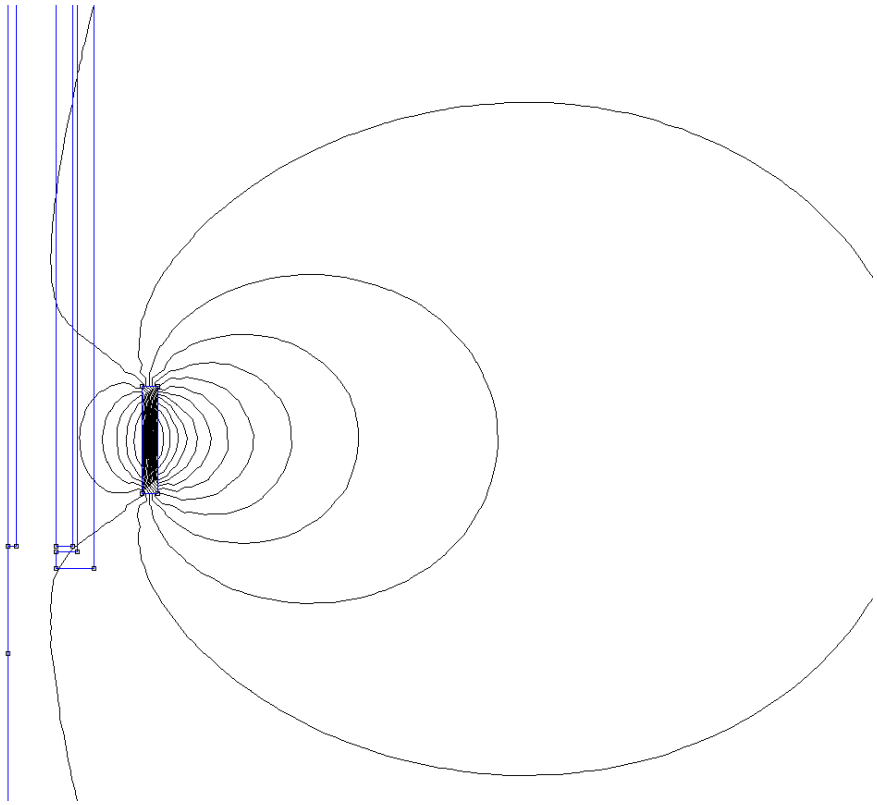

Figure 7-9: Magnetic Field Simulation, μ CAT2_NonMagCasing.ans

Half the anode is shown along the centerline. The empty space could be an insulator. The cathode and casing then appear close together. A permanent magnet is positioned on the outside. The cathode spot would be created at the bottom inside corner of the cathode. The magnet creates magnetic field lines that pass through the cathode spot,

approach the centerline, and then proceed outside the thruster. The plasma plume would tend to follow the magnetic field lines and be turned to the exhaust direction.

The same configuration was modeled but with a magnetic material for the casing. Steel was the magnetic material and axisymmetric magnetic field simulation results for this case are shown in Figure 7-10.

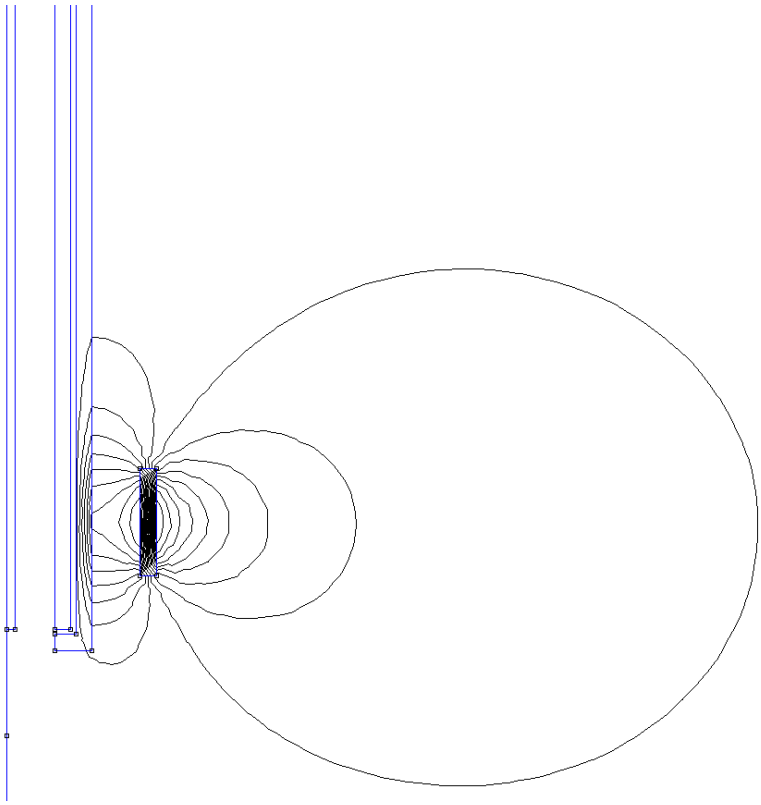

Figure 7-10: Magnetic Field Simulation, μ CAT2_MagCasing.ans

It is clearly seen that the use of the steel magnetic material for the casing blocks the magnetic field lines from reaching the cathode spot area. No plasma plume turning benefit would be obtained in this case.

The most advantageous arrangement seems to come from a single permanent magnet, similar to that shown in Figure 7-4, that is perpendicular to the thruster axis. A quarter circle shape similar to that in Figure 7-7 is another possibility but has a slightly increased complexity. In addition, the use of ferro-magnetic materials in the thruster structure might cause problems since they could distort, or even block, the desired magnetic field.

Chapter 8 – Plasma Parameters

The successful operation of the μCAT is based on the assumption that the ablated material emanating from the cathode spot is in the form of plasma. The magnetic field then turns the charged particles in the direction of the exhaust. A check on this assumption can be made by calculating the Debye Length, λ_D, for the environment of the μCAT with a titanium arc. The equation for the Debye Length is listed in reference 16 as

$$\lambda_D = \left(\frac{\epsilon_0 * K * T_e}{n * e^2}\right)^{\frac{1}{2}} \tag{8-1}$$

The permittivity of free space, ϵ_0, is taken as 8.85×10^{-12} C^2/Nm^2. K is Boltzmann's constant with a value of 1.381×10^{-23} J/K. T_e is the electron temperature and is assumed to be 2 eV for a titanium arc. The conversion factor is then 11,600 K per 1 eV. The number density, n, for the arc is assumed to be 1×10^{20} particles/m^3. The electronic charge, e, has a value of 1.602×10^{-19} C. The Debye Length for the GWU μCAT is then 1.051×10^{-6} m. The μCAT inner diameter is 0.218 inches, or 0.00554 m. Since the Debye Length is several orders of magnitude less than a characteristic dimension of the μCAT, $\lambda_D << L$, the cathode spot material would be expected to behave as a plasma within the geometric region of the μCAT hardware.

The Larmor radii for the ions and electrons, r_{Li} and r_{Le}, respectively, should be considered in order to evaluate the turning of the charged particles in the μCAT's externally applied magnetic field. The mass of a titanium ion and an electron will be needed. The atomic mass of titanium will be taken as 47.90 g/gmole. The mass of an atom is found from

$$\frac{mass}{atom} = \frac{atomic\ mass}{Avogadros's\ number} \tag{8-2}$$

Then for a titanium atom,

$$\frac{mass}{titanium\ atom} = \frac{47.90\ g/gmole}{6.022x10^{23}\ atoms/gmole} * \frac{1\ kg}{1000\ g} \tag{8-3}$$

So for one titanium atom,

$$\frac{mass}{titanium\ atom} = 7.954x10^{-26}kg \tag{8-4}$$

An electron mass is $9.1095x10^{-31}$ kg. Titanium ions in an electric arc will be assumed to be doubly charged. The ionicity is 2.0. As a result, the mass of a titanium ion missing two electrons is nearly the same as for a titanium atom.

The Larmor radius for a titanium ion in the μCAT is then found from the following formula in reference 16 as

$$r_{Li} = \frac{mV_{perpendicular}}{qB} \tag{8-5}$$

where m is the mass of the particle, $V_{perpendicular}$ is the velocity component of the particle perpendicular to the magnetic field lines, q is the electric charge of the particle, and B is the strength of the magnetic field. A doubly charged titanium ion will have a charge of

$$q_{Tion} = 2(1.602x10^{-19}C) = 3.204x10^{-19}C \tag{8-6}$$

The experimentally determined particle speeds and the magnetic field strengths varied. Therefore, a number of different Larmor radii values exist for the μCAT. Speeds of 0 to 70,000 m/sec and magnetic fields of 0 to 0.3 Tesla will be considered. The resulting Larmor radii in meters for titanium ions are shown in Table 8-1.

r_{Li} (m)	B (Tesla)	0	0.05	0.10	0.15	0.20	0.25	0.30
$V_{perpendicular}$ (m/sec)								
10000		Inf	0.0497	0.0248	0.0166	0.0124	0.00993	0.00828
20000		Inf	0.0993	0.0497	0.0331	0.0248	0.0199	0.0166
30000		Inf	0.149	0.0745	0.0497	0.0372	0.0298	0.0248
40000		Inf	0.199	0.0993	0.0662	0.0497	0.0397	0.0331
50000		Inf	0.248	0.124	0.0828	0.0621	0.0497	0.0414
60000		Inf	0.298	0.149	0.0993	0.0745	0.0596	0.0497
70000		Inf	0.348	0.174	0.116	0.0869	0.0695	0.0579

Table 8-1: Ion Larmor Radii for Different Particle Speeds and Magnetic Field Strengths

The smallest Larmor radius for an ion is 0.00828 m when the speed is 10,000 m/sec in a 0.3 Tesla magnetic field. The higher speeds and lower B fields have even larger Larmor radii. The μCAT inner diameter of 0.00554 m is somewhat smaller. Therefore, the ions are not expected to be magnetized within the confines of the μCAT chamber. The magnetic field would need to be around 0.45 Tesla for the ions to be magnetized at the 10,000 m/sec speed.

The Larmor radius for electrons in the μCAT also varies with the speed and magnetic field strength. Even though the charge on one electron is half that of the doubly charged titanium ion, the electron mass is five orders of magnitude smaller than the ion mass. The largest Larmor radius for the electrons is 0.00000796 m when the speed is

70,000 m/sec in a 0.05 Tesla magnetic field. Therefore, the electrons are expected to be magnetized within the μCAT chamber for all conditions. Electrons would be constrained to follow the magnetic field lines. The magnetic field strength would have to be as low as around 0.00001 Tesla for the electrons not to be magnetized within the 0.00554 m inner diameter of the μCAT at the 10,000 m/sec speed, or 0.00007 Tesla at the 70,000 m/sec speed.

Since the ions might not be magnetized in the μCAT, other mechanisms must be at work to cause the plasma plume to turn in the direction of the thruster axis. The forces acting on the ions include that from the magnetic field and also electrostatic forces from the anode and cathode and from the electrons themselves. The magnitude of these forces on an ion can be determined and compared.

The magnetic force on a charged particle can be found from the formula listed in reference 15 as

$$\vec{F}_{mag} = q\vec{V}x\vec{B} \tag{8-7}$$

where q is the charge of the particle, $\vec{V}$ is the particle velocity, and $\vec{B}$ is the magnetic field strength. The various combinations of particle speeds and $\vec{B}$ fields result in different values of the magnetic force on one ion. Again, speeds of 0 to 70,000 m/sec and magnetic fields of 0 to 0.3 Tesla will be considered. The velocities will be considered to be perpendicular to the magnetic field resulting in the maximum values for the magnetic forces for each pair of conditions. These force values in Newtons for titanium ions are shown in Table 8-2.

F_{mag_ion} (N)	B (T)	0	0.05	0.10	0.15	0.20	0.25	0.30
V_{per} (m/sec)								
0		0	0	0	0	0	0	0
10000		0	1.60E-16	3.20E-16	4.81E-16	6.41E-16	8.01E-16	9.61E-16
20000		0	3.20E-16	6.41E-16	9.61E-16	1.28E-15	1.60E-15	1.92E-15
30000		0	4.81E-16	9.61E-16	1.44E-15	1.92E-15	2.40E-15	2.88E-15
40000		0	6.41E-16	1.28E-15	1.92E-15	2.56E-15	3.20E-15	3.84E-15
50000		0	8.01E-16	1.60E-15	2.40E-15	3.20E-15	4.01E-15	4.81E-15
60000		0	9.61E-16	1.92E-15	2.88E-15	3.84E-15	4.81E-15	5.77E-15
70000		0	1.12E-15	2.24E-15	3.36E-15	4.49E-15	5.61E-15	6.73E-15

Table 8-2: Ion Magnetic Forces for Different Ion Speeds and Magnetic Field Strengths

Besides the obvious zero cases, the magnetic forces on a doubly charged ion range from 1.60E-16 to 6.73E-15 N.

The potential across the anode and cathode results in an electric field and an electrostatic force on the charged particles. This electrostatic force can be found from a formula in reference 15 as

$$\vec{F}_{el} = q\vec{E} \tag{8-8}$$

where again, q is the charge on the particle and $\vec{E}$ is the electric field. The electric field can be found from

$$\vec{E} = \frac{potential}{distance} \tag{8-9}$$

The arc voltage values found previously in Table 5-4 and shown in Figure 5-4 can be used for the potential between the anode and cathode. These voltage values varied depending on the magnetic field strength. The minimum distance between the anode and cathode was approximately 0.04 inches, or 0.001 m. The electric field strength varies throughout the μCAT but will have a maximum value near the 0.001 m insulator between the anode and cathode. The electrostatic force values on a doubly charged titanium ion with the various electric field, potential, and magnetic field coil voltages are shown in Table 8-3.

Magnetic Field Coil Voltage (volts)	Potential (volts)	Electric Field (volts/m)	Electrostatic Force (N)
0	61.86738999	61867.38999	1.98E-14
10	58.76923077	58769.23077	1.88E-14
11.2	61.19804457	61198.04457	1.96E-14
19.6	78.19974119	78199.74119	2.51E-14
20	79.00934579	79009.34579	2.53E-14
30	89.61534247	89615.34247	2.87E-14
30.8	89.76530059	89765.30059	2.88E-14
40	91.489819	91489.819	2.93E-14
42	92.91715322	92917.15322	2.98E-14
50	98.62649007	98626.49007	3.16E-14
56	102.6936995	102693.6995	3.29E-14

60	105.4051724	105405.1724	3.38E-14
61	107.8277066	107827.7066	3.45E-14
70	129.6305147	129630.5147	4.15E-14

Table 8-3: Electrostatic Forces on a Doubly Charged Titanium Ion

The electrostatic forces are seen to range from 1.98E-14 to 4.15E-14 N. The electrostatic forces on the ions would be different in areas of the μCAT further away from the anode-cathode interface.

Electrostatic forces also exist between the positive ions and negative electrons in the titanium plasma. The electrons are initially attracted to the anode closer to the exit plane of the μCAT. The magnetized electrons may experience some constraint by the magnetic field and display a tendency to remain in the vicinity of the anode and exhaust. Assuming the titanium ions are doubly charged, two free electrons should exist for each ion. The electrostatic force between one ion and two closely located electrons can be found from Coulomb's Law. The formula as listed in reference 15 is

$$\vec{F}_{12} = \frac{1}{4\pi\epsilon_0}\frac{q_1 q_2}{r_{12}^2}\hat{r}_{12} \tag{8-10}$$

$\vec{F}_{12}$ is the electrostatic force between an ion and a pair of electrons. Here, the electrons are treated as one particle. In the quasi-neutral plasma, it would be expected to encounter two electrons for every doubly charged ion. The permittivity of free space, ϵ_0, has a value of $8.85\text{x}10^{-12}$ C^2/Nm^2. The electric charges for an ion and a pair of electrons are q_1 and q_2. The separation distance between the ion and the pair of electrons is r_{12}. The proximity of the electrons to each other is an assumption for calculation purposes. The pair of electrons represents one particle to associate with one positive ion. Normally, the

negative electrons would be expected to repel each other. The direction of the electrostatic force is given by the unit vector, $\hat{r}_{12}$, between the ion and the general location of the pair of electrons. The magnitude of the electrostatic force is of interest. The appropriate values can be used in Coulomb's Law for a sample 0.001 m separation distance.

$$F_{12} = \frac{1}{4\pi\left(8.85x10^{-12}\frac{C^2}{Nm^2}\right)}\frac{[2(1.602x10^{-19}C)][2(-1.602x10^{-19}C)]}{(0.001m)^2} \quad (8\text{-}11)$$

Then

$$F_{12} = -9.23x10^{-22}N \quad (8\text{-}12)$$

The negative sign indicates an attraction. The force varies inversely with the square of the distance between the particles. Values of the magnitude of this force for separation distances of 0.001 to 0.010 m are shown in Table 8-4.

Separation Distance (m)	Magnitude of Electrostatic Force Between Particles (N)
0	Infinite
0.001	9.23064E-22
0.002	2.30766E-22
0.003	1.02563E-22
0.004	5.76915E-23
0.005	3.69226E-23
0.006	2.56407E-23
0.007	1.8838E-23

0.008	1.44229E-23
0.009	1.13959E-23
0.010	9.23064E-24

Table 8-4: Magnitude of Electrostatic Force Between Particles for Different Separation Distances

A plot of these forces vs. separation distance is shown in Figure 8-1.

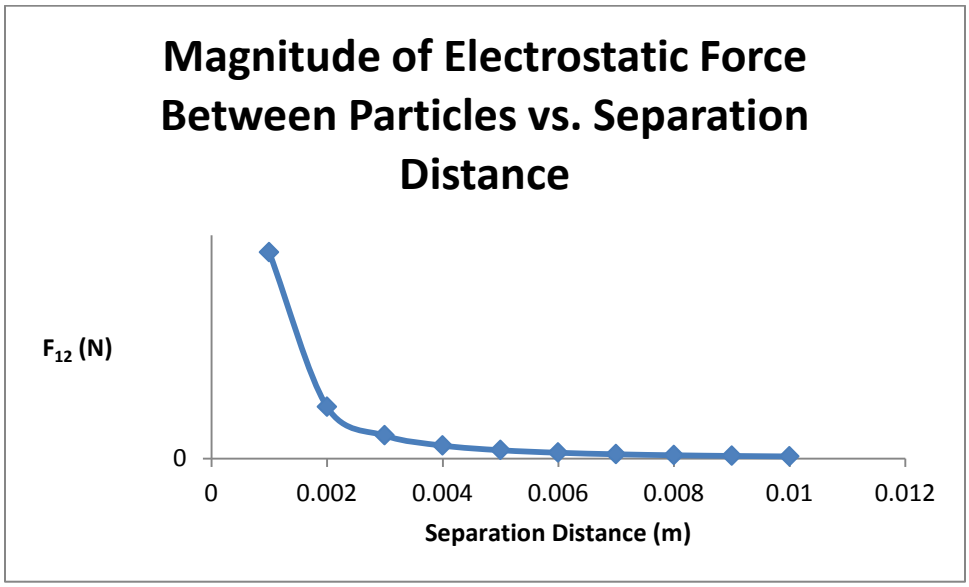

Figure 8-1: Magnitude of Electrostatic Force Between Particles vs. Separation Distance

The electrostatic force between the charged particles could equal the larger value of 4.15E-14 N for the electrostatic force due to the anode and cathode if the particle separation distance were reduced to 1.49×10^{-7} m. This distance is an order of magnitude less than the Debye Length of 1.051×10^{-6} m. The electrostatic force between the particles could equal the smaller 1.98E-14 N for the electrostatic force due to the anode and cathode if the separation distance were 2.16×10^{-7} m.

The electrostatic forces due to the anode and cathode seem to have the highest magnitude. The magnetic forces due to the motion of the charged particles are one to two

orders of magnitude smaller. The electrostatic forces between pairs of individual particles are much less except for particle separation distances an order of magnitude less than the Debye Length.

Chapter 9 – μCAT Application

The μCAT provides a very low thrust. It does have the potential to deliver this thrust for an extended period of time. There are a number of applications for such a device. One possible application that can be considered is an orbit change for a satellite. Specifically, a change from a circular Low Earth Orbit (LEO) to an elliptical orbit with a lower perigee can be analyzed.

A one kg satellite will be assumed to start in a 500 km altitude circular orbit around the Earth. The satellite can be maneuvered by changing the circular orbit to an elliptical one with a perigee at a lower altitude of 300 km. The μCAT thrust would produce changes to the satellite on a long time scale. As an approximation for calculation, however, it will be assumed that the thrust results in an instantaneous velocity change, ΔV, to change the circular orbit to an elliptical one. The ΔV change occurs just at the apogee of the new elliptical orbit. The perigee of the new elliptical orbit will be assumed to be at the lower altitude of 300 km.

The semi-major axis, a, of the elliptical orbit can be found from

$$2a = r_a + r_p \tag{9-1}$$

where r_a is the apogee distance and r_p is the perigee distance. The equation can be rewritten as

$$2a = (r_e + h_a) + (r_e + h_p) \tag{9-2}$$

where r_e is the 6378 km radius of the Earth, h_a is the apogee altitude of 500 km, and h_p is the perigee altitude of 300 km. Then

$$2a = (6378\ km + 500\ km) + (6378\ km + 300\ km) \tag{9-3}$$

and

$$a = 6778\ km \tag{9-4}$$

The energy law, or vis-viva equation, provides an expression for determining the spacecraft velocity, V, of a satellite in an elliptical orbit as shown in references 17 and 18,

$$\frac{V^2}{2} - \frac{\mu}{r} = -\frac{\mu}{2a} \tag{9-5}$$

or as shown in reference 19,

$$V = \sqrt{\mu\left(\frac{2}{r} - \frac{1}{a}\right)} \tag{9-6}$$

The Earth is at one focus of the elliptical orbit and r is the distance from the center of the Earth to the satellite. The value of the gravitational parameter, μ, for the Earth is 3.986012×10^5 km^3/sec^2. Then at the apogee of the elliptical orbit

$$V_a = \sqrt{\left(3.986012x10^5\ \frac{km^3}{sec^2}\right)\left(\frac{2}{6378\ km + 500\ km} - \frac{1}{6778\ km}\right)} \tag{9-7}$$

and

$$V_a = 7.5563\ \frac{km}{sec} \tag{9-8}$$

The velocity of the satellite in the starting circular orbit with a radius equal to the apogee distance of the elliptical orbit can be found from

$$V_{circular} = \sqrt{\frac{\mu}{r}} \tag{9-9}$$

as shown in reference 20.

Then

$$V_{circular} = \sqrt{\frac{3.986012x10^5 \frac{km^3}{sec^2}}{6378\ km + 500\ km}} \tag{9-10}$$

and

$$V_{circular} = 7.6127\ \frac{km}{sec} \tag{9-11}$$

The ΔV that is needed to change from the circular orbit to the elliptical one is then

$$\Delta V = V_{circular} - V_a \tag{9-12}$$

and

$$\Delta V = 0.0564\ \frac{\text{km}}{\text{sec}} \tag{9-13}$$

The new elliptical orbit might then be used as the starting point for additional maneuvers.

The rocket equation from reference 20 can then be used to determine the mass of titanium electrode propellant needed to produce this ΔV.

$$\Delta V = c \ln \frac{M_0}{M_f} \tag{9-14}$$

The exhaust velocity is c and the final satellite mass, M_f, was assumed to be 1 kg. M_0 is the initial mass of the satellite. M_p is the propellant mass.

$$M_0 = M_f + M_p \tag{9-15}$$

The rocket equation can also be written as

$$\frac{M_0}{M_f} = e^{\frac{\Delta V}{c}} \tag{9-16}$$

And substituting gives

$$\frac{M_f + M_p}{M_f} = e^{\frac{\Delta V}{c}} \tag{9-17}$$

or

$$M_p = M_f * e^{\frac{\Delta V}{c}} - M_f \tag{9-18}$$

The experimental μCAT exhaust velocities varied considerably. Representative values could be from 20,000 to 50,000 m/sec (20 to 50 km/sec). Using the low end value gives

$$M_p = 1\ kg * e^{\frac{0.0564\frac{km}{sec}}{20\frac{km}{sec}}} - 1\ kg \tag{9-19}$$

Then

$$M_p = 0.00282\ kg \tag{9-20}$$

The orbit change maneuver could be accomplished for the 1 kg satellite with approximately 2.82 gm of the titanium electrode propellant.

An estimate of the time needed to consume 2.82 gm of the propellant can be made by using a representative value for the mass consumption rate in the μCAT. This rate varies depending on the magnetic field coil strength. A value of $2x10^{-5}$ mg/pulse is in the middle of the range. Then

$$2x10^{-5}\frac{mg}{pulse} * \frac{1\ gm}{1000\ mg} * number\ of\ pulses = 2.82\ gm \tag{9-21}$$

and

$$number\ of\ pulses = 1.41x10^{8} \tag{9-22}$$

At a thruster operational frequency of 10 pulses/sec, $1.41x10^{7}$ sec, or 3,917 hours would be needed. The orbit change maneuver could be accomplished in a little over 163 days. This time might be decreased by changing the frequency or current to the thruster. The thruster duty cycle could be customized to suit the specific mission being executed.

The amount of propellant needed for the orbit change maneuver for various exhaust velocities is shown in Table 9-1.

Exhaust Speed (km/sec)	Propellant Mass (kg)
0	Infinite
5	0.011343859
10	0.005655935
15	0.003767078
20	0.00282398
25	0.002258547
30	0.001881768
35	0.001612728
40	0.001410995
45	0.001254119
50	0.001128636
55	0.001025981
60	0.000940442
65	0.000868069
70	0.000806039

Table 9-1: Propellant Mass for Orbit Change Maneuver for a 1 kg Satellite vs. Exhaust Speed

These values are plotted in Figure 9-1.

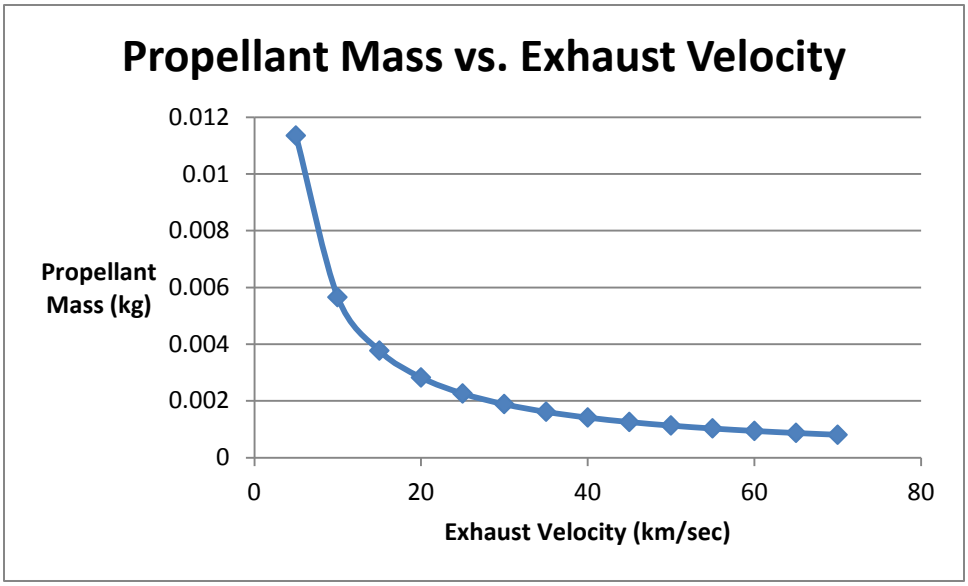

Figure 9-1: Propellant Mass for Orbit Change Maneuver for a 1 kg Satellite vs. Exhaust Velocity

Increasing the exhaust velocity eventually produces a more limited benefit in terms of the mass of propellant needed to perform the maneuver. The elbow of the curve around 20 km/sec may be a reasonable choice to consider for an operating point. This value for the exhaust velocity was found to occur at the low end of the magnetic field strengths applied to the μCAT. It should be remembered, however, that lower magnetic field strengths may not be as effective in turning the plasma plume in the correct exhaust direction. While adequate exhaust velocities may occur at low field strengths, the amount of the propellant that actually gets expelled may be smaller.

Conclusions

The most significant conclusion from the effort with the GWU μCAT was that the externally applied magnetic field is effective at increasing the performance of the thruster. Especially as seen in Figure 5-1, the exhaust plume kinetic energy seems to increase exponentially with the magnetic field coil voltage. Realistically, it would be expected that the charged particles in the plasma plume would eventually be fully turned to the exhaust direction and no further benefit from increased magnetic field strengths would be obtained. There may be a leveling off effect at some point. In contrast, the electrical energy in the vacuum arc exhibited a tendency to decrease with the magnetic field coil voltage. In addition, the arc pulse duration also tended to decrease with the magnetic field coil voltage while the arc voltage showed a strong increasing tendency. The magnitude of the μCAT pulses often had a significant variation from pulse to pulse as seen in some of the figures in Appendix C. The frequency of the pulses, however, was very consistent. The energy expended in the magnetic field coil obviously increased with the coil voltage. The components of this energy in the magnetic field and in the resistive coil losses were comparable, but the resistive part was dominant.

Different efficiency values were determined. All were based on a ratio of the mechanical plume output energy to different electrical input energies. Efficiency1 was based on the plume energy and the electric arc energy. It showed an exponential increase to over 13% with increasing magnetic field coil voltage. When the energies expended in the magnetic field coil were taken into account, Efficiency2 still showed an increasing trend while Efficiency3 was more nearly level and both were around or below 1%, a full order of magnitude less than Efficiency1. These efficiencies could be improved by

minimizing the resistance of the magnetic field coil and by increasing the number of coil turns per unit length. Also, less coil energy would be consumed by minimizing the time used to reach the final coil current level. Although the current in the coil could be decreased to reduce the resistive losses, the lower current would also reduce the magnetic field strength.

The magnetic field simulations for different permanent magnet configurations indicated that the placement of the magnets with respect to the cathode spot location is critical to optimum operation of the μCAT. A radially oriented ring magnet similar to the configuration in Figure 7-3 might be the best since the magnetic field lines could be made to intersect the cathode spot in a nearly perpendicular direction before turning approximately 90 degrees to the exhaust direction. It was found that using multiple magnets would lead to undesirable corner effects on the magnetic field lines. In such cases, the plasma plume would probably be misdirected and impact the μCAT structure itself rather than be properly exhausted out of the unit. It was also seen that the use of a ferromagnetic material in a casing around the electrodes would block the magnetic field lines and destroy the plasma turning benefit of the external magnetic field.

The evaluation of the cathode jet properties showed that the material is a plasma since the Debye Length is significantly less than characteristic dimensions of the μCAT. An evaluation of properties also showed that the titanium ions are not magnetized while the electrons are. Calculations of various forces in the μCAT showed that the electrostatic forces on the charged particles from the anode and cathode could be larger than the magnetic field forces on those particles. Also, the electrostatic forces between the charged particles themselves could be the largest if the particle separation distances

were an order of magnitude less than the Debye Length. Finally, a sample calculation for a possible orbit change maneuver from a 500 km circular orbit to a 500 km apogee, 300 km perigee elliptical orbit showed that a propellant mass of a few grams would be adequate for a one kg satellite. The propellant mass needed for larger satellites could be scaled up accordingly. The time required to accomplish the maneuver would be on the order of five or six months.

References

1. Taisen Zhuang, Alexey Shashurin, Thomas Denz, David Chichka, and Michael Keidar, "Micro-Vacuum Arc Thruster with Extended Lifetime", 45th AIAA/ASME/SAE/ASEE Joint Propulsion Conference & Exhibit, Denver, Colorado, 2-5 August 2009, AIAA Paper No. AIAA 2009-4820.

2. Patrick Vail, Anthony Pancotti, Taisen Zhuang, Alexey Shashurin, Thomas Denz, and Michael Keidar, "Performance Characterization of Micro-Cathode Arc Thruster (μCAT)", 47th AIAA/ASME/SAE/ASEE Joint Propulsion Conference & Exhibit, San Diego, California, 31 July - 03 August 2011, AIAA Paper No. AIAA 2011-5883.

3. A.A.Plyutto, V.N. Ryzhdov, and A.T. Kapin, "High Speed Plasma Streams in Vacuum Arcs", Soviet Physics JETP (J. Exptl. Theoret. Phys.), Volume 20, Number 2, pages 328-337, February 1965.

4. A.S. Gilmour, Jr., "Concerning the Feasibility of a Vacuum Arc Thrustor", AIAA Fifth Electric Propulsion Conference, San Diego, California, March 7-9, 1966, AIAA Paper No. 66-202.

5. A.S. Gilmour, Jr., R.J. Clark, Jr., and H. Veron, "Pulsed Vacuum-Arc Microthrustors", AIAA Electric Propulsion and Plasmadynamics Conference, Colorado Springs, Colorado, September 11-13, 1967, AIAA Paper No. 67-737.

6. Rolf Dethlefsen, "Performance Measurements on a Pulsed Vacuum Arc Thruster", AIAA Journal, Volume 6, Number 6, Technical Notes, June 1968.

7. Alexander S. Gilmour, Jr. and David L. Lockwood, “Pulsed Metallic-Plasma Generators”, Proceedings of the IEEE, Volume 60, Number 8, August 1972.

8. A.M. Dorodnov, “Technical applications of plasma accelerators”, Sov. Phys. Tech. Phys., 23(9), September 1978.

9. Andre Anders, Robert A. MacGill, and Thomas A. McVeigh, “Efficient, compact power supply for repetitively pulsed, “triggerless” cathodic arcs”, Review of Scientific Instruments, Volume 70, Number 12, December 1999.

10. A. Anders, J. Schein, and N. Qi, “Pulsed vacuum-arc ion source operated with a “triggerless” arc initiation method”, Review of Scientific Instruments, Volume 71, Number 2, February 2000.

11. Niansheng Qi, Jochen Schein, Robert Binder, Mahadevan Krishnan, Andre Anders, and Jay Polk, “Compact Vacuum Arc Micro-Thruster for Small Satellite Systems”, AIAA-2001-3793, 2001.

12. Jochen Schein, Niansheng Qi, Robert Binder, Mahadevan Krishnan, John K. Ziemer, James E. Polk, and Andre Anders, “Low Mass Vacuum Arc Thruster System for Station Keeping Missions”, 27th International Electric Propulsion Conference, Pasadena, California, October 15-19, 2001, Paper No. IEPC-01-228.

13. J. Schein, N. Qi, R. Binder, M. Krishnan, J. K. Ziemer, J. E. Polk, and A. Anders, “Inductive energy storage driven vacuum arc thruster”, Review of Scientific Instruments, Volume 73, Number 2, February 2002.

14. James E. Polk, Michael J. Sekerak, John K. Ziemer, Jochen Schein, Niansheng Qi, and Andre Anders, "A Theoretical Analysis of Vacuum Arc Thruster and Vacuum Arc Ion Thruster Performance", IEEE Transactions on Plasma Science, Volume 36, Number 5, October 2008.

15. Paul A. Tipler, "Physics", Worth Publishers, Inc., New York, NY, 1976.

16. Francis F. Chen, "Introduction to Plasma Physics and Controlled Fusion", Second Edition, Volume 1: Plasma Physics, Springer Science+Business Media, LLC, New York, NY, 2006.

17. Howard D. Curtis, "Orbital Mechanics for Engineering Students", Elsevier Butterworth-Heinemann, Burlington, MA, 2005.

18. Bong Wie, "Space Vehicle Dynamics and Control", American Institute of Aeronautics and Astronautics, Inc., Reston, VA, 1998.

19. George P. Sutton, Oscar Biblarz, "Rocket Propulsion Elements", Seventh Edition, John Wiley & Sons, Inc., New York, NY, 2001.

20. Michael D. Griffin, James R. French, "Space Vehicle Design", Second Edition, American Institute of Aeronautics and Astronautics, Inc., Reston, VA, 2004.

Appendix A – μCAT Voltage vs. Time Curves for Various Magnetic Field Strengths

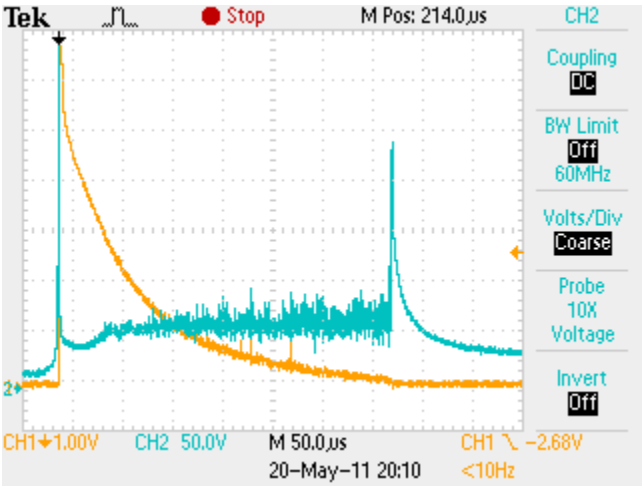

Figure A-1: μCAT Voltage vs. Time Curves for 0 Volt Magnetic Field

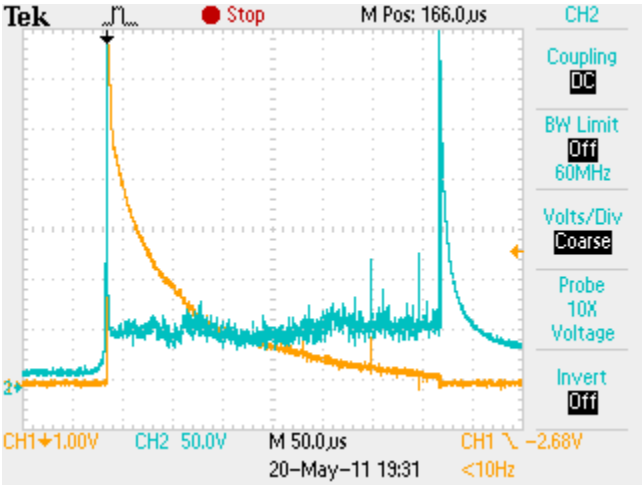

Figure A-2: μCAT Voltage vs. Time Curves for 10 Volt Magnetic Field

Appendix A – μCAT Voltage vs. Time Curves for Various Magnetic Field Strengths

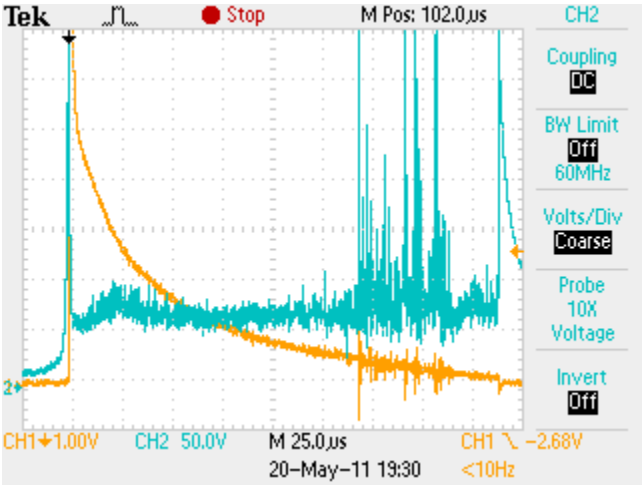

Figure A-3: μCAT Voltage vs. Time Curves for 20 Volt Magnetic Field

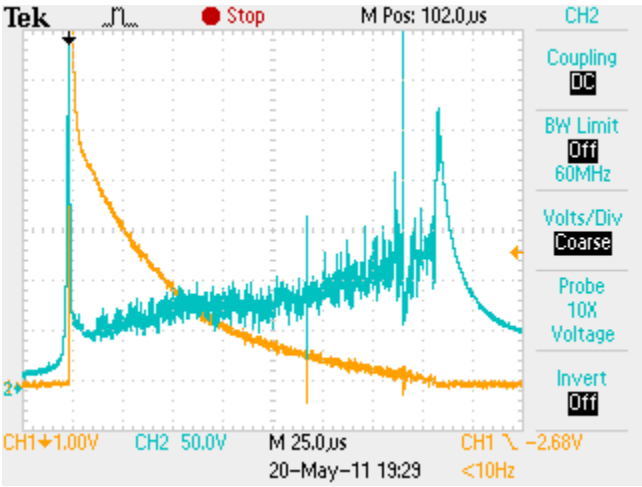

Figure A-4: μCAT Voltage vs. Time Curves for 30 Volt Magnetic Field

Appendix A – μCAT Voltage vs. Time Curves for Various Magnetic Field Strengths

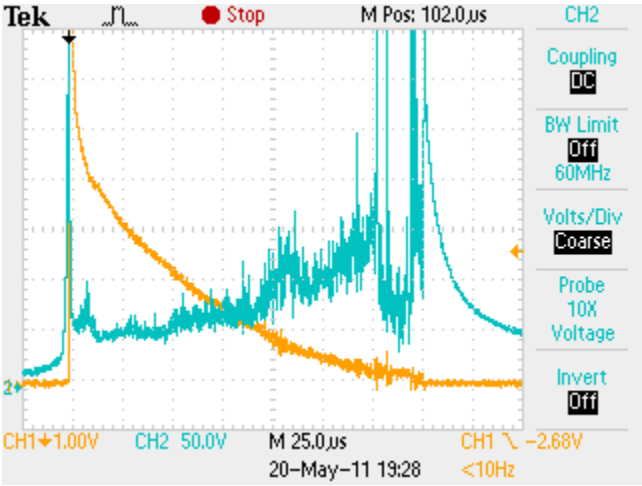

Figure A-5: μCAT Voltage vs. Time Curves for 40 Volt Magnetic Field

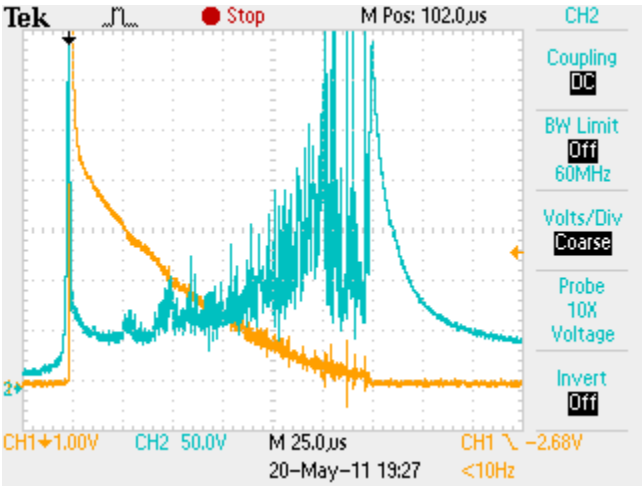

Figure A-6: μCAT Voltage vs. Time Curves for 50 Volt Magnetic Field

Appendix A – μCAT Voltage vs. Time Curves for Various Magnetic Field Strengths

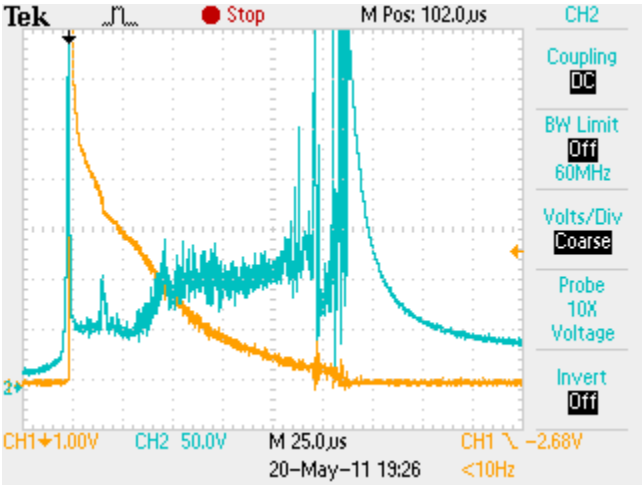

Figure A-7: μCAT Voltage vs. Time Curves for 60 Volt Magnetic Field

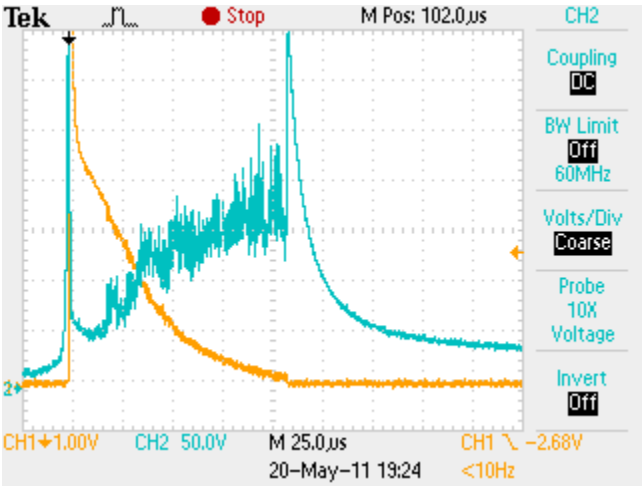

Figure A-8: μCAT Voltage vs. Time Curves for 70 Volt Magnetic Field

Appendix B – Magnetic Field Coil Signal vs. Time Curves for Various Magnetic Field Strengths

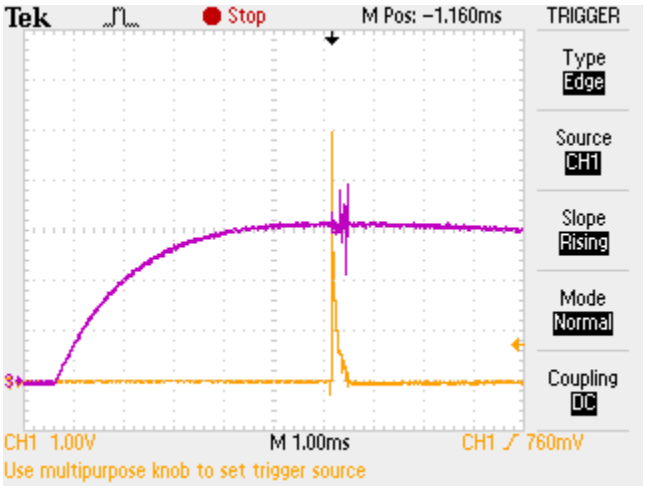

Figure B-1: Magnetic Field Coil Shunt Resistor Voltage vs. Time Curve for 10 Volt Magnetic Field

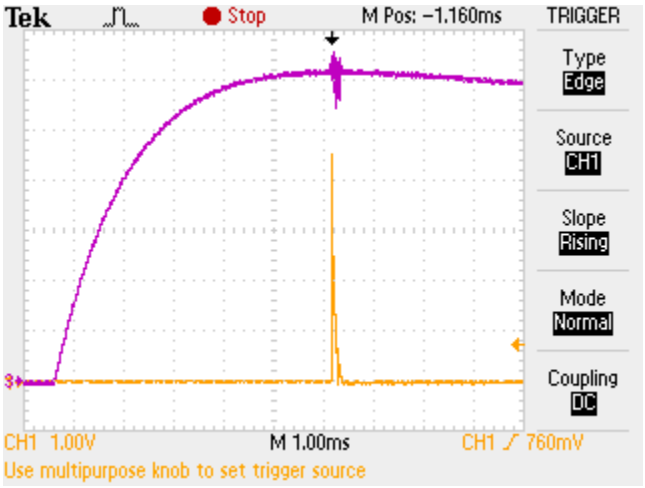

Figure B-2: Magnetic Field Coil Shunt Resistor Voltage vs. Time Curve for 20 Volt Magnetic Field

Appendix B – Magnetic Field Coil Signal vs. Time Curves for Various Magnetic Field Strengths

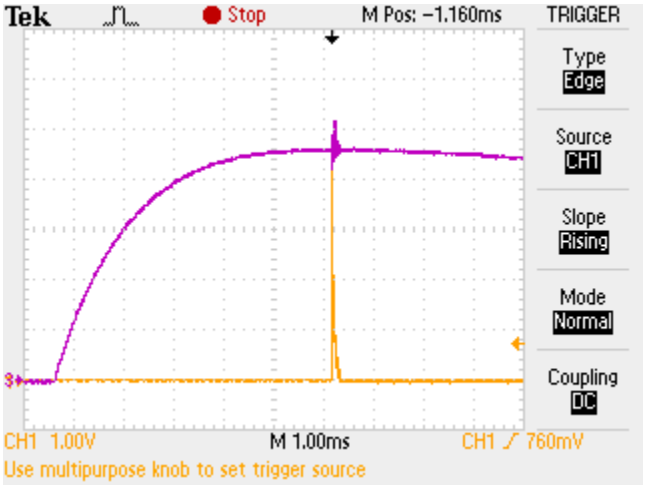

Figure B-3: Magnetic Field Coil Shunt Resistor Voltage vs. Time Curve for 30 Volt Magnetic Field

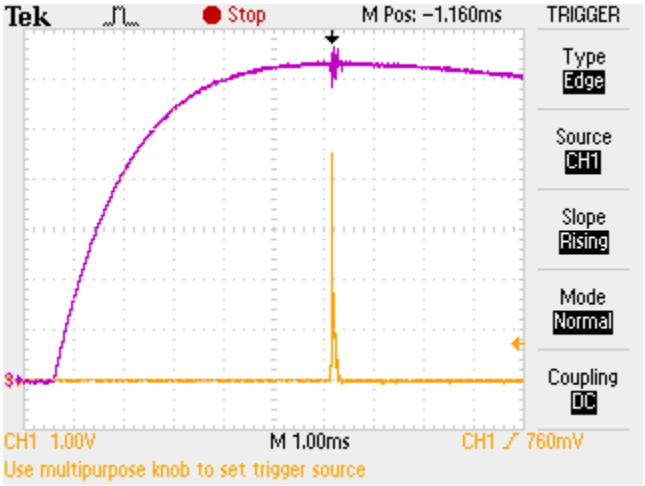

Figure B-4: Magnetic Field Coil Shunt Resistor Voltage vs. Time Curve for 40 Volt Magnetic Field

Appendix B – Magnetic Field Coil Signal vs. Time Curves for Various Magnetic Field Strengths

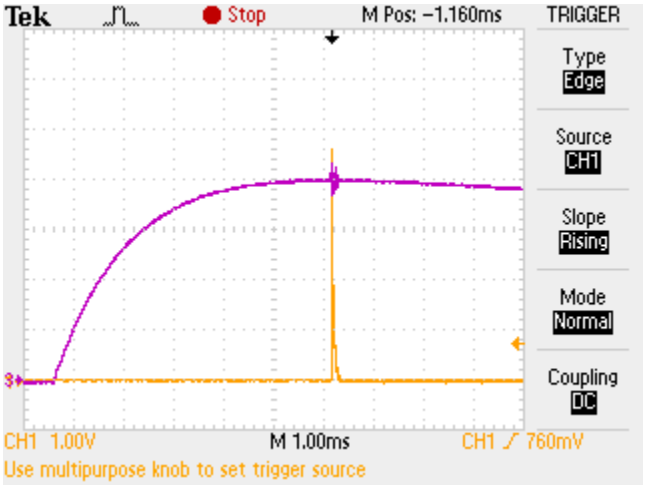

Figure B-5: Magnetic Field Coil Shunt Resistor Voltage vs. Time Curve for 50 Volt Magnetic Field

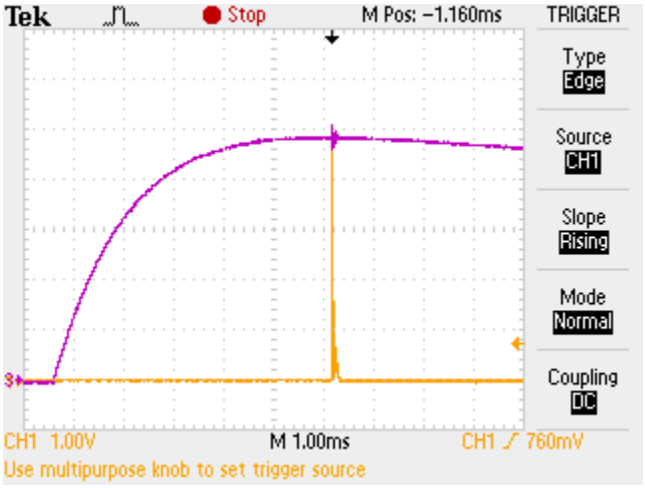

Figure B-6: Magnetic Field Coil Shunt Resistor Voltage vs. Time Curve for 60 Volt Magnetic Field

Appendix B – Magnetic Field Coil Signal vs. Time Curves for Various Magnetic Field Strengths

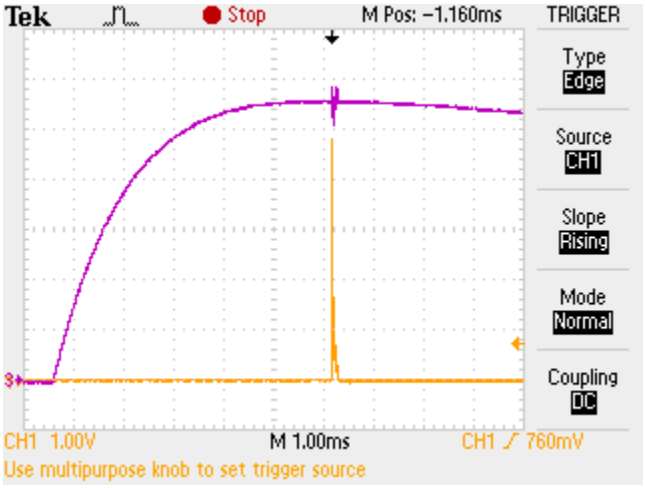

Figure B-7: Magnetic Field Coil Shunt Resistor Voltage vs. Time Curve for 70 Volt Magnetic Field

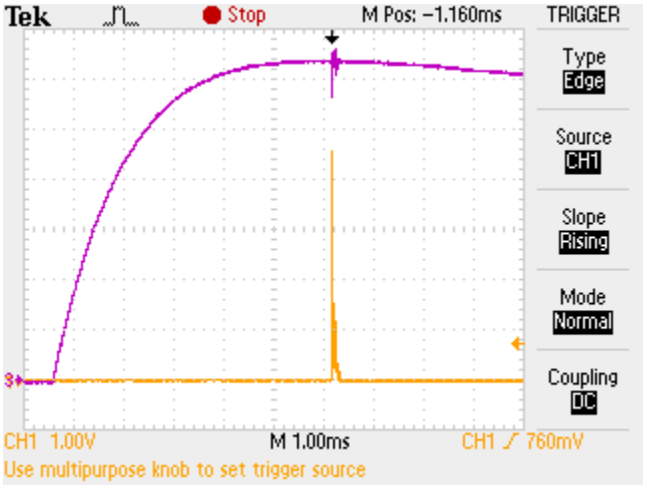

Figure B-8: Magnetic Field Coil Shunt Resistor Voltage vs. Time Curve for 80 Volt Magnetic Field

Appendix B – Magnetic Field Coil Signal vs. Time Curves for Various Magnetic Field Strengths

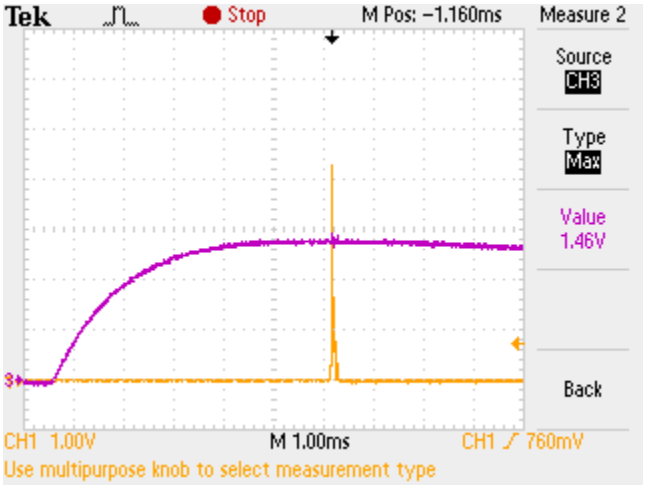

Figure B-9: Magnetic Field Coil Shunt Resistor Voltage vs. Time Curve for 90 Volt Magnetic Field

Appendix C – Arc Pulses vs. Time for Various Magnetic Field Strengths

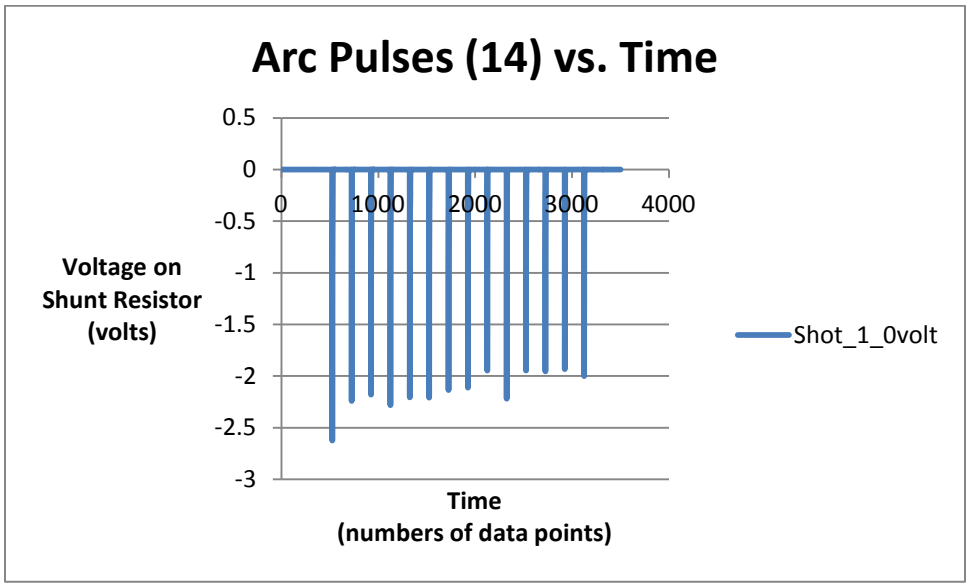

Figure C-1: Arc Pulses (14) vs. Time for Shot 1 at 0 Volts

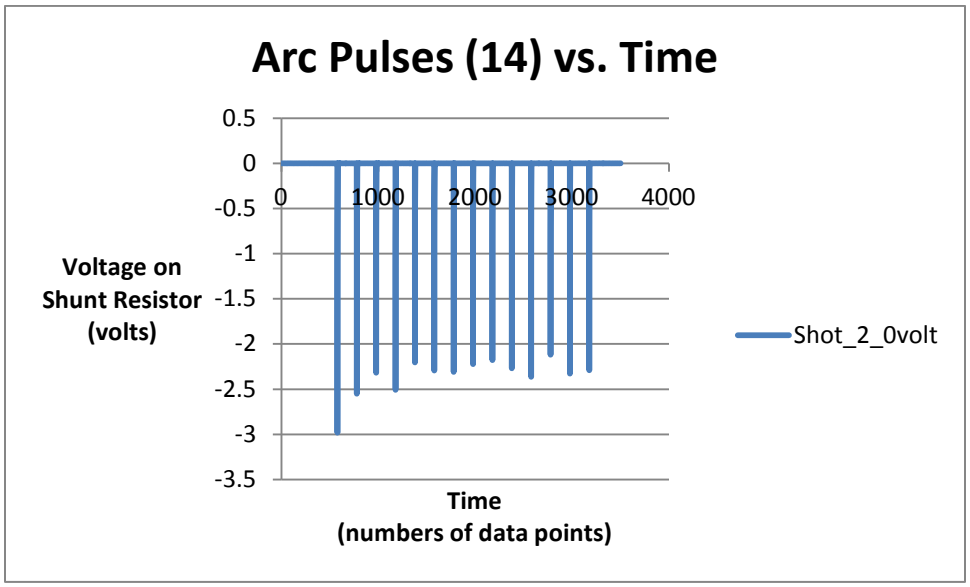

Figure C-2: Arc Pulses (14) vs. Time for Shot 2 at 0 Volts

Appendix C – Arc Pulses vs. Time for Various Magnetic Field Strengths

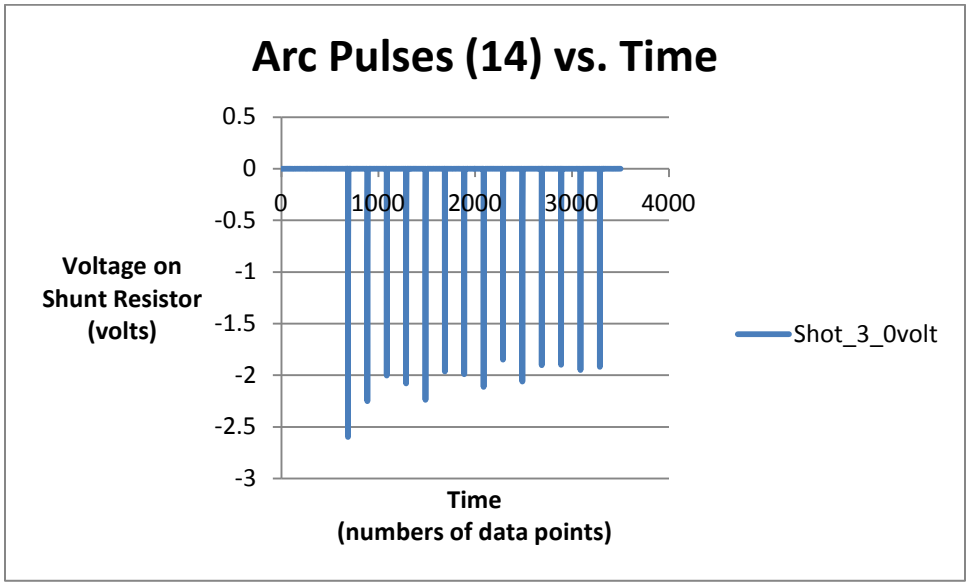

Figure C-3: Arc Pulses (14) vs. Time for Shot 3 at 0 Volts

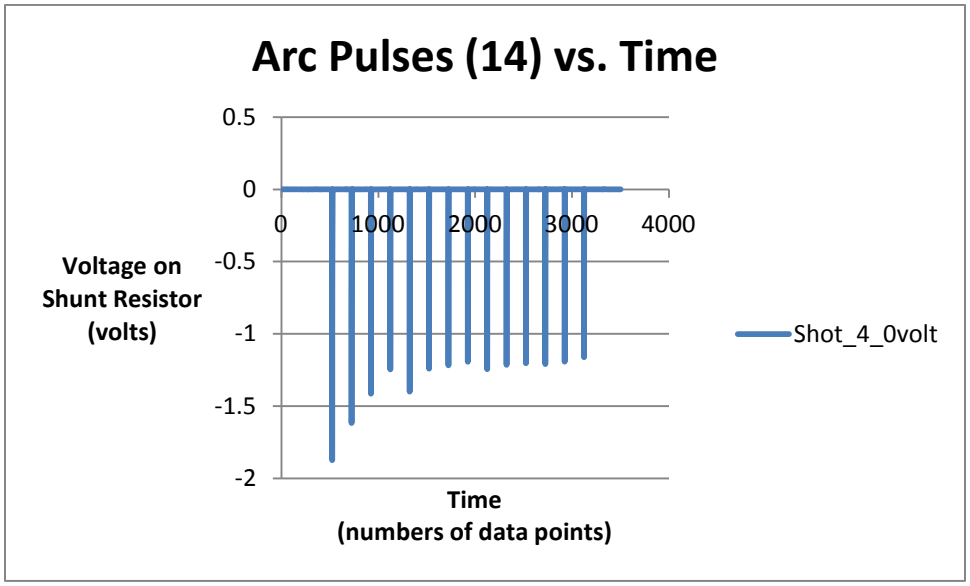

Figure C-4: Arc Pulses (14) vs. Time for Shot 4 at 0 Volts

Appendix C – Arc Pulses vs. Time for Various Magnetic Field Strengths

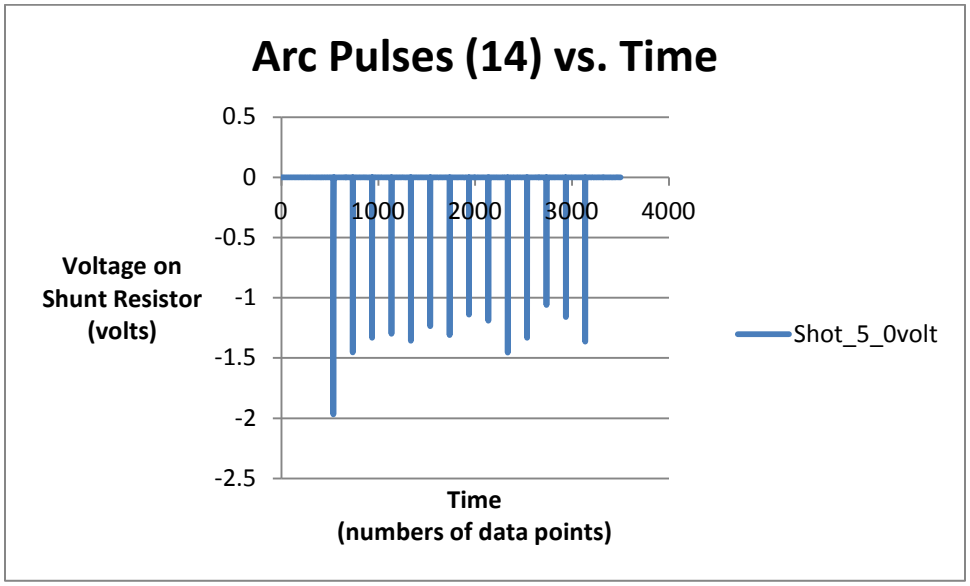

Figure C-5: Arc Pulses (14) vs. Time for Shot 5 at 0 Volts

Appendix C – Arc Pulses vs. Time for Various Magnetic Field Strengths

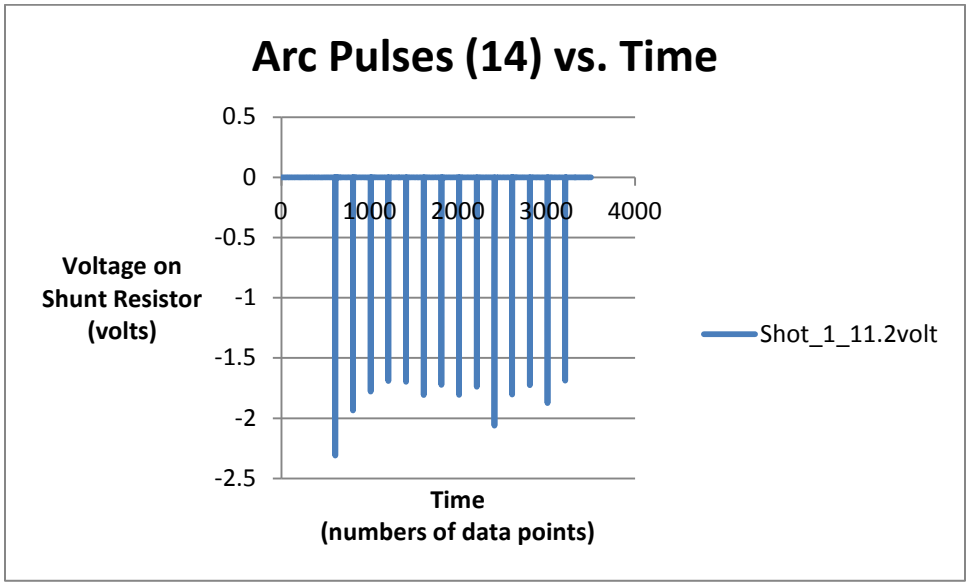

Figure C-6: Arc Pulses (14) vs. Time for Shot 1 at 11.2 Volts

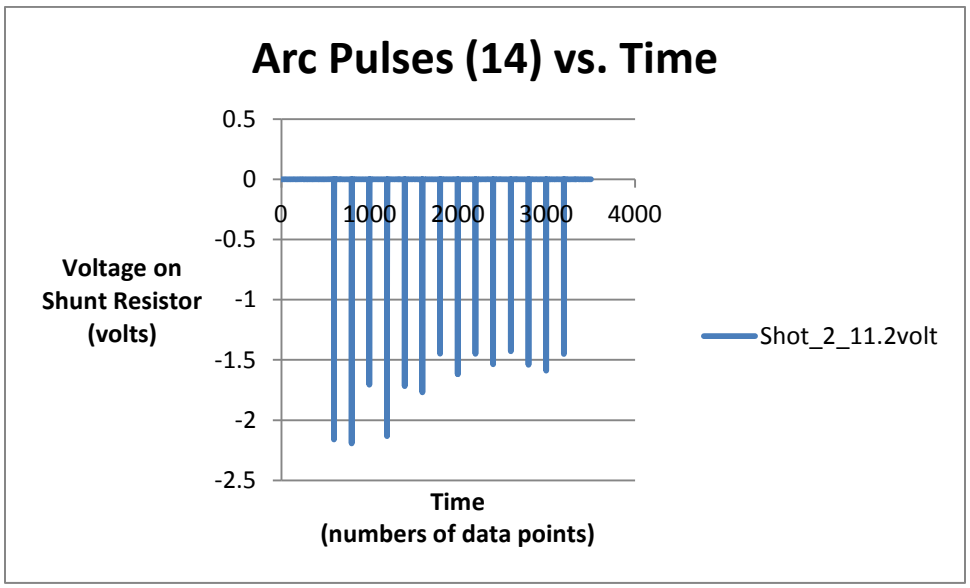

Figure C-7: Arc Pulses (14) vs. Time for Shot 2 at 11.2 Volts

Appendix C – Arc Pulses vs. Time for Various Magnetic Field Strengths

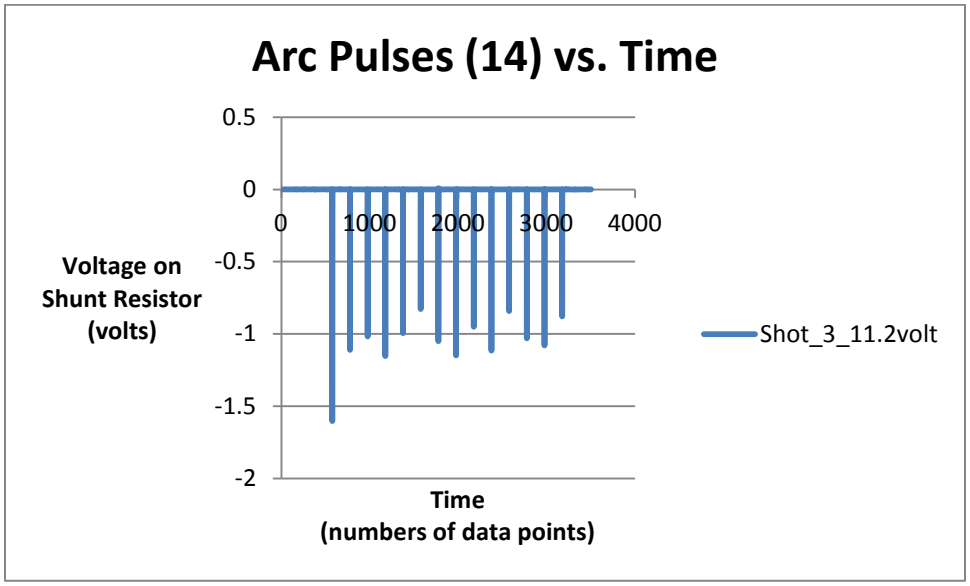

Figure C-8: Arc Pulses (14) vs. Time for Shot 3 at 11.2 Volts

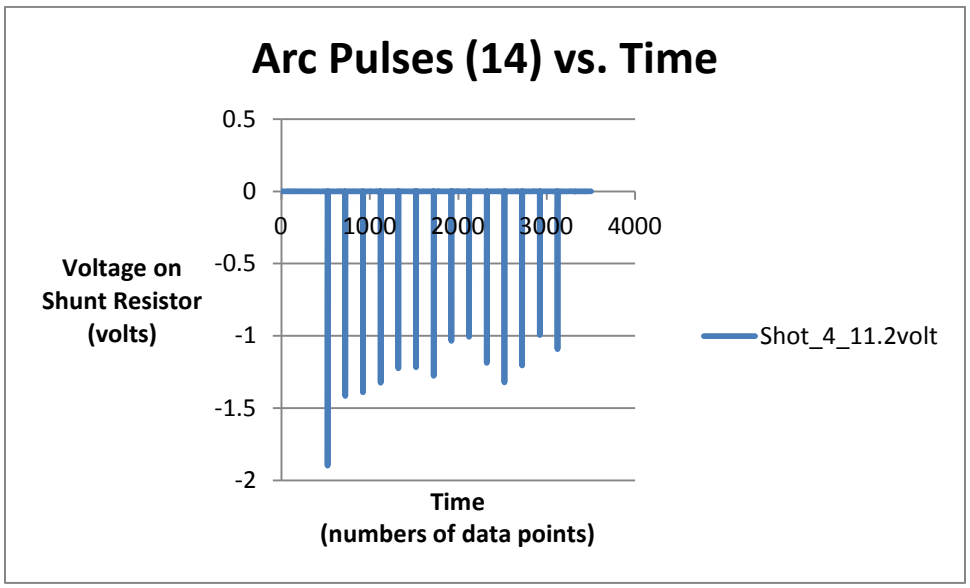

Figure C-9: Arc Pulses (14) vs. Time for Shot 4 at 11.2 Volts

Appendix C – Arc Pulses vs. Time for Various Magnetic Field Strengths

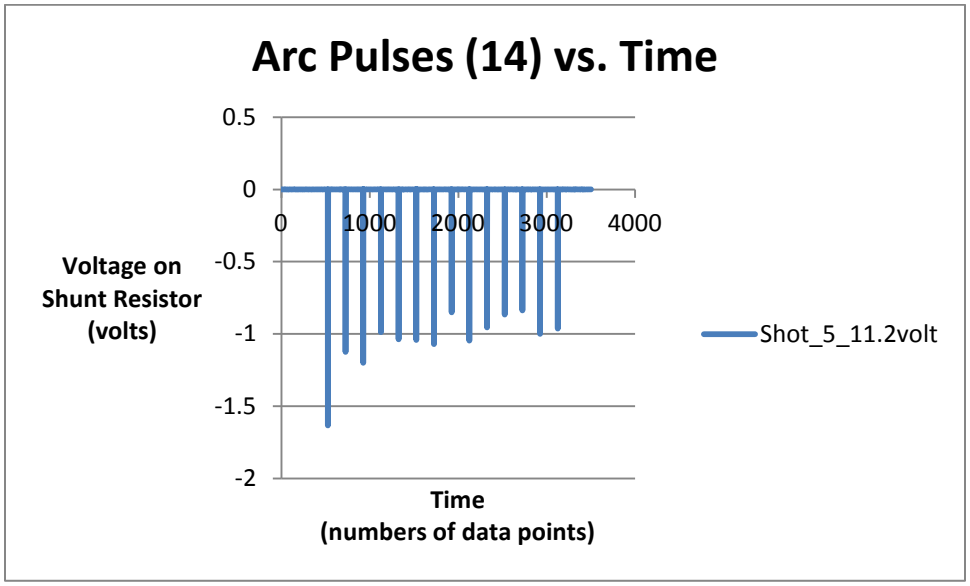

Figure C-10: Arc Pulses (14) vs. Time for Shot 5 at 11.2 Volts

Appendix C – Arc Pulses vs. Time for Various Magnetic Field Strengths

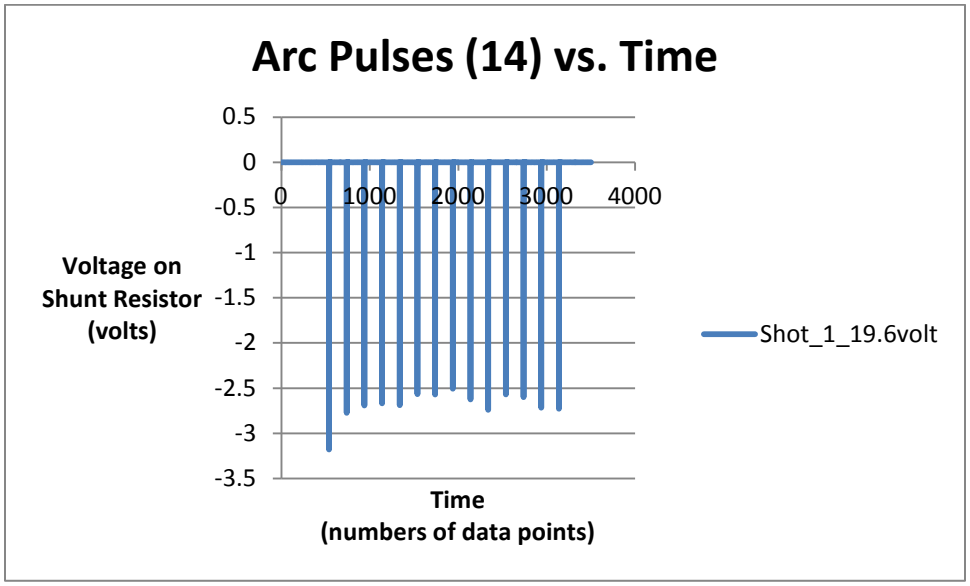

Figure C-11: Arc Pulses (14) vs. Time for Shot 1 at 19.6 Volts

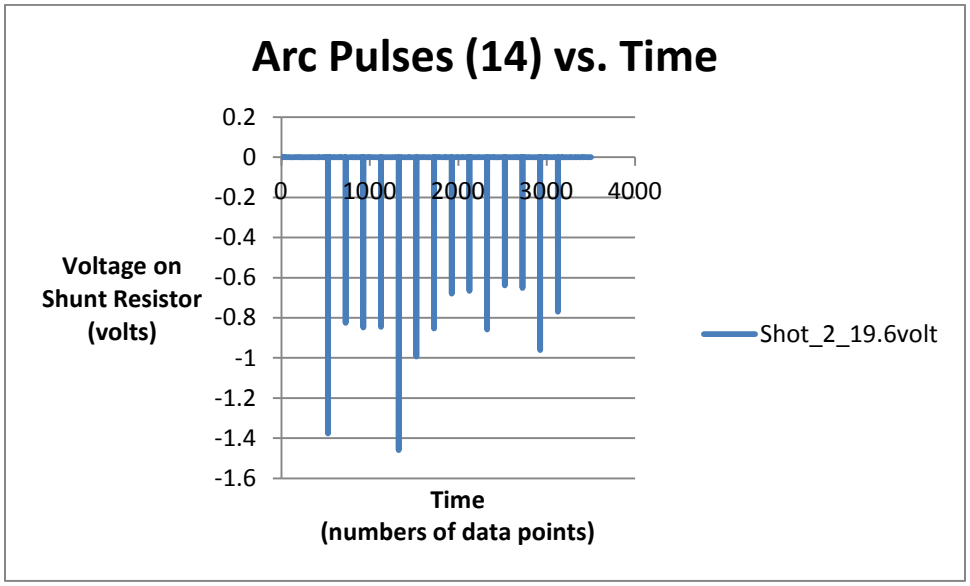

Figure C-12: Arc Pulses (14) vs. Time for Shot 2 at 19.6 Volts

Appendix C – Arc Pulses vs. Time for Various Magnetic Field Strengths

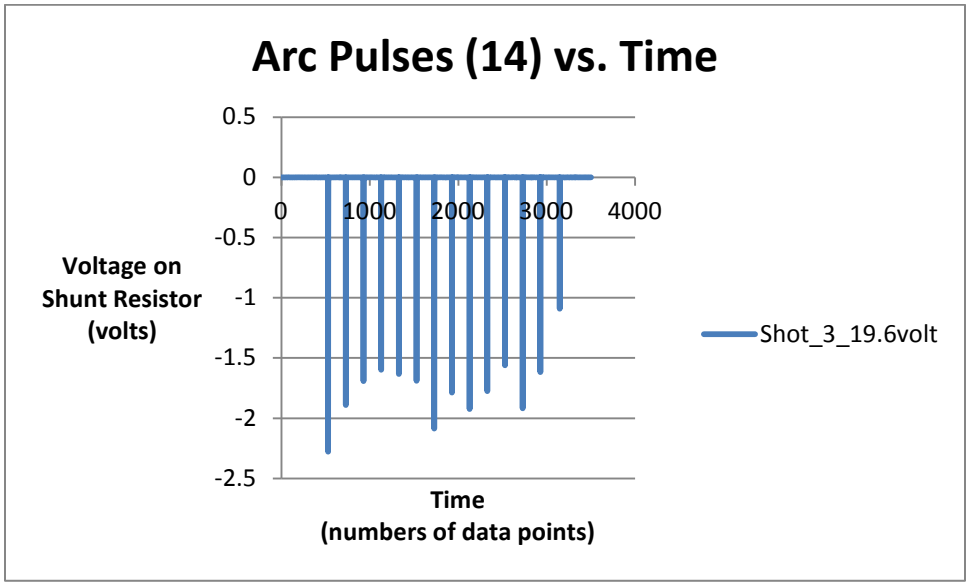

Figure C-13: Arc Pulses (14) vs. Time for Shot 3 at 19.6 Volts

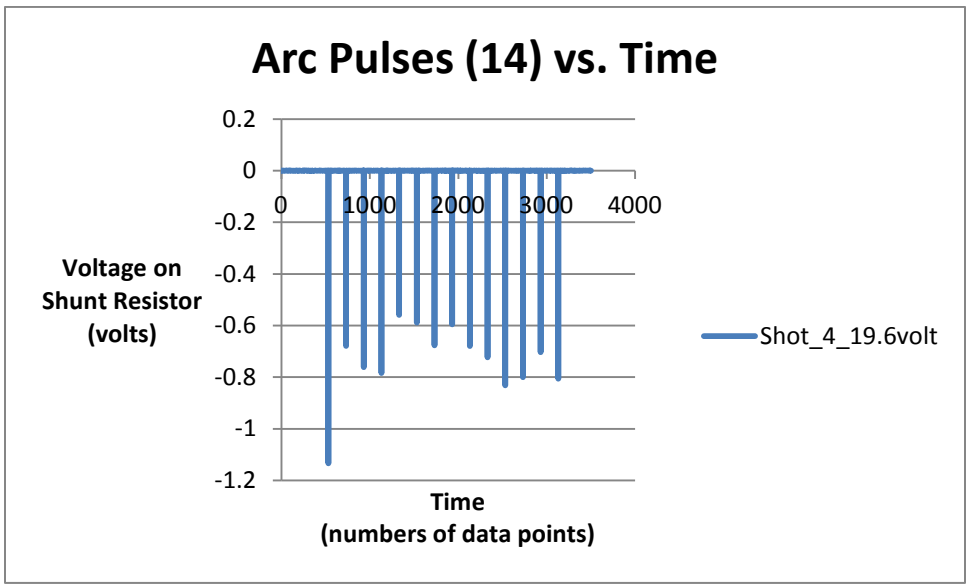

Figure C-14: Arc Pulses (14) vs. Time for Shot 4 at 19.6 Volts

Appendix C – Arc Pulses vs. Time for Various Magnetic Field Strengths

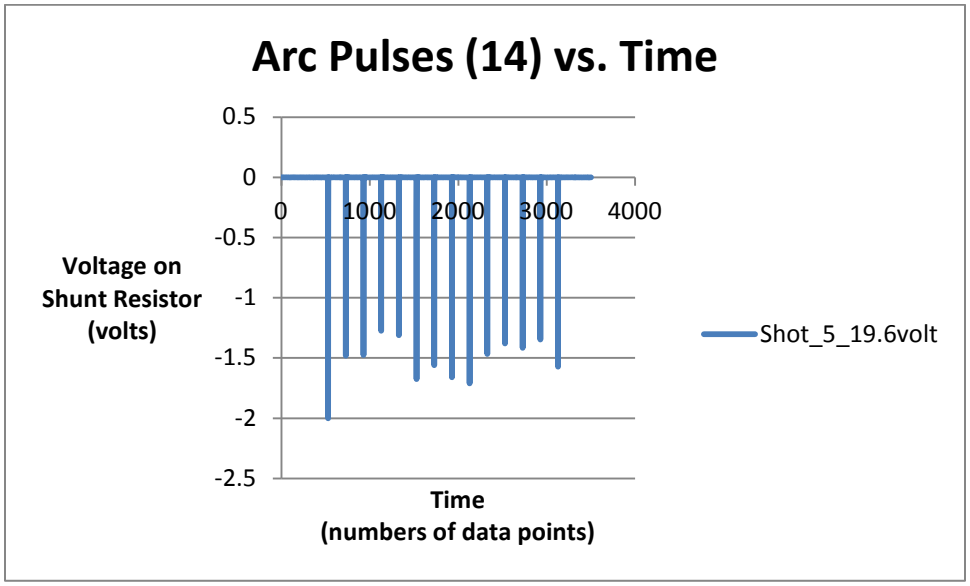

Figure C-15: Arc Pulses (14) vs. Time for Shot 5 at 19.6 Volts

Appendix C – Arc Pulses vs. Time for Various Magnetic Field Strengths

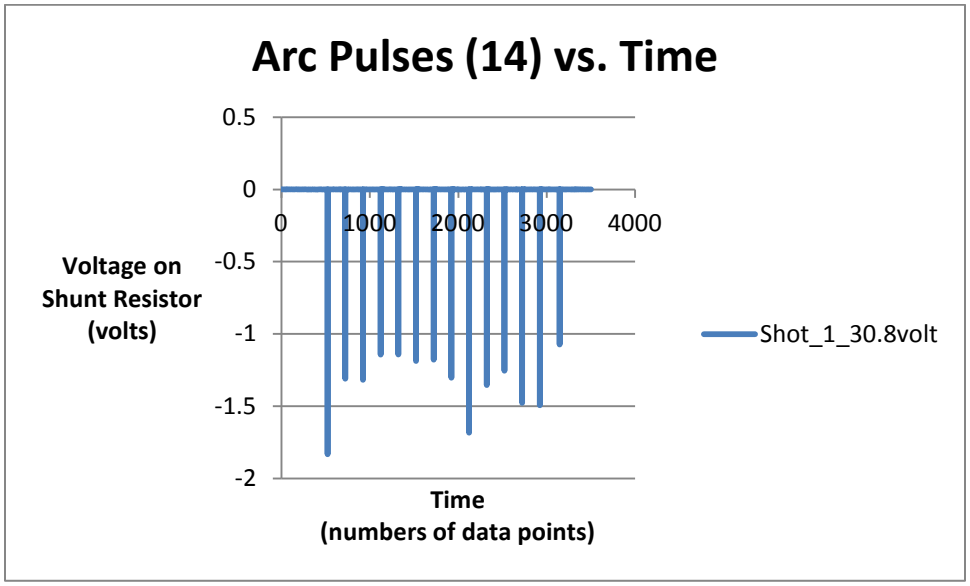

Figure C-16: Arc Pulses (14) vs. Time for Shot 1 at 30.8 Volts

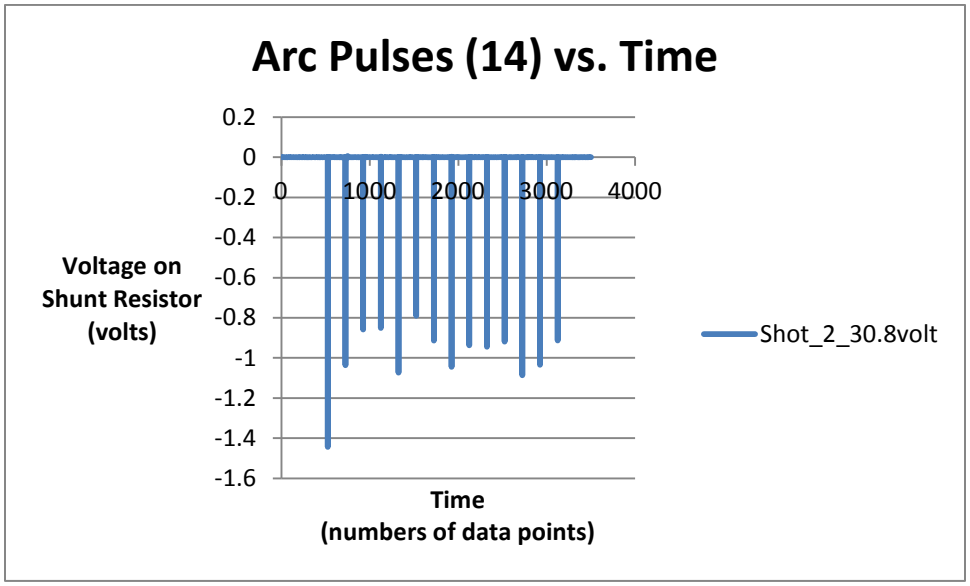

Figure C-17: Arc Pulses (14) vs. Time for Shot 2 at 30.8 Volts

Appendix C – Arc Pulses vs. Time for Various Magnetic Field Strengths

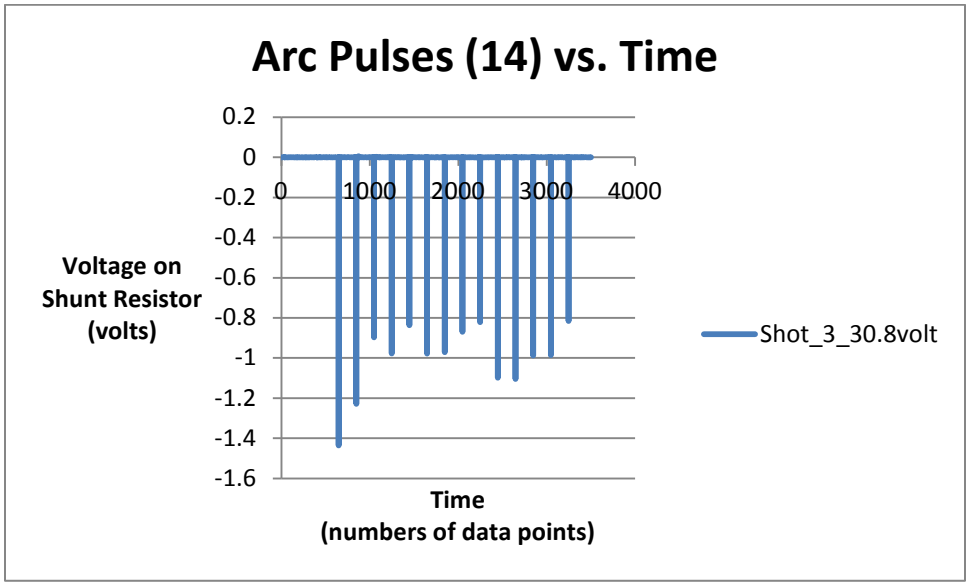

Figure C-18: Arc Pulses (14) vs. Time for Shot 3 at 30.8 Volts

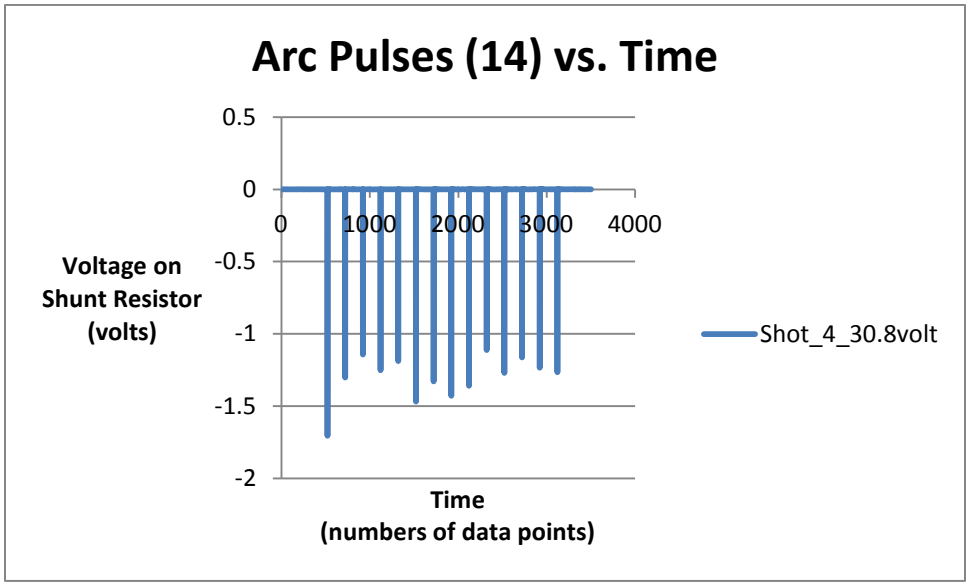

Figure C-19: Arc Pulses (14) vs. Time for Shot 4 at 30.8 Volts

Appendix C – Arc Pulses vs. Time for Various Magnetic Field Strengths

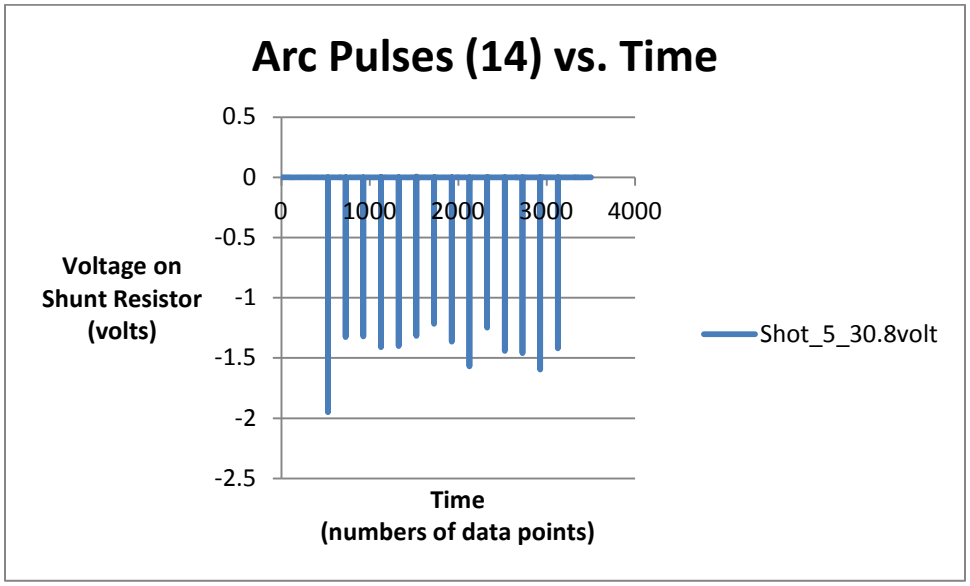

Figure C-20: Arc Pulses (14) vs. Time for Shot 5 at 30.8 Volts

Appendix C – Arc Pulses vs. Time for Various Magnetic Field Strengths

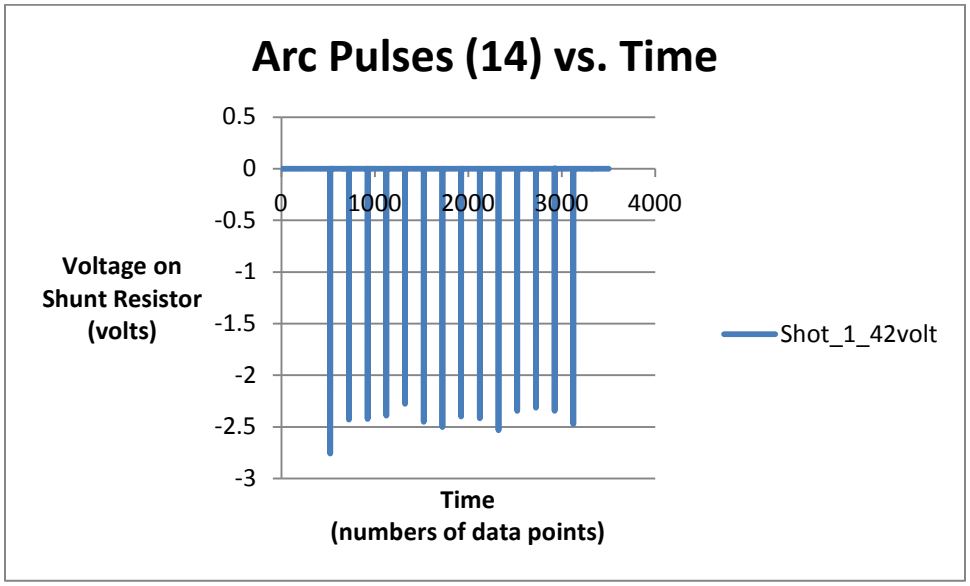

Figure C-21: Arc Pulses (14) vs. Time for Shot 1 at 42 Volts

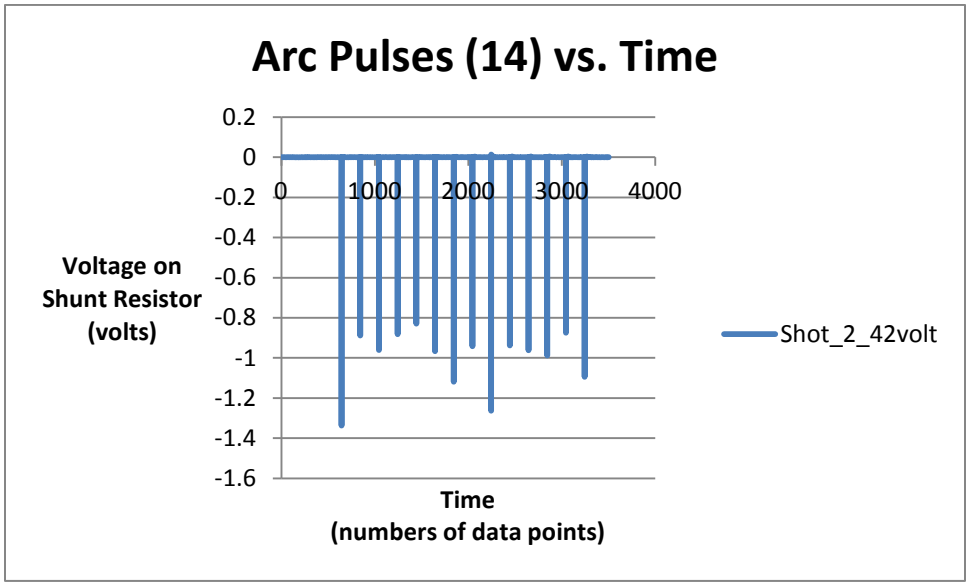

Figure C-22: Arc Pulses (14) vs. Time for Shot 2 at 42 Volts

Appendix C – Arc Pulses vs. Time for Various Magnetic Field Strengths

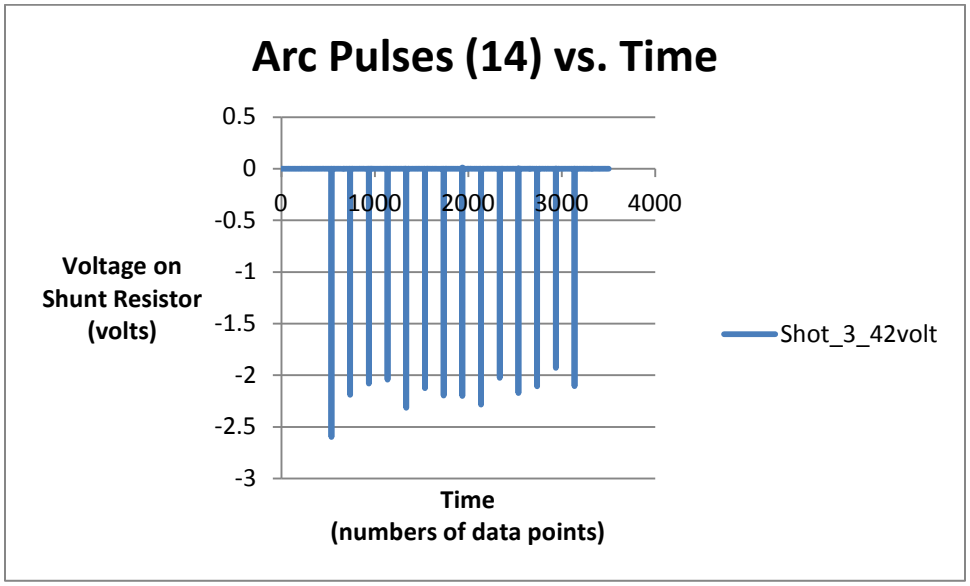

Figure C-23: Arc Pulses (14) vs. Time for Shot 3 at 42 Volts

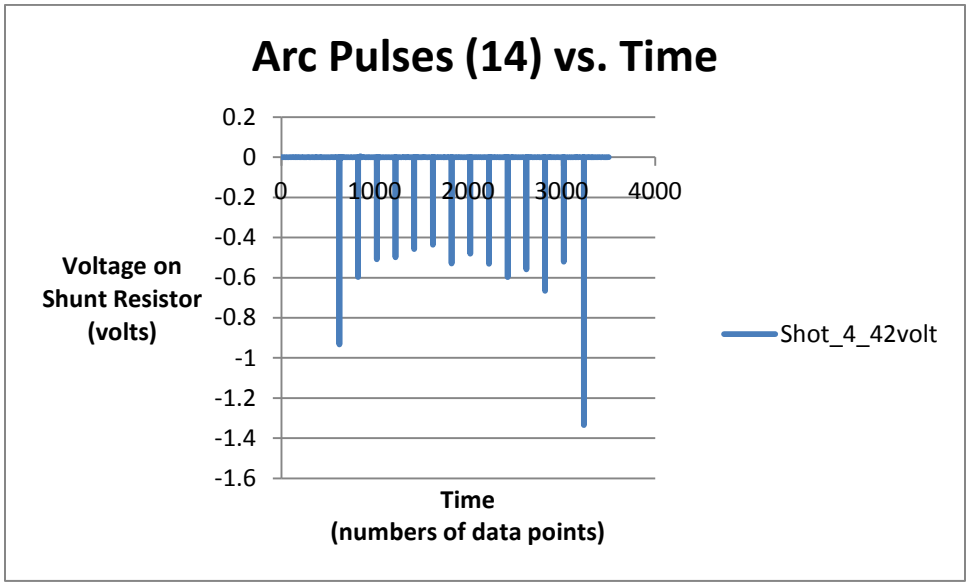

Figure C-24: Arc Pulses (14) vs. Time for Shot 4 at 42 Volts

Appendix C – Arc Pulses vs. Time for Various Magnetic Field Strengths

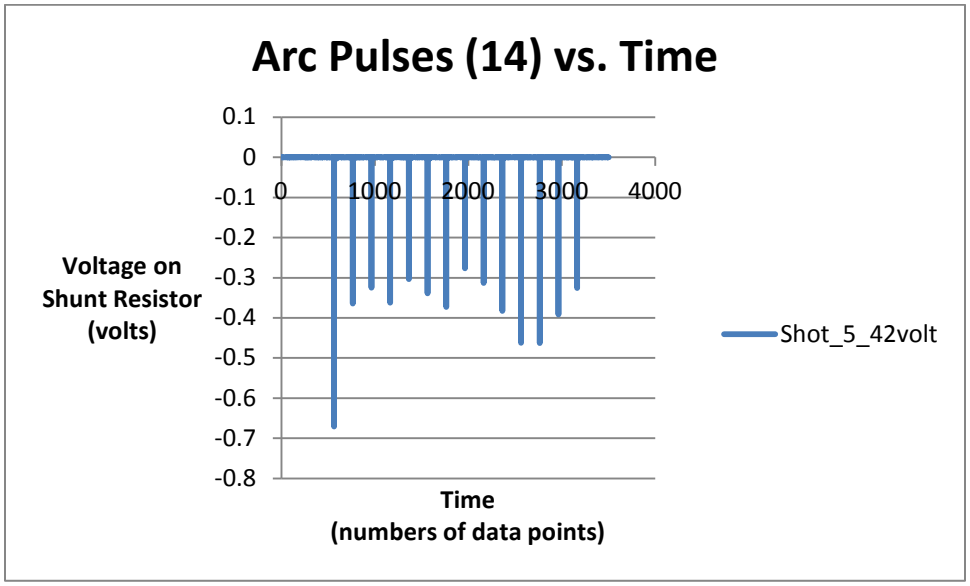

Figure C-25: Arc Pulses (14) vs. Time for Shot 5 at 42 Volts

Appendix C – Arc Pulses vs. Time for Various Magnetic Field Strengths

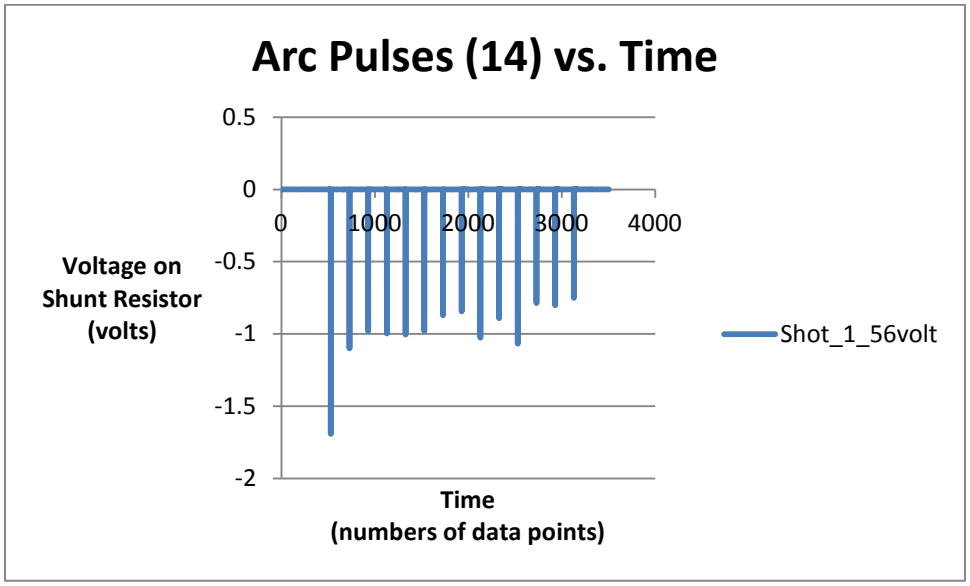

Figure C-26: Arc Pulses (14) vs. Time for Shot 1 at 56 Volts

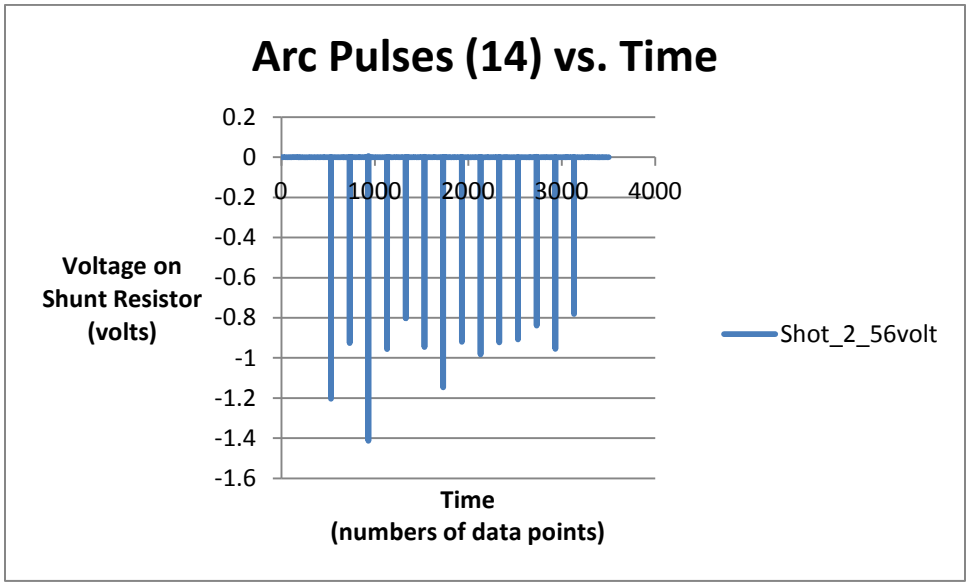

Figure C-27: Arc Pulses (14) vs. Time for Shot 2 at 56 Volts

Appendix C – Arc Pulses vs. Time for Various Magnetic Field Strengths

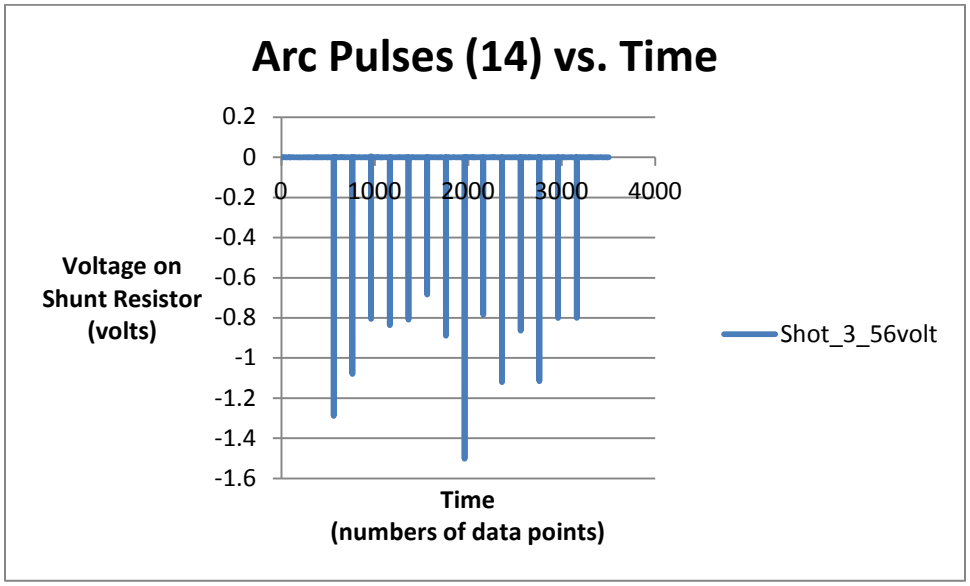

Figure C-28: Arc Pulses (14) vs. Time for Shot 3 at 56 Volts

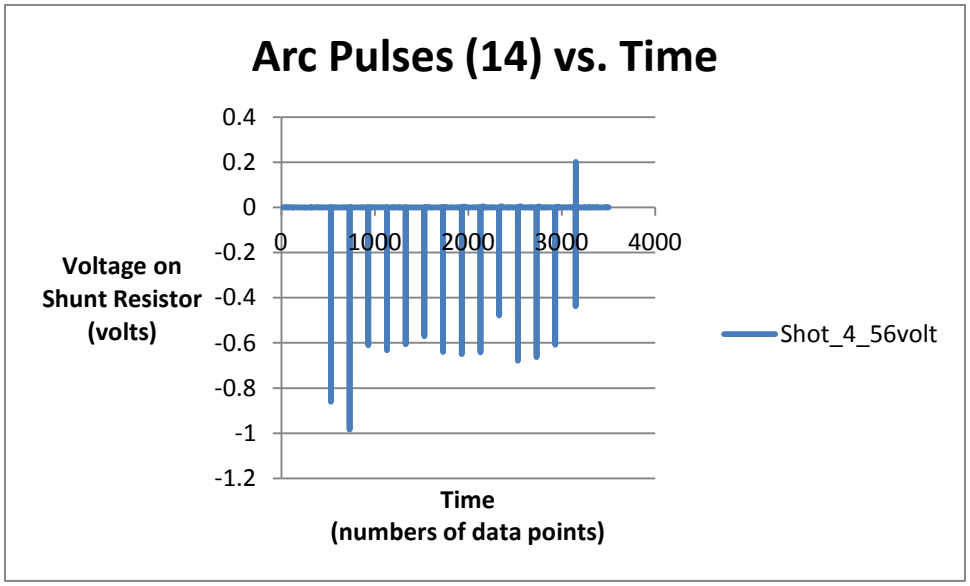

Figure C-29: Arc Pulses (14) vs. Time for Shot 4 at 56 Volts

Appendix C – Arc Pulses vs. Time for Various Magnetic Field Strengths

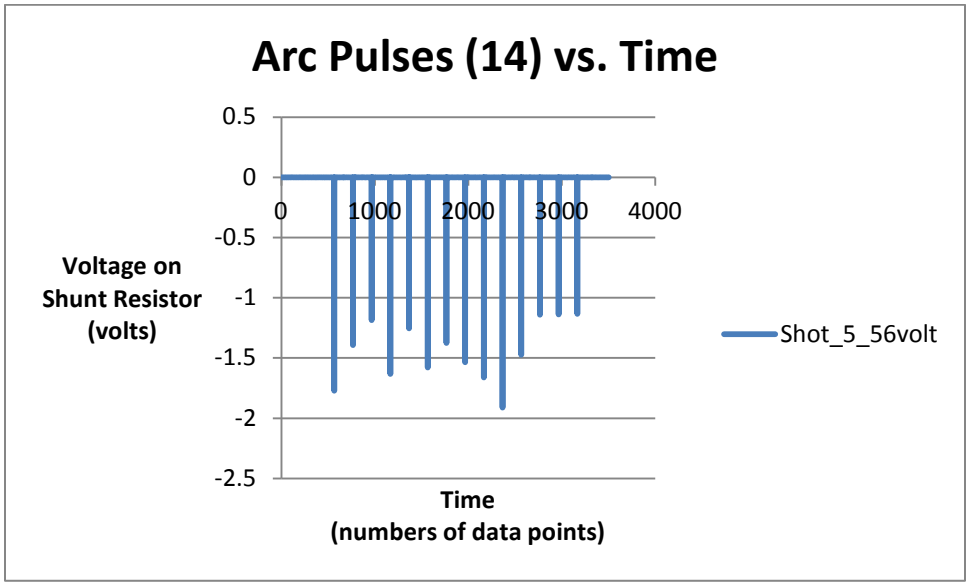

Figure C-30: Arc Pulses (14) vs. Time for Shot 5 at 56 Volts

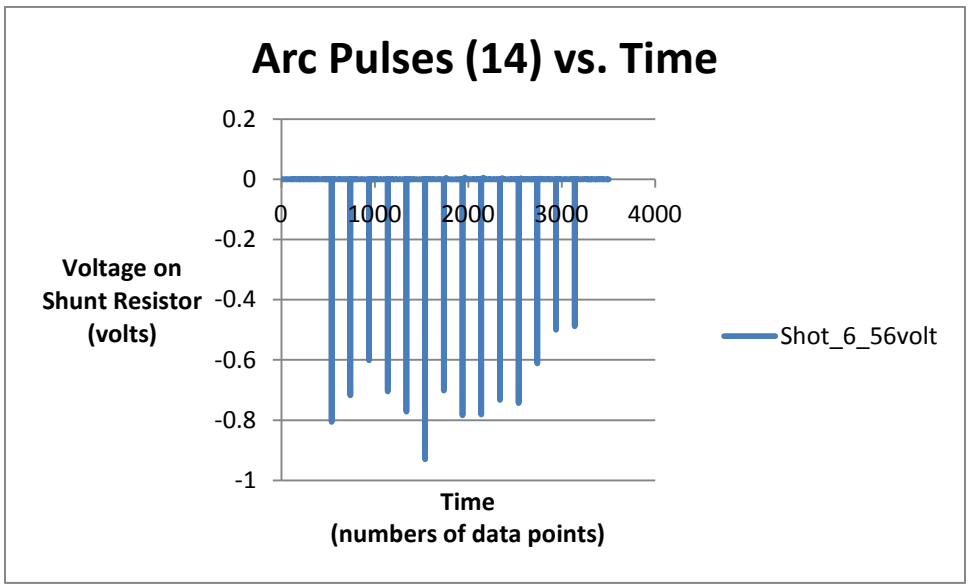

Figure C-31: Arc Pulses (14) vs. Time for Shot 6 at 56 Volts

Appendix C – Arc Pulses vs. Time for Various Magnetic Field Strengths

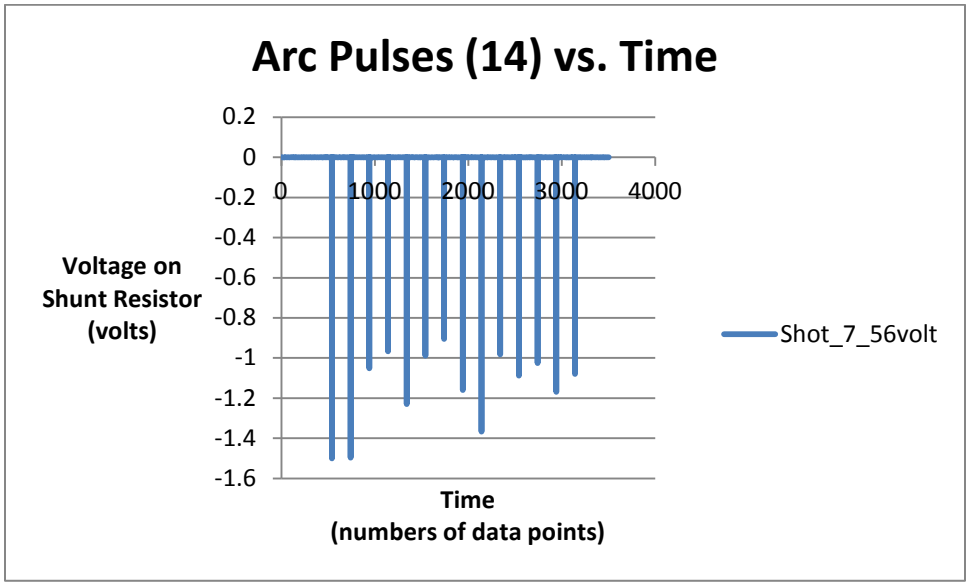

Figure C-32: Arc Pulses (14) vs. Time for Shot 7 at 56 Volts

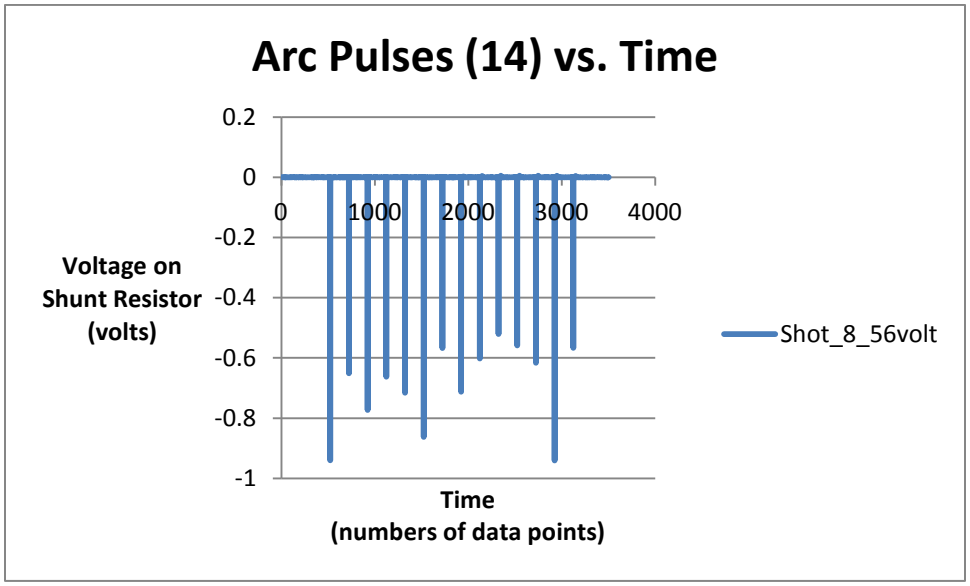

Figure C-33: Arc Pulses (14) vs. Time for Shot 8 at 56 Volts

Appendix C – Arc Pulses vs. Time for Various Magnetic Field Strengths

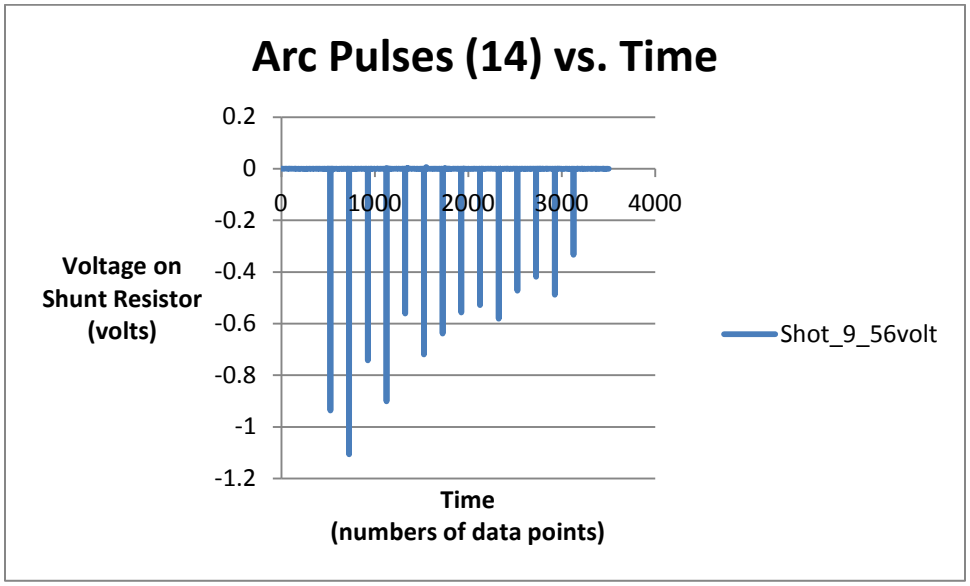

Figure C-34: Arc Pulses (14) vs. Time for Shot 9 at 56 Volts

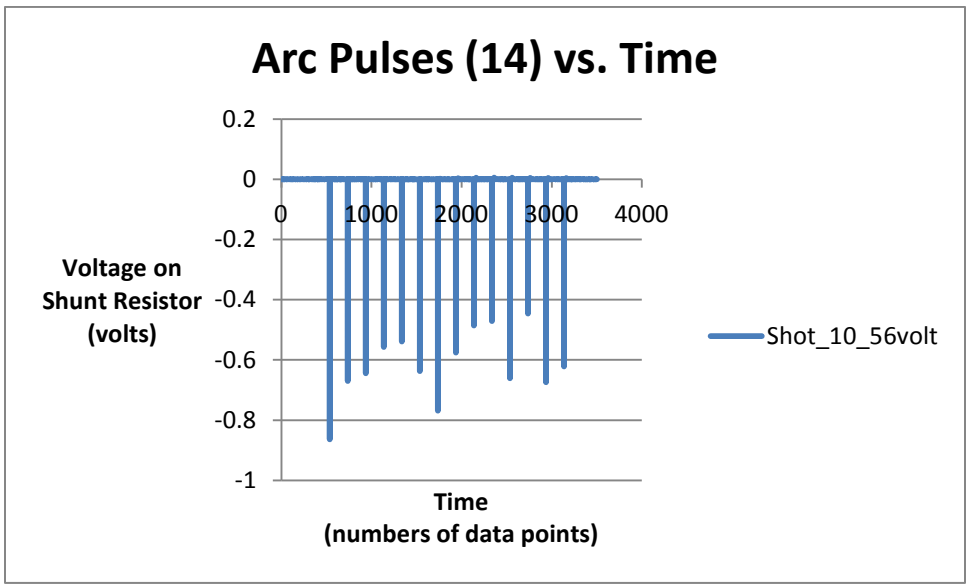

Figure C-35: Arc Pulses (14) vs. Time for Shot 10 at 56 Volts

Appendix C – Arc Pulses vs. Time for Various Magnetic Field Strengths

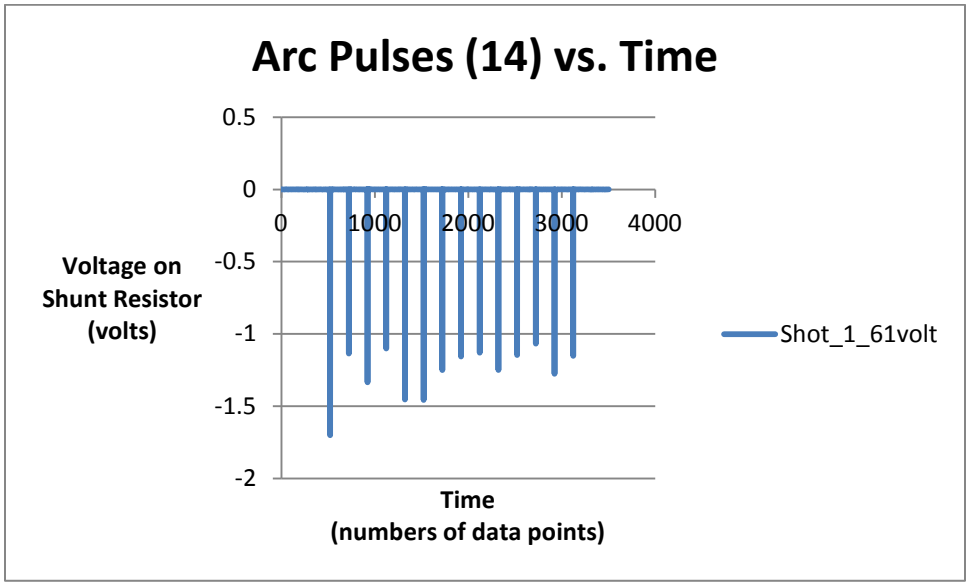

Figure C-36: Arc Pulses (14) vs. Time for Shot 1 at 61 Volts

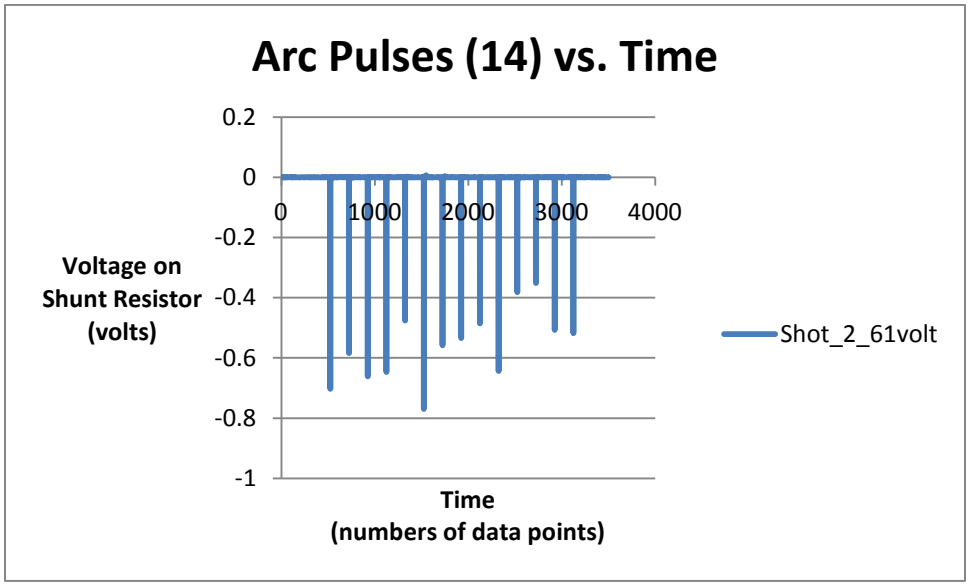

Figure C-37: Arc Pulses (14) vs. Time for Shot 2 at 61 Volts

Appendix C – Arc Pulses vs. Time for Various Magnetic Field Strengths

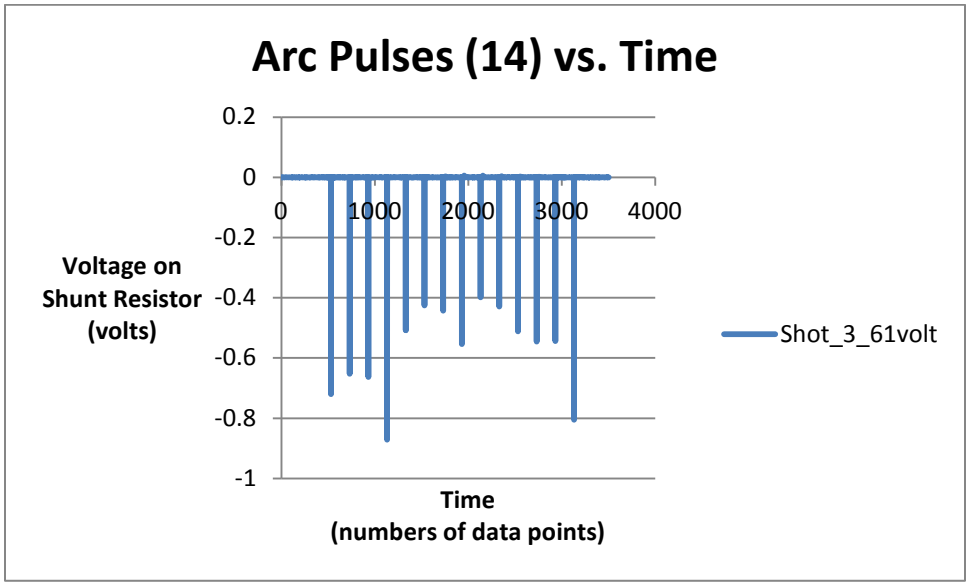

Figure C-38: Arc Pulses (14) vs. Time for Shot 3 at 61 Volts

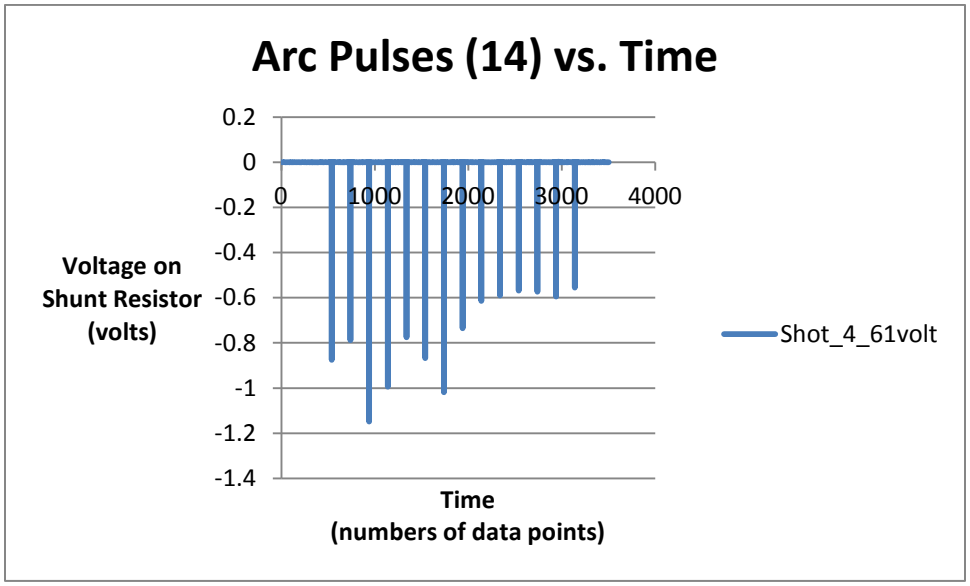

Figure C-39: Arc Pulses (14) vs. Time for Shot 4 at 61 Volts

Appendix C – Arc Pulses vs. Time for Various Magnetic Field Strengths

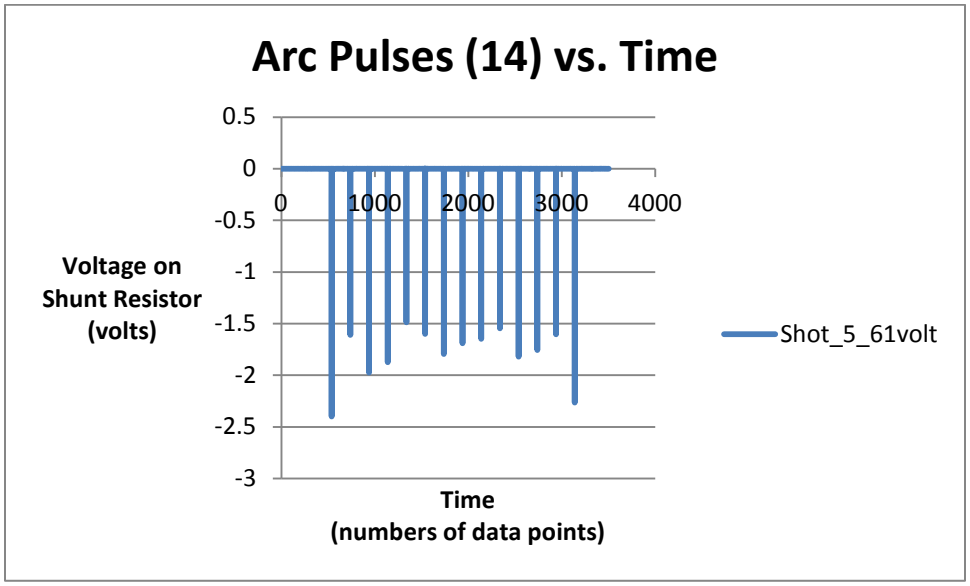

Figure C-40: Arc Pulses (14) vs. Time for Shot 5 at 61 Volts

Appendix C – Arc Pulses vs. Time for Various Magnetic Field Strengths

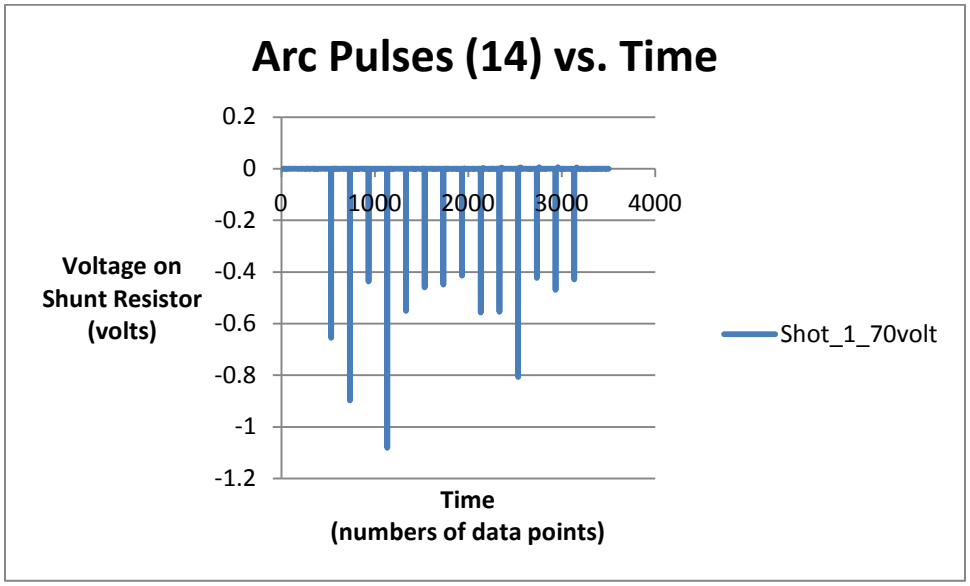

Figure C-41: Arc Pulses (14) vs. Time for Shot 1 at 70 Volts

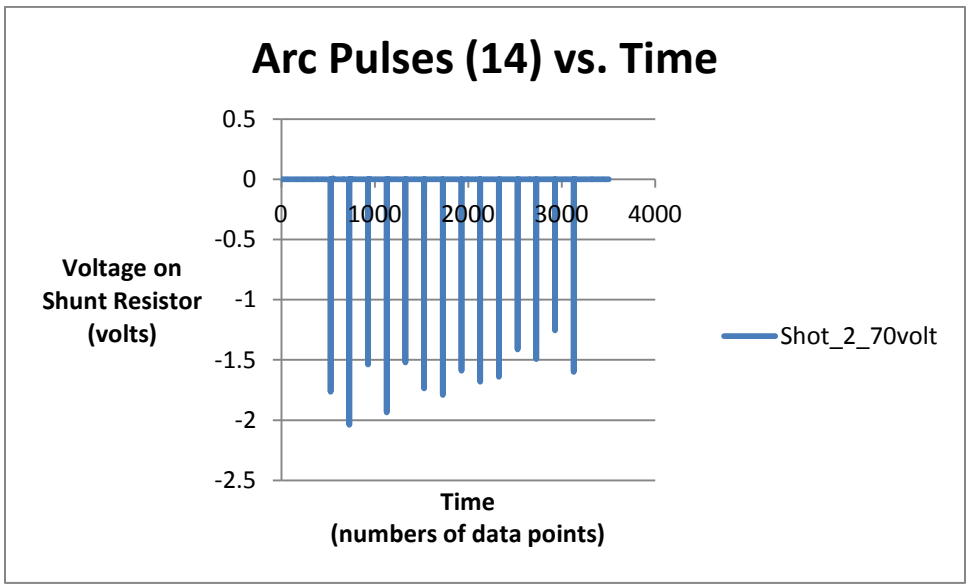

Figure C-42: Arc Pulses (14) vs. Time for Shot 2 at 70 Volts

Appendix C – Arc Pulses vs. Time for Various Magnetic Field Strengths

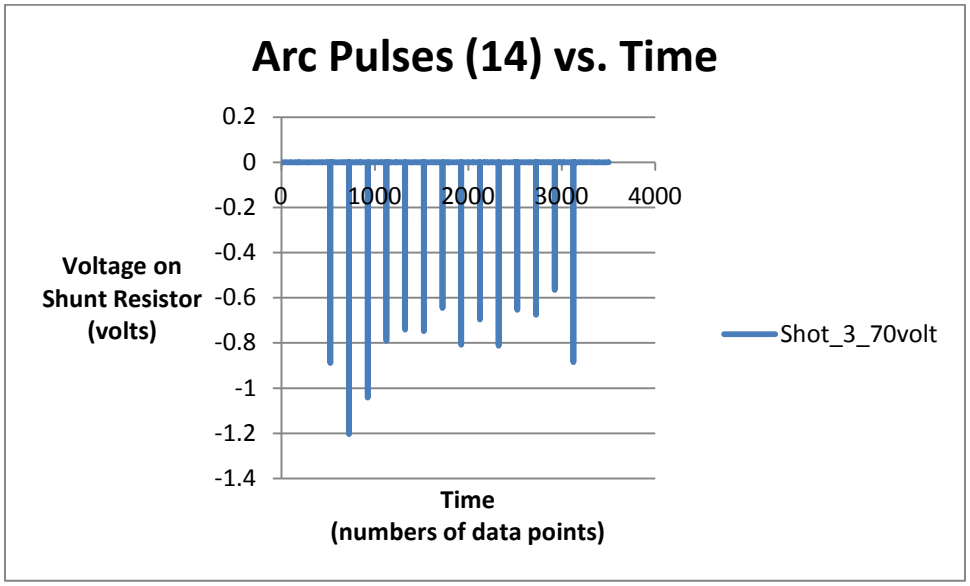

Figure C-43: Arc Pulses (14) vs. Time for Shot 3 at 70 Volts

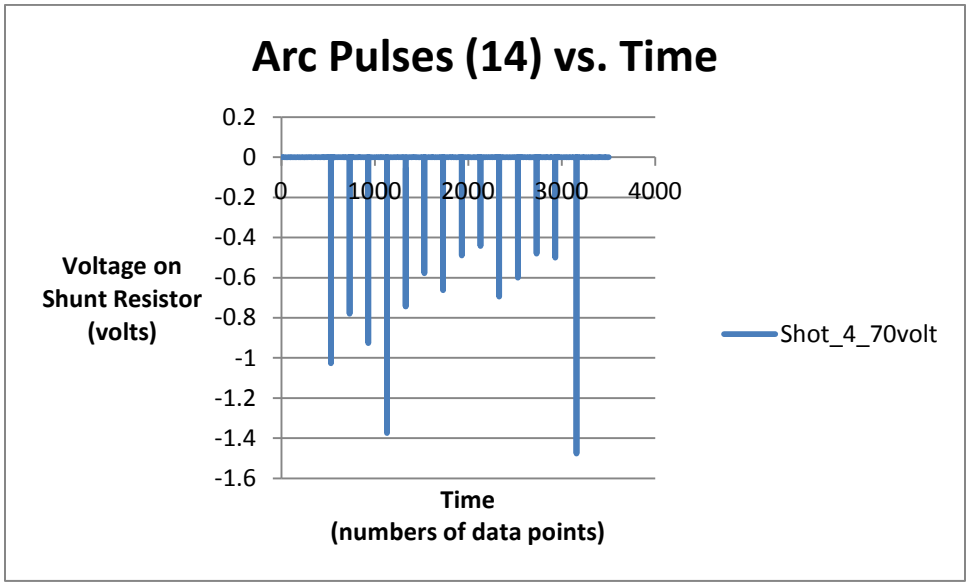

Figure C-44: Arc Pulses (14) vs. Time for Shot 4 at 70 Volts

Appendix C – Arc Pulses vs. Time for Various Magnetic Field Strengths

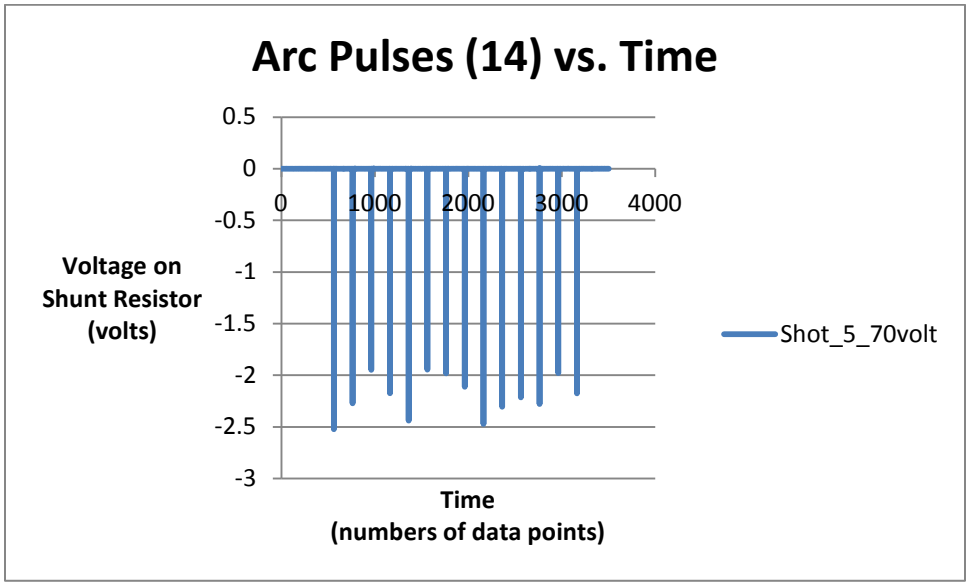

Figure C-45: Arc Pulses (14) vs. Time for Shot 5 at 70 Volts

Appendix D – Magnetic Field Simulations

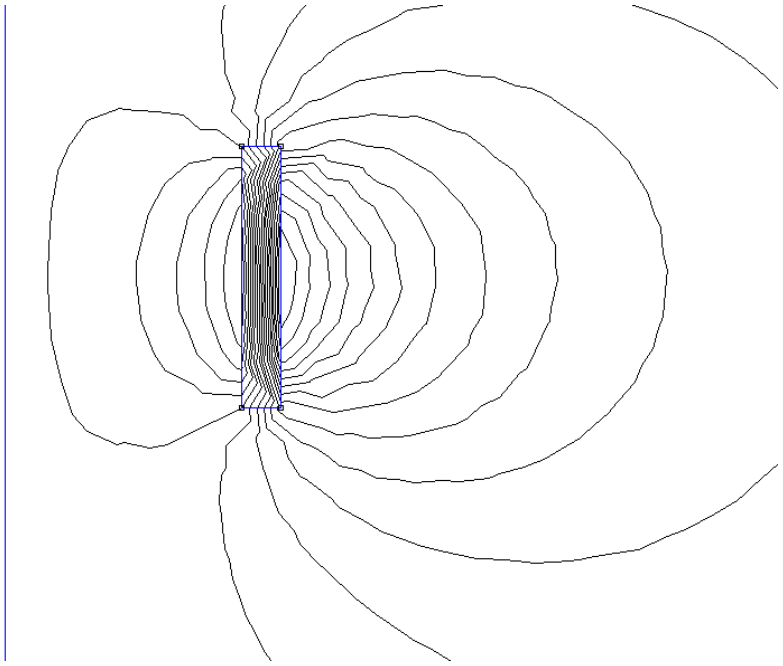

Figure D-1: Magnetic Field Simulation, AxialMagnet1.ans (Smaller Area)

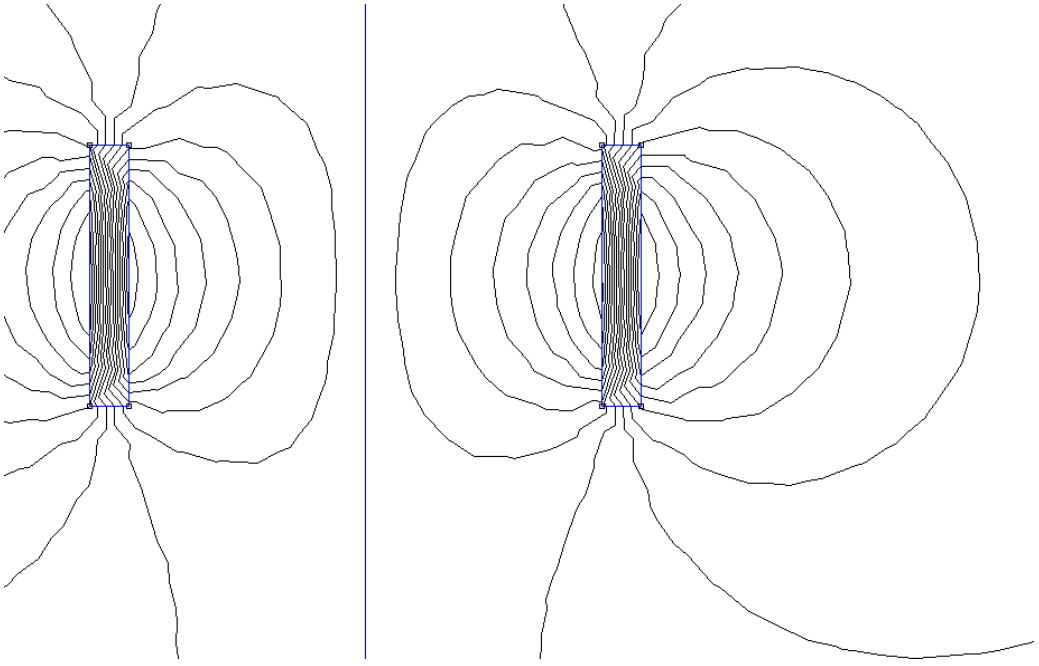

Figure D-2: Magnetic Field Simulation, PlanarMagnet1.ans (Smaller Area)

Appendix D – Magnetic Field Simulations

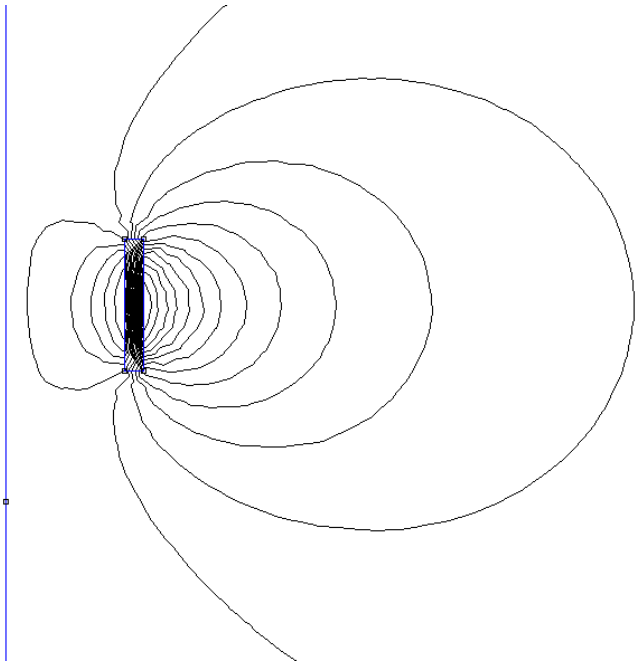

Figure D-3: Magnetic Field Simulation, AxialMagnet1.ans (Larger Area)

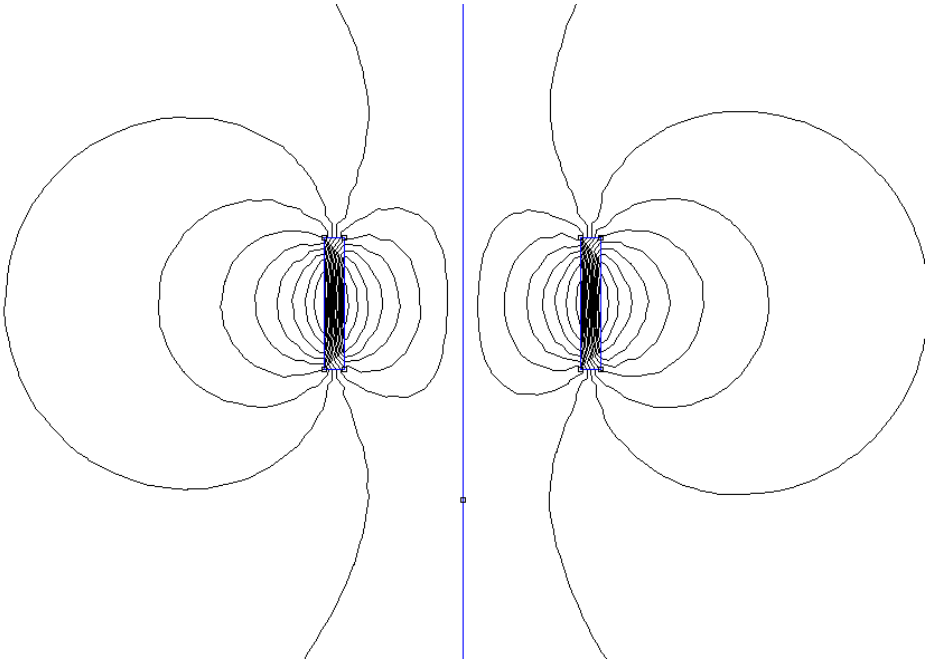

Figure D-4: Magnetic Field Simulation, PlanarMagnet1.ans (Larger Area)

Appendix D – Magnetic Field Simulations

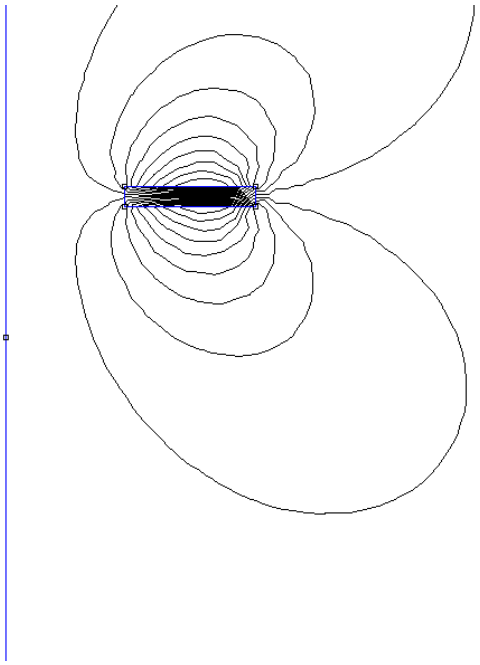

Figure D-5: Magnetic Field Simulation, AxialMagnet1Rotated.ans

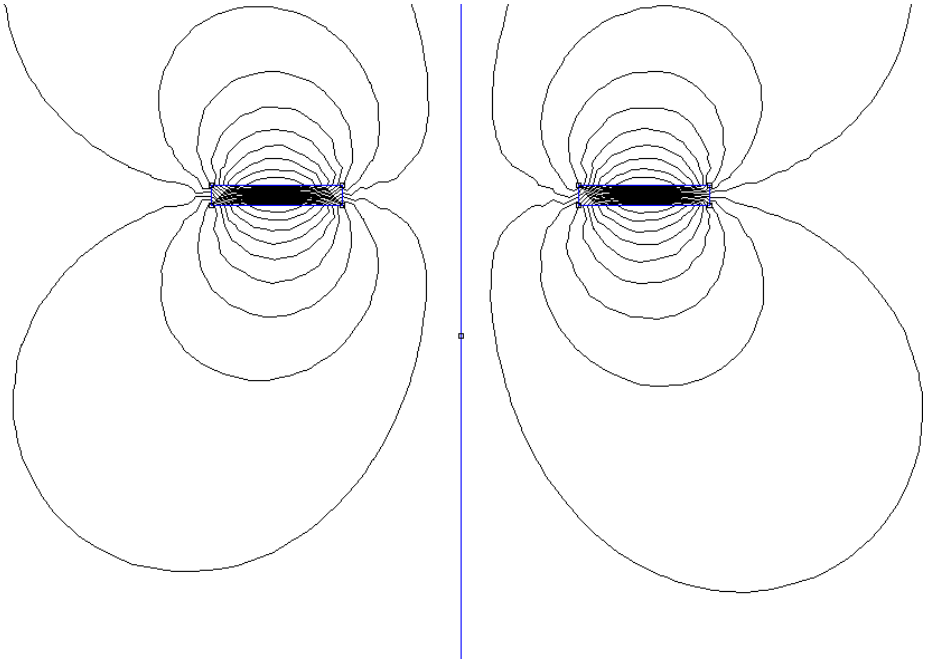

Figure D-6: Magnetic Field Simulation, PlanarMagnet1Rotated.ans

Appendix D – Magnetic Field Simulations

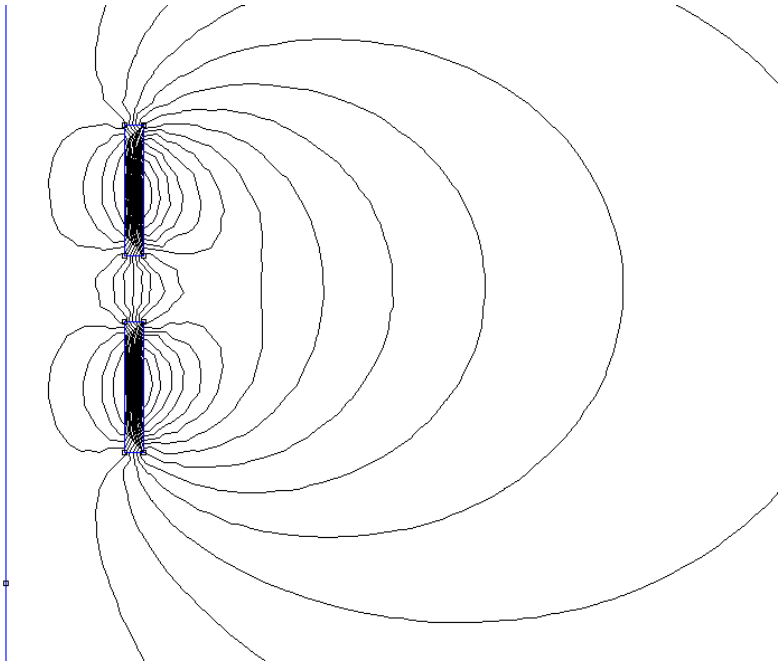

Figure D-7: Magnetic Field Simulation, AxialMagnet2NonExpanded.ans

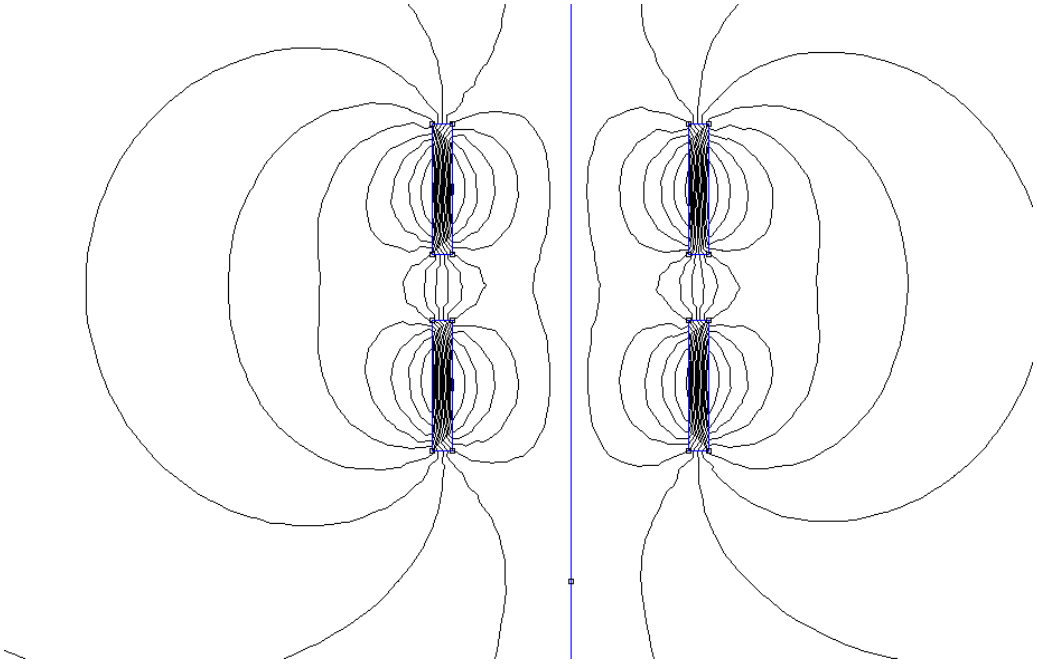

Figure D-8: Magnetic Field Simulation, PlanarMagnet2NonExpanded.ans

Appendix D – Magnetic Field Simulations

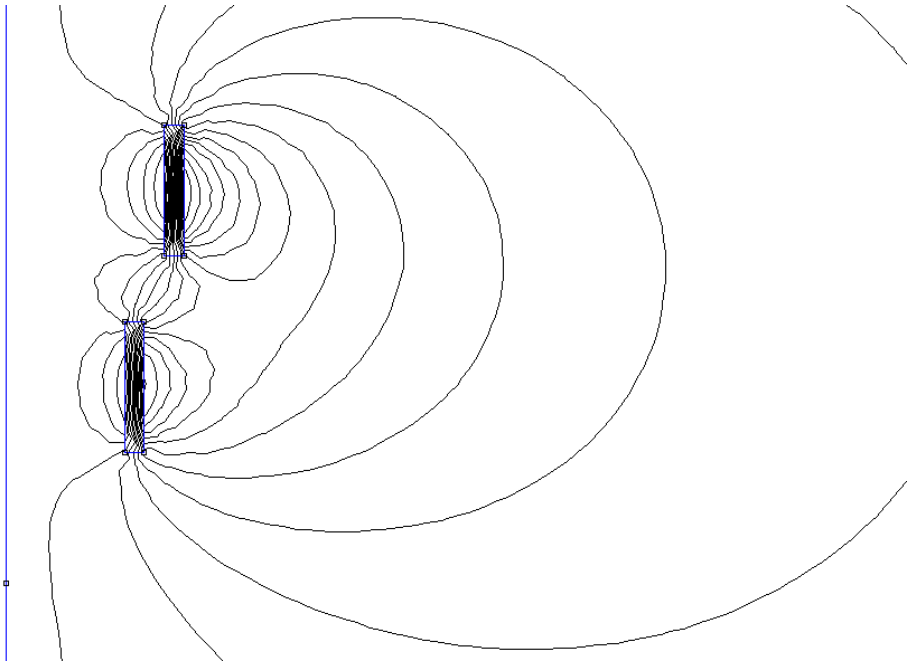

Figure D-9: Magnetic Field Simulation, AxialMagnet2Expanded.ans

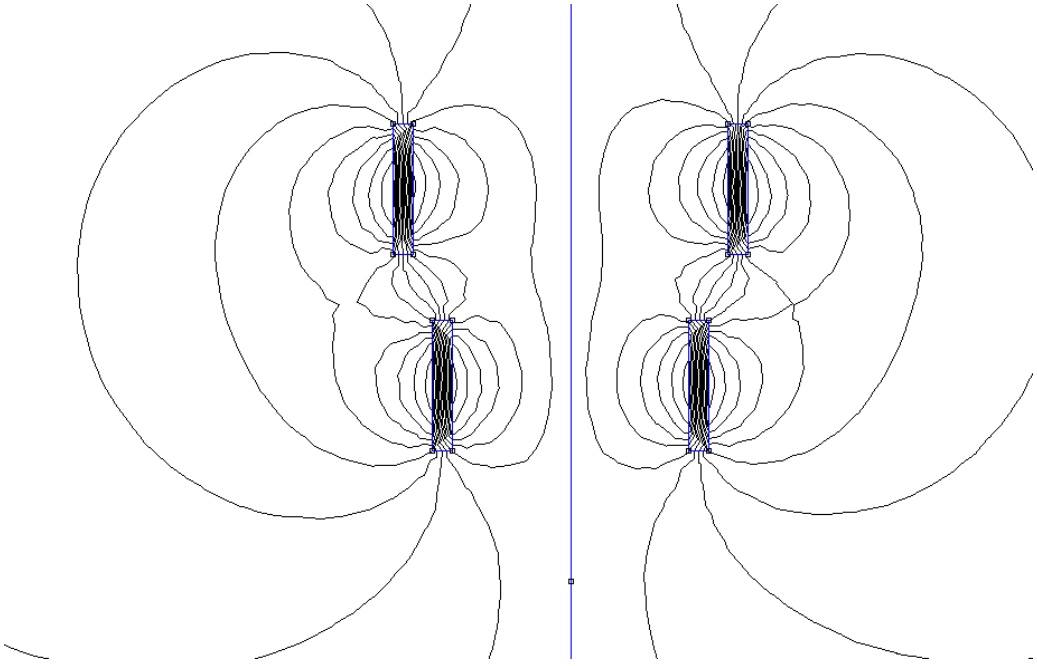

Figure D-10: Magnetic Field Simulation, PlanarMagnet2Expanded.ans

Appendix D – Magnetic Field Simulations

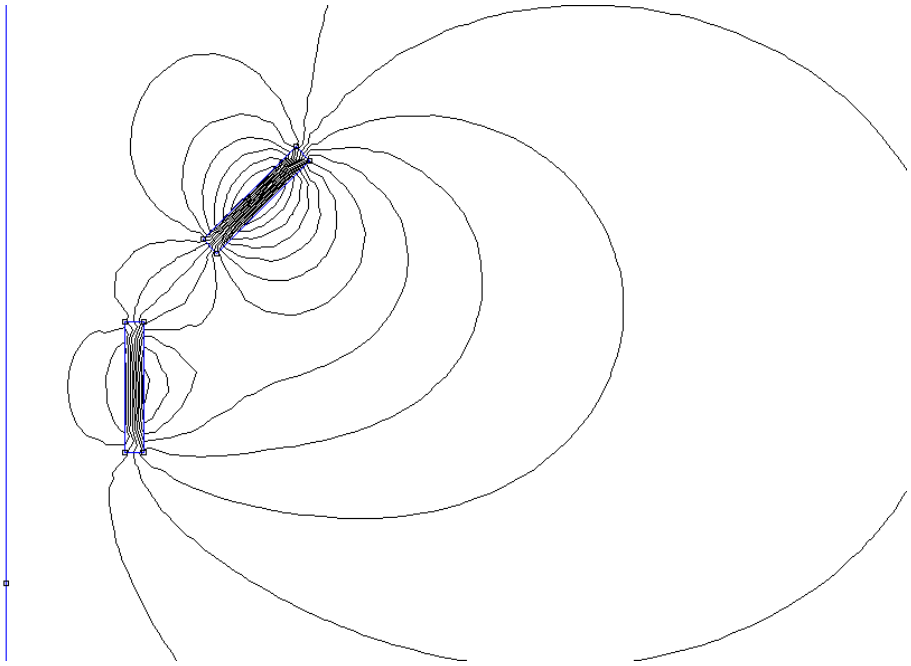

Figure D-11: Magnetic Field Simulation, AxialMagnet2_45Angle.ans

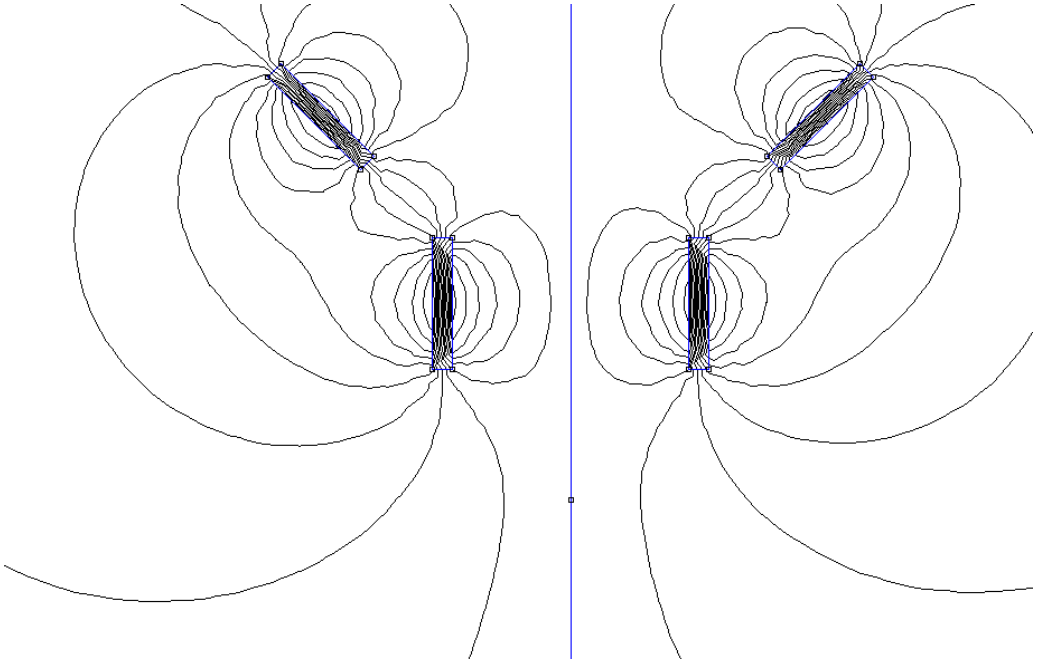

Figure D-12: Magnetic Field Simulation, PlanarMagnet2_45Angle.ans

Appendix D – Magnetic Field Simulations

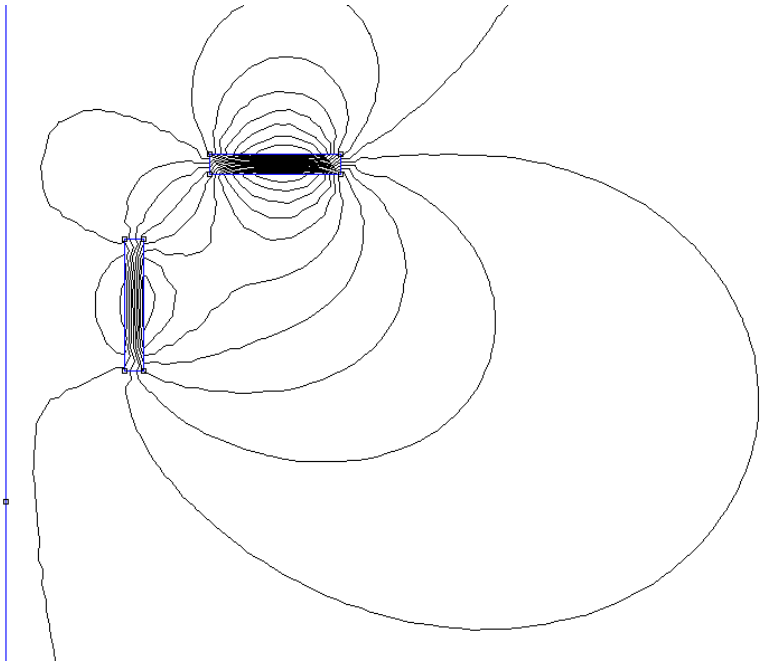

Figure D-13: Magnetic Field Simulation, AxialMagnet2RightAngle.ans

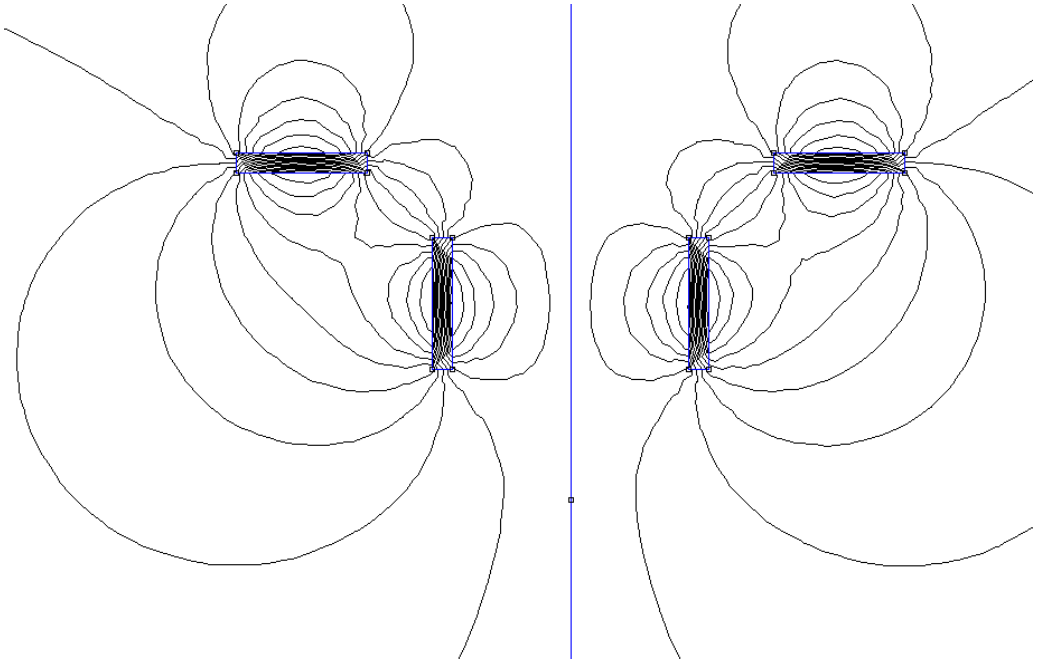

Figure D-14: Magnetic Field Simulation, PlanarMagnet2RightAngle.ans

Appendix D – Magnetic Field Simulations

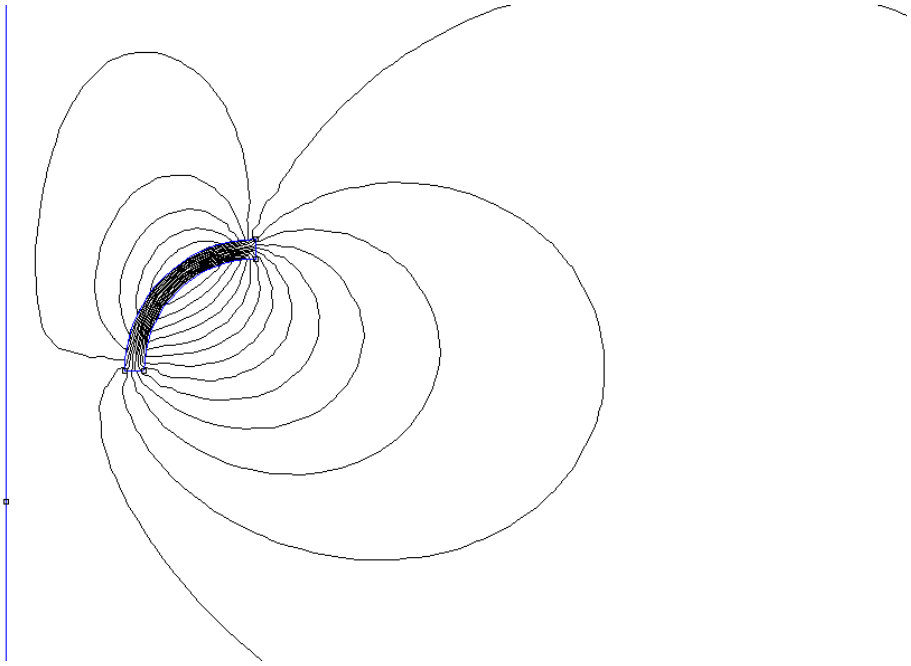

Figure D-15: Magnetic Field Simulation, AxialMagnet1QuarterCircle.ans

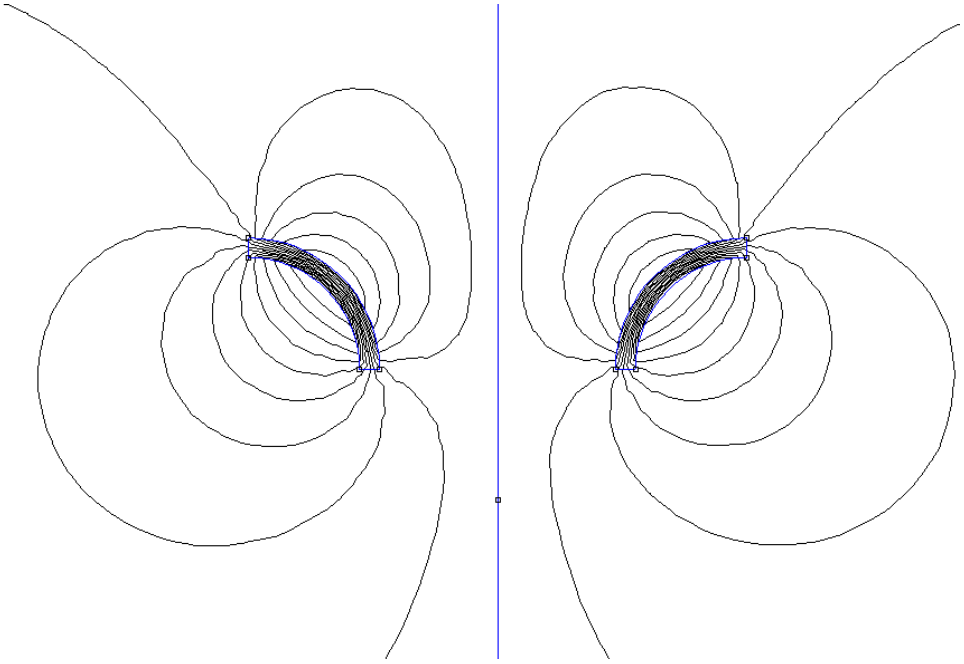

Figure D-16: Magnetic Field Simulation, PlanarMagnet1QuarterCircle.ans

Appendix D – Magnetic Field Simulations

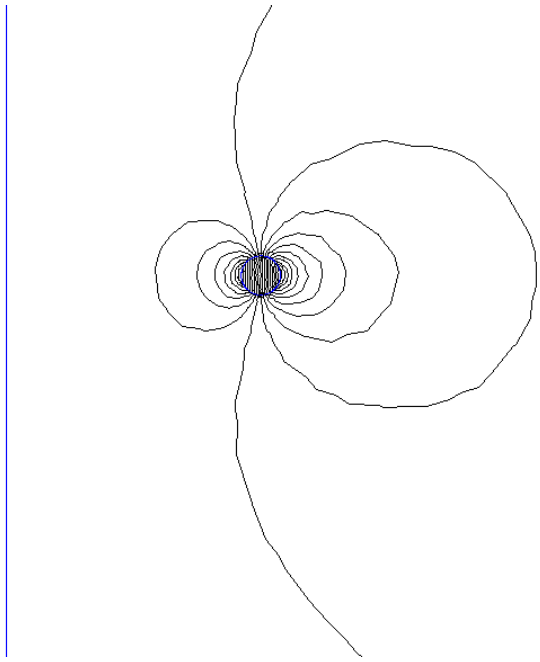

Figure D-17: Magnetic Field Simulation, AxialMagnet1Circular.ans

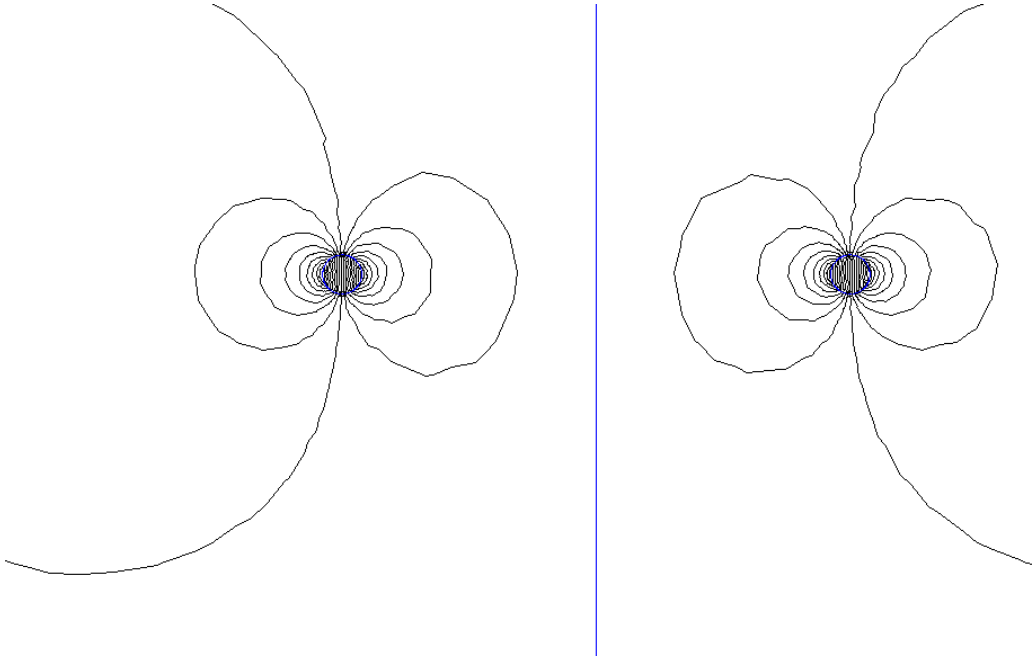

Figure D-18: Magnetic Field Simulation, PlanarMagnet1Circular.ans

Appendix D – Magnetic Field Simulations

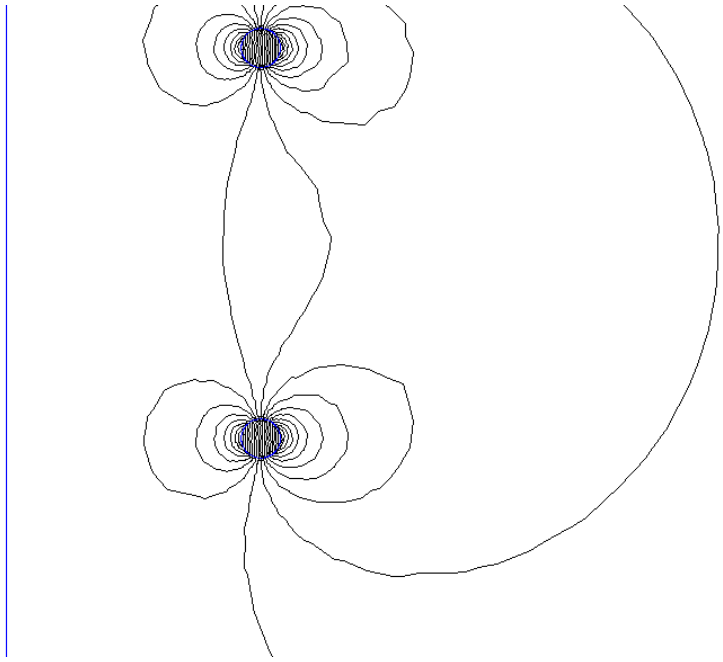

Figure D-19: Magnetic Field Simulation, AxialMagnet2Circular.ans

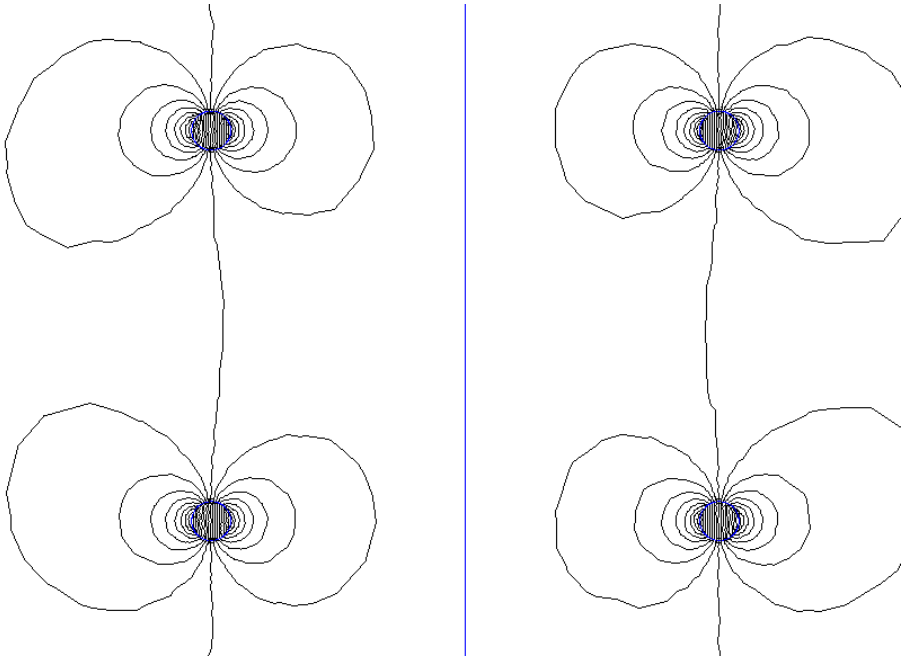

Figure D-20: Magnetic Field Simulation, PlanarMagnet2Circular.ans

Appendix D – Magnetic Field Simulations

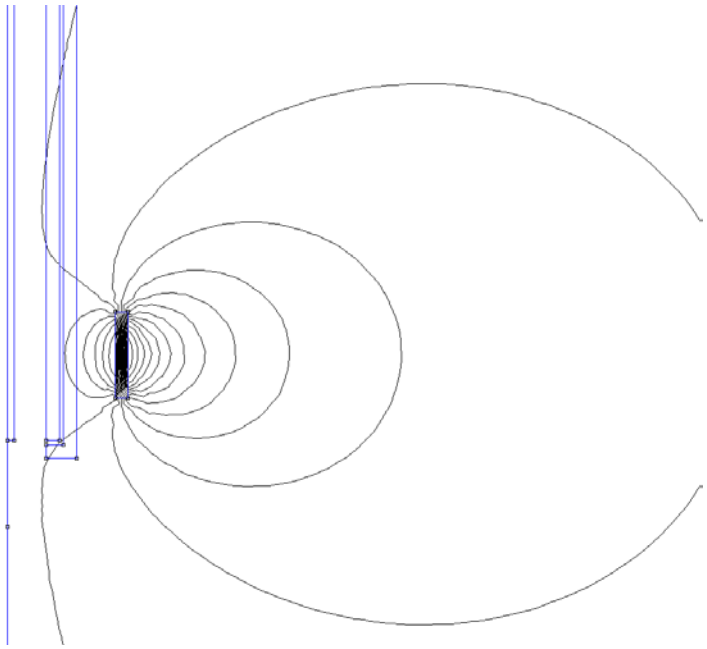

Figure D-21: Magnetic Field Simulation, μ CAT2_NonMagCasing.ans

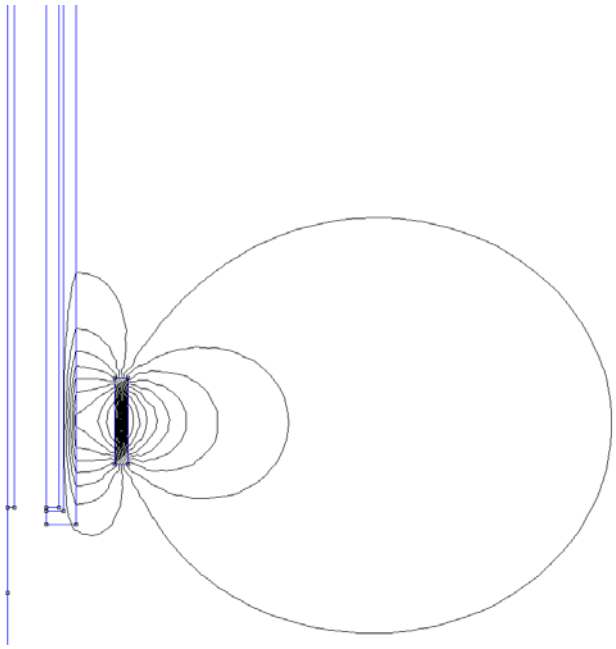

Figure D-22: Magnetic Field Simulation, μ CAT2_MagCasing.ans